Available online at www.sciencedirect.com
SCIENCE DIRECT®
Progress in Surface Science 77 (2004) 171–258
Progress in SURFACE SCIENCE
www.elsevier.com/locate/progsurf

Review

Mineral–water interfacial structures revealed by synchrotron X-ray scattering ☆

Paul Fenter [a,*], Neil C. Sturchio [b]

[a] *Argonne National Laboratory, ER-203, 9700 South Cass Avenue, Argonne, IL 60439, USA*
[b] *Department of Earth and Environmental Sciences, University of Illinois at Chicago, 845 West Taylor Street, Chicago, IL 60607, USA*

Abstract

Chemical reactions occurring at the mineral–water interface are controlled by an interfacial layer, nanometers thick, whose properties may deviate from those of the respective bulk mineral and water phases. The molecular-scale structure of this interfacial layer, however, is poorly constrained, and correlations between macroscopic phenomena and molecular-scale processes remain speculative. The application of high-resolution X-ray scattering techniques has begun to provide substantial new insights into the molecular-scale structure of the mineral–water interface. In this review, we describe the characteristics of synchrotron-based X-ray scattering techniques that make them uniquely powerful probes of mineral–water interfacial structures and discuss the new insights that have been derived from their application. In particular, we focus on efforts to understand the structure and distribution of interfacial water as well as their dependence on substrate properties for major mineral classes including oxides, carbonates, sulfates, phosphates, silicates, halides and chromates. We compare these X-ray scattering results with those from other structural and spectroscopic techniques and integrate

☆ The submitted manuscript has been created by the University of Chicago as operator of Argonne National Laboratory under Contract No. W-31-109-ENG-38 with the US Department of Energy. The US government retains for itself, and others acting on its behalf, a paid-up, non-exclusive, irrevocable worldwide license in said article to reproduce, prepare derivative works, distribute copies to the public, and perform publicly and display publicly, by or on behalf of the government.

* Corresponding author. Tel.: +1 630 252 7053.
E-mail address: fenter@anl.gov (P. Fenter).

0079-6816/$ - see front matter © 2005 Elsevier Ltd. All rights reserved.
doi:10.1016/j.progsurf.2004.12.001

these to provide a conceptual framework upon which to base an understanding of the systematic variation of mineral–water interfacial structures.
© 2005 Elsevier Ltd. All rights reserved.

Keywords: X-ray scattering; X-ray reflectivity; Crystal truncation rod; Water; Mineral–water interface; Solid–liquid interface; Interfacial water; Surface relaxation; Surface structure

Contents

1. Introduction

1.1. Background

The mineral–water interface is arguably one of the most important interfacial systems because of its deep and pervasive effects in nature (on abiotic and biotic systems) and technology. In nature, mineral–water interfaces are the principal site of low-temperature geochemical processes at and near Earth's surface. These processes, including dissolution and precipitation of primary minerals, as well as adsorption and incorporation of trace impurities, exert a powerful influence on the natural geochemical and biogeochemical cycles in our environment and effectively control the compositions of groundwaters, surface waters, the oceans, and, to a large extent, the atmosphere. For example, the dissolution of crustal minerals releases primary nutrients (e.g., Ca, K, PO_4, Fe, Mn) that are necessary to sustain life, leads to the formation of clay minerals that are fundamental for soil formation, buffers the acidification of watersheds, and is the primary sink for atmospheric of CO_2 over long times [1,2]. Biological control of growth and precipitation of minerals from fluids is critical to the development of both microorganisms and higher forms of life [3–5]. The control that microorganisms exert on their microenvironments, and in some cases their macroenvironments, is exhibited in their ability to nucleate specific mineral phases that, in many cases, are not the equilibrium phase (e.g., calcite vs. aragonite) and in their ability to control the texture and orientation of the crystal phase [3,6–9]. This control is fundamental to the formation of exoskeletons (e.g., derived from calcium carbonate and silica) and bone materials (e.g., phosphates such as apatite). Skeletal materials in some cases derive from single crystals having exquisite shapes and textures that are biologically controlled [10]. The dissolution of bone and skeletal materials (i.e., demineralization) has also been studied intensively and is an important process leading to diseases such as osteoporosis [11,12]. Water films on particle surfaces are of primary interest in areas such as atmospheric chemistry [13,14], where such films may play an important role in mediating reactions with other atmospheric gases (e.g., NO_x and SO_x).

The solid–liquid interface is also critical in many areas of human activity, including various technological and industrial processes. The adsorption and/or incorporation of contaminant species into mineral phases in underground aquifers leads to the sequestration and/or oxidation–reduction reactions of toxic elements in groundwater [15]. Permeable reactive barriers represent a technology to purify contaminated water as it flows through the ground, either by adsorption or through chemical reactions, instead of more intrusive and costly ex situ procedures [16,17]. Crystal growth

of minerals in aqueous media is central for a broad range of technologies [18–24] and can be controlled through inhibition and/or adsorption of impurities [25–28] or incorporation of impurity ions [29–31]. Noble-metal catalyst formation is initiated by the adsorption of heavy-metal complexes from aqueous solutions to oxide substrates [32].

Although the origins of modern surface science were closely coupled with the development of ultra-high vacuum technology (UHV) and various electron- and ion-based techniques [33], the key feature of all of these phenomena and processes is the presence of a liquid, typically aqueous, phase that is largely incompatible with UHV technologies. Progress in this vast important area of surface science was limited until the late 1980s when a resurgence was driven by driven by the development of new capabilities to make direct observations of the structure and properties of the liquid–solid interface, both in situ and with sub-Ångstrom resolution and sensitivity. Most notable was the development of scanning probe microscopies [34,35], and various synchrotron X-ray techniques [36–42], which together have enabled new classes of in situ nanoscale and atomic-scale studies of mineral–fluid interfaces.

Much attention has been given to solid–liquid interfaces in the past few decades, particularly solid–water interfaces [43–51]. Although significant strides have been made in recent years, structure and bonding at the mineral–fluid interface are only beginning to be understood for the simplest minerals [52]. A key feature of solid–liquid interfaces is the perturbation of the liquid structure near the solid surface (Fig. 1). Although the substrate and fluid structures far from the interface are known, the behavior of the first few fluid layers is unknown and likely to be different. This interfacial structure may have crucial influence on solid–liquid interfacial properties, notably diffusion, solute adsorption, and dielectric properties. For instance, the perturbations on the fluid side of the interface in Fig. 1 might be characterized by the ''adsorption'' of one or more water layers, with the development of a ''modulated liquid'', or with the formation of ''ice-like'' layers. These layers may or may not have any lateral registry with respect to the substrate lattice. Here, we refer to water in this transition region as ''interfacial water''. These various conceptual models suggest different properties of interfacial water. Theoretical studies predict that the ''hard-wall'' effect of a smooth solid surface would constrain interfacial liquids, resulting in a layered density profile [53–55] analogous to the hydration shell surrounding an isolated solute in a bulk water [56]. Since these early predictions, evidence for such interfacial layering of liquids (especially water) near interfaces has come primarily from molecular dynamics simulations [57–68] suggesting that layering may be a generic effect at the solid–liquid interface and it may be present at many different types of substrates, ranging from silicates to metals.

Until recently, experimental evidence that interfacial fluids develop structure (i.e., have a density profile that is distinct from a smoothly varying step function) has come from two sources. First, measurements of the forces between two muscovite–mica surfaces as a function of surface separation (using the ''surface forces apparatus'', or SFA) showed dramatic oscillations in force–distance curves for aqueous and non-aqueous solutions [69,70]. These oscillations are associated with the removal of individual fluid layers separating the muscovite surfaces and suggest that

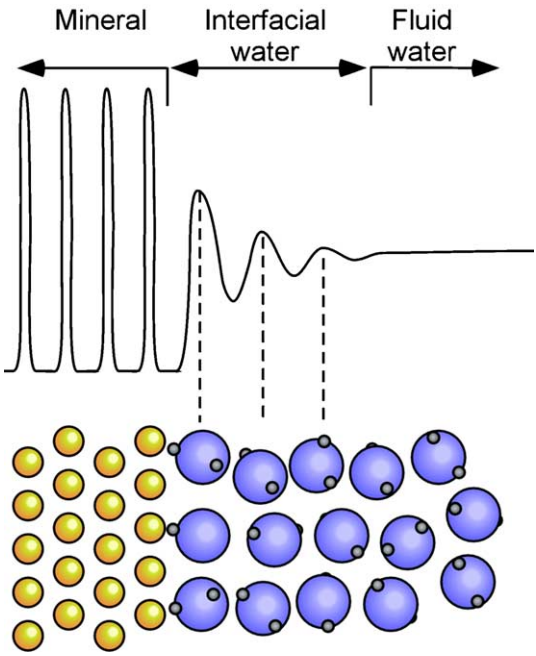

Fig. 1. Schematic density profile of interfacial water near the solid–aqueous interface. The nature and range of any interfacial ordering, indicated by the oscillatory density profile near the interface, is to be determined.

the interfacial fluids form discrete layers, at least when confined between two surfaces. Additional measurements led to new insights into the properties of these confined water layers [71–73]. Qualitatively similar layering of water has been observed in scanning force microscopy [74] and scanning tunneling microscopy [75] as the apparent formation of integral numbers of water layers separating the tip and sample. More recently, unexpected dynamics of water were observed at the "Janus interface" of water confined between hydrophobic and hydrophilic surfaces [76,77]. More direct structural insight into these phenomena has derived largely from neutron scattering measurements of various hydrated clay minerals that confine thin water films in interlayer regions [57,58,78–81]. These measurements directly demonstrated that fluids, including water, can develop layered structure when confined between silicate planes. The results, however, leave unanswered a central question: Is the observed structure of confined water layers an intrinsic property of free solid–fluid interfaces? Or, is it simply the result of confinement of fluids in the nanoscale spaces between solid surfaces?

In recent years, substantial progress has been made in direct observation of solid–liquid interfaces with non-aqueous fluids, mostly by using X-ray scattering techniques. Liquid density oscillations near solid surfaces have indeed been observed in systems ranging from liquid metallic gallium adjacent to the surface of diamond [82] to normal molecular liquids adjacent to oxidized silicon surfaces [83–85]. In

the latter case, direct evidence for such oscillations was obtained for both thin films and macroscopically thick layers, suggesting that the layering was intrinsic to the isolated interface. This work also established that layering was not intrinsic to all systems and that shear flow could either disrupt or induce molecular layering [86]. In each of these measurements, relatively weak layering of the fluid was observed within ~2–3 molecular layers of the surface [82,83]. Other measurements addressing the nature of the liquid phase adjacent to the solid substrate have shown that liquid Pb adjacent to a silicon surface has a 5-fold local symmetry, confirming earlier theories that supercooling is due to the formation of icosahedral complexes that act as the nucleation barrier to solidification [87]. Recent measurements have revealed distinct layering of normal liquids confined between hard walls [88,89], as well as rare gases confined in nanometer-sized cavities in aluminum [90]. The first direct experimental observations of density oscillations at solid–aqueous interfaces were observed adjacent to conducting substrates under potentiometric control (i.e., in the presence of applied electric fields). Under such conditions, it was generally assumed that such layers would be ice-like [91–94].

An additional complexity inherent to mineral–water interfaces derives from the fact that most minerals are insulators and potentiometric control is normally inapplicable for such studies. Instead, the pH-dependent charge at mineral surfaces is associated with acid–base behavior of oxide and silicate surfaces (e.g., protonation reactions of surface oxygens). This phenomenon is a central component to surface complexation models that attempt to explain and/or predict surface protonation reactions and ultimately reactivity [95–98]. Spectroscopic studies clearly show evidence that mineral surfaces interact with the aqueous phase through chemical reactions, for example, to form hydroxylated surface functional groups [99–103]. Observation of differences in water thin-films on glass substrates formed by vapor phase adsorption and in the vicinity of the bulk meniscus revealed the structure of water wetting films [104]. Neutron scattering measurements are also able to probe solid–water interfaces [105] and have probed the structure of water at non-wetting surfaces revealing a water density deficit associated with hydrophobic interactions [106]. Information on the *orientation* and *spectroscopy* of aqueous solutions near mineral surfaces was also obtained by non-linear optical spectroscopy measurements of interfacial water molecules near silica and corundum surfaces [107–111], as well as recently for a quartz surface [112].

In spite of all these studies, little is known from direct experimental observations about the *structure* of water near isolated mineral–water interfaces [38,52], including the location of interfacial species, their registry with respect to the substrate lattice, and the extent of order (both vertical and lateral). In analogy to the hydration layer that surrounds ions in aqueous media, any reactions that take place at the mineral–water interface should be controlled by transport through a surface hydration layer at the mineral–water interface. The properties of hydrated ions are well understood, and vary systematically with elementary parameters (e.g., ion size and hydration energy) [56]. In contrast, direct experimental knowledge of surface hydration layer properties at mineral–water interfaces is extremely limited. The properties of mineral surface hydration layers, including degree of ordering and spatial extent, are likely to

be controlled by the structural and chemical properties of the substrate, including the functional groups expressed at the surface, and the unit cell size and its symmetry. An understanding of these interrelationships between hydration layer properties and mineral surface structures is critical for developing a fundamental understanding of mineral–water interface processes.

In this review, we discuss the new insights into the structure and properties of the mineral–water interface derived from high-resolution synchrotron X-ray scattering techniques. We explore both the mineral and the fluid sides of the mineral–water interface and their interrelationships. We take a broad definition of minerals to extend to any naturally-occurring inorganic crystalline phase (or, in some cases, synthetic equivalents) including the major mineral classes of ionic crystals, oxides, silicates, phosphates, and sulfates but excluding metals and semiconductors that generally do not play an important role in interfacial processes in natural environments under ambient conditions (297 K, 1 atm). Consequently, we will not review extensive developments in well-studied areas such as metal–aqueous electrochemistry, which has been reviewed previously [113–118]. Nor do we intend to duplicate the recent reviews of water properties and organization at solid substrates as derived from various macroscopic and spectroscopic studies [47,119–124], or oxide surface structure and reactivity at ultra-high vacuum conditions [125–127]. Instead, our goal is to review and discuss the recent developments in the structure of mineral–water interfacial systems as derived exclusively from X-ray scattering measurements and to integrate the new results with recent theoretical and experimental developments. The objectives of this review are (1) to help bridge the information gap that currently separates our macroscopic concept of these systems from the critical molecular-scale behavior that has remained largely obscure and (2) to point out directions for further work in this area. The central issues that we address here are the interrelationships between the nature and composition of the substrate lattice, the identities and structures of surface functional groups that are formed by the truncation of the lattice in aqueous environments, and the structure of the interfacial water adjacent to the mineral surface. We review the results of each mineral system that has been studied to date, separating those studies that were performed in contact with fluid water (i.e., mineral–water interface, Section 2) from those done in contact with humid air and/or water vapor in vacuum (i.e., mineral–water vapor interfaces, Section 3). Systematic trends and unique features of these systems are discussed in Section 4, along with a discussion of future prospects in this area.

1.2. Structural motifs at the mineral–water interface

The creation of a surface (e.g., by cleaving a crystal) leads inevitably to the formation of undercoordinated surface species. Vacuum studies of surfaces have identified and characterized structural changes at surfaces, including local structural relaxations of the surface atoms, surface reconstructions, and even large-scale instabilities such as surface faceting [128] that are ultimately derived from the undercoordinated surface atoms. An example of an undercoordinated lattice cation at a mineral surface is the 5-fold coordinated Ti atom on the rutile (1 1 0) surface [129]. For minerals in

aqueous environments, however, immersion in water can substantially reduce the large surface energy associated with broken bonds through formation of surface complexes via chemical reactions with the aqueous phase that restore the cation's coordination shell. This results in a substantial reduction in the surface energy and thereby makes mineral–water interfaces more thermodynamically stable than they would be in the absence of water. This apparent passivation of mineral surfaces by reaction with water contrasts markedly with the distorted structures observed at elementally clean yet energetically unstable surfaces found in ultra-high vacuum environments.

Typical mineral–water surface sites are seen on the hydrated rutile (1 1 0) surface, containing two surface oxygen sites (Fig. 2). Surface sites having a singly-bound oxygen containing species are generically referred to as non-bridging oxygen (NBO) sites (Fig. 2). This NBO completes the oxygen coordination shell surrounding the 5-fold coordinated Ti atom found in vacuum studies. A second type of surface functional group common to mineral surfaces is the bridging oxygen (BO) site. Together, these sites create a surface oxygen lattice that interacts directly with the solution. While this nomenclature emphasizes the geometry of these sites, they may exist in different protonation states (e.g., an NBO might correspond to an associatively adsorbed water molecule or an dissociatively adsorbed hydroxyl group). The reactivity of these groups may also be controlled in part by the substrate crystal structure. For instance, BOs that have no broken bonds due to creation of the surface are likely to be less reactive than those BOs that are undercoordinated with respect to the bulk lattice.

1.3. Chemical properties of surface functional groups

The properties of surface functional groups generally control the reactivity of mineral–water interfaces. It is, however, difficult to make general statements concerning the nature of BOs and NBOs, given the diversity of crystal surface structures and compositions. Much of our current understanding is based on quantum-mechanical theoretical studies correlating the properties of surface functional groups with crystal chemistry and solution conditions [51,130–134]. These calculations typ-

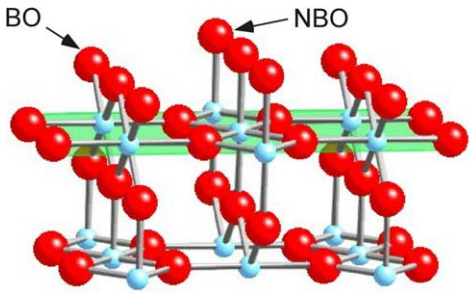

Fig. 2. Structural motifs at the mineral–water interface. Here the rutile (α-TiO_2) (1 1 0) surface is shown with bridging oxygen (BO) and non-bridging oxygen (NBO) sites as determined recently with X-ray diffraction [223]. This creates a surface oxygen lattice that is the primary contact with the aqueous phase.

ically can include only a relatively small number of water molecules because of the limitations of the computing resources required to perform the calculations. This approach is most appropriate for understanding water adsorption at mineral surfaces in vacuum and/or humid environments (where the water film thickness is limited). Insights from such calculations may not be fully applicable for understanding properties of mineral surfaces in contact with macroscopic quantities of water, but they are nevertheless quite useful when available. Recent advances have shown that the Carr–Parrinello ab initio molecular dynamics approach [135] is a powerful technique for understanding the properties of water [136,137] and water near solid–water interfaces [134,138–141] and should be an important tool for understanding the mineral–water interface.

Classical molecular dynamics (MD) simulations can incorporate thousands of water molecules and are effective in exploring the phase space of water interaction with a mineral surface (e.g., the interplay between position and orientation). The main limitation of this approach is that it normally uses potential functions that are fitted to match macroscopic properties. These potentials are generally not validated as predictors of surface properties, because of the absence of independent experimental results for comparison with simulations. Conventional MD simulations do not incorporate chemical reactions (among water molecules, ions, and the mineral surface), and therefore care must be taken to ensure that the simulations are representative of the systems of interest.

Phenomenological correlations in bonding behavior at mineral–water interfaces provide useful insights in the absence of high-level theoretical results. The bond valence approach is a simple but potentially powerful formalism originally suggested by Pauling [142] but later developed in more detail by Brown [143–145]. This is essentially an ionic charge distribution model incorporating chemical interactions ranging in strength and character from covalent bonds to ionic interactions and hydrogen bonds. In particular, the bond valence approach provides constraints that relate characteristic bond lengths, coordination numbers, and bond strengths for each atom. This approach has been useful as an independent check on the reasonableness of an experimentally-derived structure (e.g., in crystallography studies), as well as to interpret the interactions of ions with mineral surfaces [38] and their coordination environments within glasses [146]. This approach can also provide additional chemical insight into structures and properties derived by X-ray scattering techniques such as the protonation state of a surface functional group [147], to which X-ray based measurements would be otherwise insensitive.

Because we will make use of the bond valence model throughout this manuscript, the model's concepts are outlined here. Each cation has a valence, V, corresponding to the number of its valence electrons, which is expressed in terms of valence units (v.u.) and is essentially the charge available to form bonds. The bond valence of each bond is governed by the relation $s = \exp[(r_0 - r)/b]$, where r_0 is a parameter specific to a cation–anion bond pair and the respective chemical state of the ions, r is the actual cation–anion bond length, and $b = 0.37$ Å. For any given bonding configuration, the sum of bond valences of a given cation must be equal to the cation's valence (i.e., $V = \sum s_i$). Consequently, longer bonds have a smaller valence (i.e.,

are weaker), and a cation can have multiple bonding configurations ranging from a few stronger, shorter, bonds to a greater number of weaker, longer, bonds. In water, the oxygen valence of 2 can be pictured as being distributed between the two O–H bonds of the water molecules (each with $s = 0.8$) plus two hydrogen bonds with a valence of 0.2 each. If the oxygen valence due to its intra-molecular (O–H) bonds is greater than 0.8, the valence of the two accepting hydrogen bonds will be proportionally reduced.

For surfaces, a direct implication of the bond valence model is that surface bond lengths should decrease relative to their bulk values if the surface atoms retain the undercoordinated environments associated with the bond breaking necessary to create a surface. This is expected because the fixed valence of a surface atom is distributed among fewer bonds, leading to larger bond valence for each bond. Consequently, the bonds of an undercoordinated surface atom should be both stronger and shorter. This has been observed in the case of the rutile (1 1 0) surface studied in vacuum [129], where the Ti–O bond lengths were found to be substantially shorter near the surface.

Within the context of the bond valence theory, the properties of the NBO bonded to a lattice cation Me^{V+} having valence V and bulk coordination CN can be examined. The average valence of each bond (also known as the Pauling bond strength) is $\langle s \rangle = V/\mathrm{CN}$. We make the simplifying assumption that the perturbations of the surface bond valence are compensated locally. This is consistent with the observation that most mineral surface structures in contact with water have only slightly relaxed surface lattices with respect to the bulk truncated lattice. If the NBO perfectly compensates for the exposed lattice cation, we expect that the NBO has a valence due to the NBO–Me bond of V/CN. If the substrate metal cation valence deficit significantly exceeds that of the valence available through hydrogen bonds of a water molecule ($\sim$0.2 v.u. per accepting hydrogen bond), then this valence deficit cannot be satisfied by the adsorption of a water molecule as an intact molecule (i.e., associatively) but could be satisfied by a dissociatively adsorbed water molecule. In this scenario, an adsorbed OH^- will have available for bonding with the surface the $\sim$0.8 v.u. that was taken up by the proton in the water molecule. Consequently, the nature of an NBO (i.e., adsorbed H_2O or OH^-) may be inferred by the properties of the substrate lattice and its lattice cation.

Similar constraints can be developed for BOs. For BOs having a broken bond, the situation is comparable to that of NBOs, and in such cases the nature of any adsorbed species will be sensitive to the substrate crystal structure. In this case, bond valence model predicts that the interaction will be primarily to hydrogen atoms and BOs will either be directly protonated or associated with water molecules through accepting hydrogen bonds. For BOs having no bonds broken to create a surface, the bond valence of the oxygen is completely saturated by bonds with the lattice cations. The result is an inert functional group, as long as the surface atom locations are unchanged with respect to the bulk structure (and the valence of the cation to which the BO is bound is unchanged). The structural relaxations of surface atoms away from their bulk lattice position can, however, lead to moderate reactivity. For instance, the bond valence reduction associated with a Me–oxygen bond

length change of +0.07 Å, typical for mineral–water interfaces, is 0.17 v.u. This valence is similar to that of an accepting hydrogen bond. This shows that nominally "unreactive" functional groups may be accessible for the coordination with water molecules via hydrogen bonding. More generally, the valence of each atom in a structure can be calculated when the full three-dimensional interfacial structure is known to reveal bond valence deficits associated with adsorbed protons and hydrogen-bonded water [147].

A complete understanding of mineral–water interface reactivity must include the pH-dependent development of surface charge that results from proton adsorption/desorption by surface oxygen atoms (especially those of metal (hydr)oxides). Mineral surfaces are characterized by a pH of zero net surface charge, pH_{pzc}, that is specific to each mineral surface [46,148], with the mineral surface having negative and positive charges above and below the pH_{pzc}, respectively. This charging behavior is normally understood with surface complexation models (SCMs), in which mass law expressions describing ion binding at the metal oxide surface are coupled with classical models of the electrical double layer (EDL) [46,96,98,148–156]. This proton charge is compensated by aqueous ions distributed among discrete (i.e., Stern or Helmholtz) planes of cation and anion adsorption, as well as a diffuse layer of ions typically described by Gouy–Chapman theory [46,151,157,158]. A generic 2-pK formalism if often used to describe proton affinity for surface oxygen atoms [98,148,149]. A related approach is the MUlti-Site Ion Complexation (MUSIC) model [152,153] that utilizes the specific crystal surface structure and the bond valence concept [142,143] with an empirical relationship between valence undersaturation and proton affinities of oxygen ligands in bulk solutions to predict surface oxygen proton affinities and site densities.

1.4. Constraints and limits on interfacial water structure

Interfacial water may be expected to exhibit some structural characteristics of ice and/or water, because the uniqueness of these structures comes from the water molecule's structure and its tendency to form hydrogen bonds. The structures and properties of ice and water have been studied for many decades [159–162]. The common solid phase of water (ice-I) is hexagonal ice having lattice parameters $|\boldsymbol{a}| = 4.5227$ Å and $|\boldsymbol{c}| = 7.3671$ Å, near $T = 0$ °C and $P = 1$ bar, where water molecules are ordered in a bilayer structure, as shown in Fig. 3a [163]. Each bilayer has hexagonal symmetry, and the protons are disordered, with the average positions indicated. Each water molecule has four neighboring water molecules: three within the bilayer, and one in the adjacent bilayer. The average O–O spacing in this structure is 2.75 Å, with a bilayer spacing of 3.644 Å.

X-ray and neutron scattering data for liquid water show that the oxygen–oxygen pair distribution function exhibits characteristic layering with a strong first peak near 2.8 Å, followed by rapid dampening of oscillations within 10 Å [160,161,164,165] (Fig. 3b). Similarly, measurements of supercooled water lead to a water correlation length of only ~4 Å that is temperature independent [166]. Both of these observations suggest that perturbations of the bonding and interactions in interfacial water will not

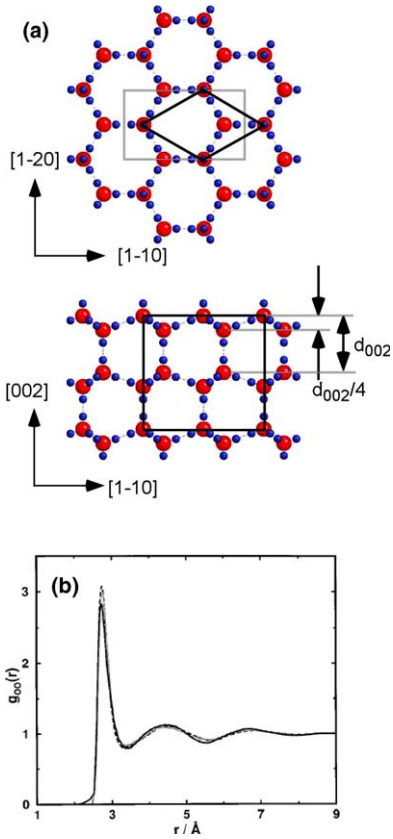

Fig. 3. (a) The structure of hexagonal ice as seen along [0 0 1] (above) and [1 −2 0] (below) with oxygen and hydrogen shown in red and blue, respectively. Hydrogens are shown in all possible sites since they are disordered in this phase. (b) The O–O correlation function in liquid water. Part (b) is reprinted with permission from J.M. Sorenson, G. Hura, R.M. Glaeser, T. Head-Gordon, Journal of Chemical Physics 113 (2000) 9149–9161. Copyright 2000 by the American Institute of Physics. (For interpretation of the references in color in this figure legend, the reader is referred to the web version of this article.)

extend far from source of perturbation (i.e., the interface) unless interfacial water is truly ice-like. Substantial progress has been made recently in understanding the local bonding structure in water and ice, both experimentally and theoretically [167–170]. These studies showed that the hydrogen bond in ice has a covalent component and that the liquid structure disrupts, on average, one hydrogen bond per water molecule. These ideas are contrary to the widely-held notion that water retains the same local bonding structure found in ice structures, but as a disordered random network. Recognizing these important new findings, the level of detail currently available concerning interfacial water structures is generally unable to resolve these features.

In the majority of interfacial water systems studied, the structure has been derived from models optimized through comparison with X-ray scattering data. In this

respect, it is useful to consider the steric constraints on water structure independent of specific chemical (e.g., hydrogen bonding) interactions. A reasonable first approximation is that interfacial water density equals the bulk water density, $\rho_w = 1$ g/cm^3 = 1H_2O/(30.3 Å^3). This suggests that interfacial water films have a two-dimensional (2D) density of $\rho_{2d} \sim \rho_{3d}^{2/3} = 1\ H_2O/(10\ Å^2)$, which is only 11% less dense than water in a hexagonal ice bilayer (0.113 H_2O/Å^2). Assuming that water can be described by the close packing of spheres implies an O–O spacing of 3.4 Å and a layer spacing of 2.77 Å. Note that these quantities are substantially different from those of 2.75 Å and 3.64 Å, respectively, observed in hexagonal ice. This rough analysis illustrates the magnitude and character of the changes that might be found in interfacial water structures having hydrogen bonding structure that is either preserved or disrupted.

1.5. X-ray scattering from mineral–water interfaces

X-rays are an ideal probe of mineral–water interfaces. The ability of hard X-rays ($E > 5$ keV) to penetrate millimeters of water allows in situ studies to be performed at conditions defined by the relevant interfacial processes. X-rays can measure atomic-scale structures, such as the separation of individual atoms or molecules, because X-ray wavelengths are comparable to the size of atoms [171,172]. The interaction of X-rays with matter is understood at a fundamental level, and X-ray based techniques can provide truly quantitative data concerning the arrangements of atoms through a variety of approaches, such as crystallography and X-ray absorption spectroscopy [172]. These characteristics can also be used to study the structure of the mineral–fluid interface (e.g., atomic locations, bond lengths) with sub-Ångstrom precision.

The sensitivity of X-ray scattering techniques to interfacial structures arises from the interference of X-rays scattered from surfaces and interfaces, such as grazing-incidence X-ray reflectivity, surface and thin-film diffraction, crystal truncation rods (CTR) [41,42,173–181], and X-ray standing waves (XSW) [182–188]. These techniques have been used most widely to probe the interfaces of relatively simple materials (e.g., elemental semiconductors and metals) at vacuum–solid and electrolyte–solid interfaces [91,92,189–195]. However, these X-ray scattering techniques are also sufficiently robust to study the surfaces of the more complex mineral materials (e.g., molecular ionic solids, silicates, and oxides) commonly found in natural systems [39,40,126].

Here we briefly review the use of X-ray reflectivity to probe the structure of mineral–water interfaces, particularly to define water structure in the vicinity of mineral surfaces. X-ray reflectivity, simply defined as the ratio of the reflected and incident X-ray fluxes, is typically measured over a broad range of incident angles. X-rays probe structures along the direction of momentum transfer, $\boldsymbol{Q} = \boldsymbol{K}_f - \boldsymbol{K}_i$, where $|\boldsymbol{K}| = 2\pi/\lambda$ is the wave vector of the X-ray photon whose direction is along the photon propagation direction (Fig. 4a). In the simple case of the mirror-like reflection of X-rays from a surface or interface (i.e., specular reflectivity) the structure is probed only along the surface-normal direction. The measurement and interpretation of X-ray reflectivity data (i.e., the angular variation of reflected X-ray intensities

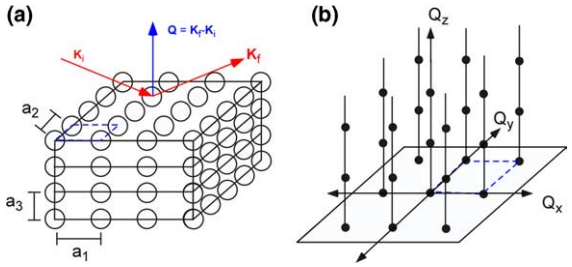

Fig. 4. (a) A truncated crystal having surface lattice spacings $\boldsymbol{a}_1$ and $\boldsymbol{a}_2$ and layer spacing $\boldsymbol{a}_3$. (b) The reciprocal-space structure for the truncated lattice in (a). Crystal truncation rods extend from Bragg peaks along the surface-normal direction.

as a function of incident angle) [41,42,177,178,180] derive from the same theoretical foundation as X-ray crystallography, a technique used widely to study the structure of bulk (three-dimensional or 3D) materials [171,172]. An important characteristic of X-ray reflectivity data is that these techniques are not only *surface sensitive*, but also *specifically derived from the interfacial structure*.

X-ray data for surfaces and bulk materials appear in different forms, as can be seen when scattered the intensity presented in reciprocal space. Surfaces and crystals appear as rods and points, respectively, as shown in Fig. 4. Here, the crystal structure will be described with a surface unit cell (with lattice parameters $\boldsymbol{a}_1$, $\boldsymbol{a}_2$, $\boldsymbol{a}_3$) where $\boldsymbol{a}_1$ and $\boldsymbol{a}_2$ are oriented within the surface plane and $\boldsymbol{a}_3$ describes the vector displacement between equivalent sites in neighboring layers (which need not be along the surface-normal direction, $\boldsymbol{n}$). These parameters will generally differ from the traditional bulk unit cell parameters. The surface reciprocal lattice vectors, $\boldsymbol{b}_j$, describing the location of the Bragg rods can be described by $\boldsymbol{a}_i \cdot \boldsymbol{b}_j = 2\pi\delta_{ij}$. For a rectangular surface unit mesh, $|\boldsymbol{b}_i| = 2\pi/|\boldsymbol{a}_i|$. Within this surface coordinate system, each of the Bragg rods are indexed with integer surface Miller indices (H, K) and a continuous index, L, along the rod.

The relationship between the interfacial structure and the reflected X-ray intensity has been discussed previously in detail, but for completeness it is summarized here. The sensitivity of X-ray diffraction to structure is derived from measurements of scattering intensities. As originally derived by Robinson [180], the integrated scattering intensity, I_{int}, due to a surface or interface is

$$I_{\text{int}} = I_0(e^2/mc^2)^2 T_{\text{cell}}[(A\lambda^3 P/a_{\text{uc}}^2)/\Omega][1/\sin(2\theta)]|F|^2 \Delta Q_z/2\pi, \tag{1}$$

where I_0 is the incident photon intensity (in units of photons per area per second), $r_e = e^2/mc^2$ is the classical electron radius, T_{cell} is the transmission factor of X-rays through the cell, A is the active area of the surface (i.e., the area of the surface that participates in the diffraction measurement), λ is the X-ray wavelength, P is a polarization factor, a_{uc} is the area of the surface unit cell, Ω is the angular velocity in the rocking scan, $1/\sin(2\theta)$ is the Lorentz factor, 2θ is the scattering angle, F is the structure factor of the interface, and ΔQ_z is the length of the surface rod that is integrated in the rocking scan (e.g., due to the finite detector resolution). Therefore, I_{int}, has

units of photons per second. Many of the pre-prefactors in Eq. (1) depend on the details of the scattering experiment and on the choice of spectrometer [196–202]. Normalizing the scattering intensity to the incident beam flux yields the X-ray reflectivity, which is dimensionless.

The structure factor, F, is related to the geometric structure through the relation:

$$F(\boldsymbol{Q}) = \int \rho(\boldsymbol{r}) \exp(\mathrm{i}\boldsymbol{Q}\cdot\boldsymbol{r})\mathrm{d}^3\boldsymbol{r} = \sum f_j(\boldsymbol{Q}) \exp(\mathrm{i}\boldsymbol{Q}\cdot\boldsymbol{r}_j) \exp(-(\boldsymbol{Q}\cdot\boldsymbol{\sigma}_j)^2/2), \quad (2)$$

where $\rho(\boldsymbol{r})$ is the electron density. The second expression is in the form of scattering from individual atoms, where $f_j(\boldsymbol{Q})$, $\boldsymbol{r}_j$, and $\boldsymbol{\sigma}_j$ are the atom scattering factor, position and projected root mean square (rms) vibrational amplitude (along $\boldsymbol{Q}$) summed over all atoms j. The interfacial structure factor in Eq. (2) can be rewritten in a form that allows for substantial conceptual simplification:

$$F = F_{\mathrm{uc}}F_{\mathrm{CTR}} + F_{\mathrm{surf}} + F_{\mathrm{water}}. \quad (3)$$

Each of these terms is identical to the structure factor as described in Eq. (2), except that the summation is over a subset of atoms. F_{uc} is summed only over atoms within a single bulk unit cell; F_{surf} is summed over all near-surface atoms that might be displaced from their ideal bulk lattice positions (typically 2–3 layers deep into the crystal) plus any adsorbed layers attached to the surface; and F_{water} describes the fluid structure above the interface, including any structuring of the fluid near the mineral surface. The structure factor of a truncated crystal (known as a crystal truncation rod, or CTR [176]) is

$$F_{\mathrm{CTR}} = 1/[1 - \exp(\mathrm{i}\boldsymbol{Q}\cdot\boldsymbol{a}_3)], \quad (4)$$

where $\boldsymbol{a}_3$ is the vector separation between neighboring substrate layers, with layer spacing $\boldsymbol{a}_3\cdot\boldsymbol{n}$.

A brief comment on terminology is warranted. Here, X-ray scattering intensity refers to a signal that is proportional to the detector count rate (photons/sec). X-ray reflectivity refers to the scattering intensity normalized to the incident beam intensity which is applicable to both specular and non-specular scattering geometries and is dimensionless. (In the literature, the term reflectivity often refers only to low angle specular reflectivity, and non-specular reflectivity often is referred to separately as crystal truncation rod scattering). In many cases, the data are reported in the form of structure factors. This is obtained by solving for $|F|$ using Eq. (1) where the extrinsic factors are removed from the experimental data. This is a convenient form for analyzing the data since they can be directly compared to structure factor calculations (e.g., using the ROD program [203]) for least-squares optimization of interfacial models.

1.5.1. Sensitivity to interfacial water structures

We illustrate the sensitivity of X-ray reflectivity data to the fluid structure at the mineral–water interface (Fig. 5a) with model calculations (Fig. 5b). Here the substrate is assumed to have a single atom per layer (so that $F_{\mathrm{uc}} = f_{\mathrm{sub}}$, where $f_{\mathrm{sub}} \sim Z$ is the atomic scattering factor of the substrate atom) with a density of 2.3 g/cm^3

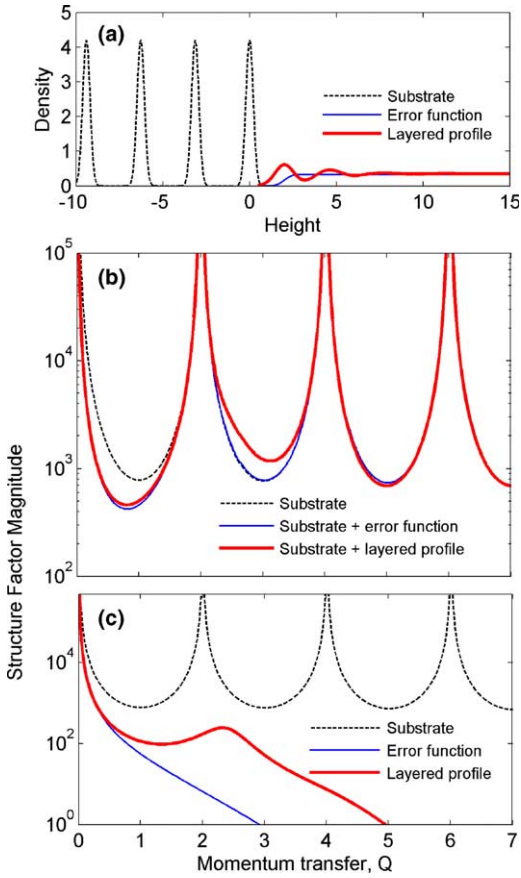

Fig. 5. (a) Model density profiles showing a substrate crystal and two fluid density profiles: a featureless error function profile, and a "layered" profile. (b) Calculated specular reflectivities for the surface in (a) without water, and with the two water profiles. (c) Individual form factors of the substrate lattice and the two water profiles in (a). Note the quasi-Bragg peak due to the layered water profile, whose position is determined by the layer spacing and whose width is determined by the extent of layering.

(typical of many minerals) and layer spacing of 3.14 Å. For simplicity, we assume that the substrate surface atoms are located precisely at the projected bulk lattice positions, and consequently all contributions from the substrate lattice are expressed by $f_{\mathrm{sub}}/[1-\exp(\mathrm{i}\boldsymbol{Q}\cdot\boldsymbol{a}_3)]$. This results in a typical CTR profile (Fig. 5b) showing a continuous intensity variation connecting substrate Bragg peaks, with a minimum structure factor magnitude corresponding to $|F_{\mathrm{uc}}|^2/4$ at the anti-Bragg position (i.e., exactly half-way between Bragg peaks).

The structure factor magnitudes for various interfacial water structures can be calculated. An error function profile has the structure factor

$$F_{\mathrm{water\_erf}} = \mathrm{i}f_{\mathrm{water}}(A_{\mathrm{uc}}\rho_{\mathrm{w}})\exp[-0.5(Q\sigma_0)^2]/Q, \tag{5}$$

where the f_{water} is the scattering factor for a water molecule, A_{uc} is the unit cell area, σ_0 is the rms width of the water interfacial profile, and $\rho_w = 0.033$ Å^{-3}. This produces a monotonically decreasing structure factor for the fluid water (Fig. 5c). The structure factor of a layered water density profile can be written as a CTR in which each layer is successively broadened away from the surface following the form $\sigma_j = [\sigma_0^2 + j\sigma_{bar}^2]^{1/2}$ [40,204]. This function takes the form

$$F_{water\_layer} = f_{water}(A_{uc} d_{water} \rho_w) \exp[-0.5(Q\sigma_0)^2]/\{1 - \exp[-0.5(Q\sigma_{bar})^2] \times \exp(iQd_{water})\}. \quad (6)$$

This formalism results in a structure factor that is similar to that of the error function profile at small Q, but with a quasi-Bragg peak at $Q = 2\pi/d_{water}$ due to the layering of density near the interface. This peak is nevertheless substantially broadened because of the limited spatial extent of the layering. The spatial extent of the water layering can be characterized as the distance at which subsequent peaks in the fluid density profile are not resolved (i.e., the layer spacing, d_{water}, is equal to full width at half-maximum of neighboring peaks). This can be expressed as a correlation length of the interfacial water:

$$L_{water} = d_{water}[(d_{water}/2.355)^2 - \sigma_0^2]/\sigma_{bar}^2 \quad (7)$$

The usefulness of the layered water structure factor is that it recovers the structure factors of both error function profiles and the CTR of an ideal crystal in appropriate limits ($Q \to 0$ in the former, $\sigma_{bar} \to 0$ in the latter).

Calculations of the full interfacial structure factor, $|F_{uc}F_{CTR} + F_{water}|^2$ are shown in Fig. 5b along with a similar calculation of a bare substrate, $|F_{uc}F_{CTR}|^2$. These calculations show that a primary difference between the solid–vacuum and solid–liquid interfaces is a reduction of the structure factor at small Q (<2 Å^{-1}) due to the smaller density discontinuity at the liquid–solid interface in the presence of water [181]. This low Q behavior is not sensitive to the molecular-scale details of the interfacial water structure because it does not yet resolve the individual layers of the fluid structure, as indicated by the nearly identical intensities for the two water profiles. At larger Q (>2 Å^{-1}), the structure factor of the bare surface and that in contact with an error function profile are nearly identical, because the magnitude of the error function structure factor is so small that the modification of the structure factor due to interference of the substrate and water structure factors is negligible (Fig. 5b). However, the structure factor for the layered water profile is distinct from the error function profile because the layered water structure factor has quasi-Bragg peak that is directly associated with the non-monotonic density profile of the water layers in the interfacial region. No single feature in these calculations, however, immediately identifies the modulation as due to the interfacial water. Other phenomena—including surface relaxations, changes in surface stoichiometry, surface roughness, and the substrate unit cell structure factor—also produce modulations in the reflectivity. Because it is not yet possible to simply invert such data to reveal the interfacial structure directly (i.e., through application of "direct methods" routines) an

understanding of the fluid–water structure is best achieved from a full quantitative understanding of the measured intensities through least-squares fitting.

This particular set of calculations (Fig. 5) shows that the changes in the scattering intensity associated with the layered structure factor are negligible beyond $Q \sim 5$–$6\ \text{Å}^{-1}$. This is ultimately due to the weak magnitude of the layered water structure factor beyond the quasi-Bragg peak, which in turn is associated with the assumed spatial broadening of all the fluid–water layers. This results in a strong drop in the intensity due to the Debye–Waller factor in Eq. (2). (Here the sharpest peak in the density profile was assumed to have an rms width of 0.5 Å, which is a reasonable lower limit for liquid-like interfacial water.) In contrast, specifically adsorbed layers (e.g. either ice-like water layers or adsorbed ions) having vibrational amplitudes comparable to substrate vibrational amplitudes will continue to have a strong effect upon the scattering intensity at or beyond $6\ \text{Å}^{-1}$. This suggests that a complete structural characterization of the interfacial structure can be obtained with measurements to $Q \sim 6\ \text{Å}^{-1}$, so that all of the available information on the fluid water structure is obtained. This is especially important because the analysis of the data is, strictly speaking, model dependent. Similarly, non-specular reflectivity data (i.e., when the momentum transfer has a component parallel to the surface plane) is needed to obtain information on the *lateral* structure of interfacial water. The non-specular rods will be modulated similarly to the specular rod discussed above if the interfacial water structure consists of discrete lateral adsorption sites or if the fluid water profile is laterally modulated with a Fourier component coincident with the surface lattice. On the other hand, the interfacial structure will make no contributions to the non-specular CTRs if it is only vertically modulated (i.e., as a 2D liquid).

1.5.2. Sensitivity to mineral surface termination

Many minerals are *layered* materials in which the electron density profile can be separated into >1 distinct planes of charge within the unit cell. Therefore one must first determine the terminating plane of the crystal before attempting to optimize the detailed mineral–water interface structure. This is non-trivial because X-ray reflectivity data cannot be inverted to reveal the structure in a model-independent manner. Instead, it is usually necessary to determine the structure by comparing the data to various structural models. The likely terminating plane of a surface prepared by cleaving might be determined as the plane that minimizes the number of broken bonds [125]. This approach is inapplicable to growth surfaces and/or to surfaces that are polished.

A destructive interference phenomenon (“termination interference”) has been observed in systems in which the location of an intensity pseudo-node (i.e., a sharp intensity minimum with a non-zero minimum intensity) has been related directly to the terminating plane of the mineral through a “finger-print” assessment derived from a visual comparison of model-calculated and measured intensities. This pseudo-node is observed over and above the inherent orders-of-magnitude intensity variation due to the CTR form factor, $|F_{\text{CTR}}|^2 = 1/\sin^2(Qc/2)$, which is present for any interfacial scattering system. Systems where this has been observed include $YBa_2Cu_3O_{7-\delta}$ [205], Si(1 1 1) [206,207], β-alanine (0 1 0) and α-glycine (0 1 0)

[208,209], KDP (101) [210], benzamide (001) [211], orthoclase (001) and (010) [212,213], muscovite (001) [214], potassium dichromate (001) [215], and fluorapatite (100) [216]. This phenomenon is illustrated for a model structure (Fig. 6) having two distinct layers (e.g., "A" and "B"), each with two atoms per layer in arbitrary positions and with arbitrary scattering amplitudes. Model calculations show that such a structure often results in an intensity node whose position along the CTR is determined by the terminating plane of the crystal. In this case, as is often observed experimentally, the intensity node is found just below or above the first-order Bragg peak along a CTR (i.e., $L \sim 1$ r.l.u. for the specular rod) for the A and B terminations, respectively. A general explanation of this phenomenon [217] shows that it is the result of destructive interference of X-rays scattered separately by the A and B layers. The cause of this interference is a node in the substrate structure factor (F_{uc} in Eq. (3) when there exists a structural relationship between the A- and B-layers (e.g., inversion symmetry). The node location, L_{Ao} (in reciprocal lattice units), is determined by the substrate crystal structure through the approximate relation: $L_{Ao} = \{2[\langle X_A\rangle - \langle X_B\rangle]\}^{-1}$ where, for example, $\langle X_A\rangle$is the reduced center-of-mass location of the A layer's electron density profile, [or, $\langle X_A\rangle = \sum(f_{Ai}\boldsymbol{r}_{Ai}\cdot\boldsymbol{n})/(\boldsymbol{a}_3\cdot\boldsymbol{n}\sum f_{Ai})$]. This shows that the node is found at $L_o < 1$ r.l.u. ($L_o > 1$ r.l.u.) when the center-of-mass

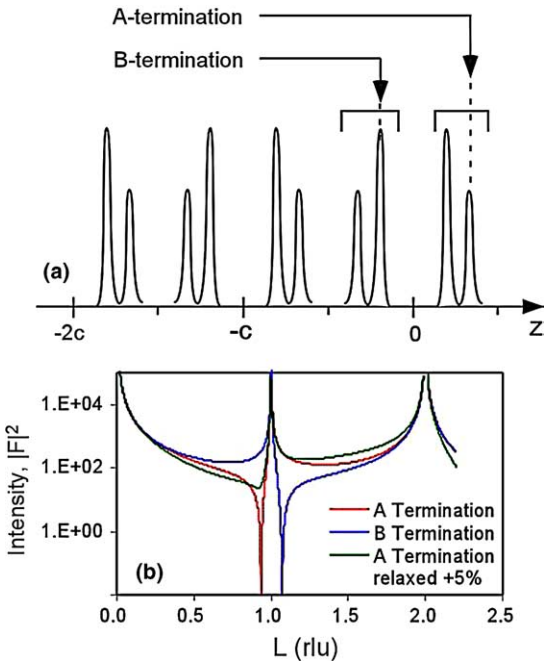

Fig. 6. (a) The density profile of a model layered crystal having two distinct layers with inversion symmetry. (b) Calculated intensity profiles for the A- and B-terminated lattices. Notice that the location of the node (either just above or below the (001) Bragg peak) is determined by the choice of terminating plane.

separation of the outer two layers is greater (less) than half the substrate lattice constant. Further, this node in the substrate structure factor will generally be observed as a pseudo-node in the measured intensity (Eq. (1)) with a non-zero intensity minimum because of the inclusion of surface structural relaxations. For crystals consisting of layers not related by symmetry (i.e., with structure factors not equal in magnitude), destructive interference will lead to a modulation of the reflectivity, making the termination interference generally more difficult to observe.

1.5.3. Resolution

The ability to make definitive statements concerning a structure is closely coupled to the spatial resolution in a scattering experiment which is in turn determined by the angular range of data. Generally, the broadest data range in reciprocal space results in the narrowest spatial resolution in direct space. Given the complexity of many mineral surfaces, high-resolution data are needed to resolve the various contributions to the interfacial structure (e.g., lattice cations, surface oxygens, adsorbed water, etc.). To visualize the effect of resolution, the *effective* electron density of a single atom can be described as a Gaussian function, in which the rms width has contributions from the intrinsic distribution σ_0 deriving from the actual rms width of the atom distribution (e.g., due to vibrations), and extrinsic contributions due to the resolution of measured data, σ_{res}. This effective width can be written as $\sigma_{eff} = (\sigma_0^2 + \sigma_{res}^2)^{1/2}$ where $\sigma_{res} = 1.1/Q_{max}$ [40,218]. This formula derives from an analysis of the two equivalent definitions of the Patterson function [171] and assumes that the data ranges from $Q = 0$ to Q_{max}. This leads to an effective full width at half-maximum (FWHM) associated with the resolution of $\sim 2.6/Q_{max}$. This result is similar to the relation describing the spatial resolution derived by applying Rayleigh's criterion to the Patterson function, which leads to a spatial resolution of π/Q_{max} and is, in turn, identical to the resolution obtained by discrete Fourier synthesis [219]. This shows that data having a value of $Q_{max} \sim 6$ Å^{-1} leads to a spatial resolution of ~ 0.5 Å.

It is useful to plot the derived structure using the resolution-broadened rms widths [40,218], which we refer to as a "resolution-broadened electron density profile". Features that are not visually distinguished in a resolution-broadened profile are therefore not resolved by the data and can be expected to be model-dependent. (Experimental data can retain sensitivity, however, to features of the structure that are not resolved.) In contrast, features that are resolved appear as discrete features and are likely to be largely model-independent. This provides a straightforward way to assess the uniqueness of a structural model.

2. Mineral–water interface structures

The mineral–water interface is conceptually and experimentally straightforward to create. A mineral is placed in contact with an aqueous reservoir that has been pre-equilibrated with the mineral and consequently is thermodynamically stable with respect to reactions (dissolution, growth, etc.). This reproduces the essence of inter-

faces present in nature but with well-defined interfacial structures that can be studied in great detail. These systems, perhaps more than any other interfacial systems that have been studied in surface science, can provide direct insight into the structures and processes that are present in nature.

The study of mineral–water interfaces with X-ray scattering poses certain inherent challenges. Measurements need to be done in the presence of a macroscopic water film that will attenuate the X-ray beam intensity (and consequently increase background signals). The most straightforward geometry is the "transmission cell" (Fig. 7a), in which the sample is held in contact with a macroscopic water layer (>1 mm thick). Because the attenuation length of X-rays in water is ~10 mm at ~20 keV, a substantial amount of incident beam attenuation occurs even for modest samples (~3–5 mm). Most measurements are therefore performed in a "thin-film" cell in which a thin (~8-μm-thick) plastic window (e.g., polyimide) holds a water film (whose thickness may be as small as ~2 μm) in contact with the mineral surface (Fig. 7b). In this geometry, the linear attenuation of X-rays is minimized, and the signal-to-background ratios are maximized. Increasing the photon energy to minimize attenuation and maximize signal-to-background ratio is effective only to photon energies of ~20 keV, at which energy the cross section for Compton scattering from low-Z elements (such as C and O) begins to dominate. Any increased penetration of the incident beam into the substrate crystal also proportionately increases the background signals from the substrate lattice [210]. The substrate background signal is often larger than the background from the plastic window and the thin water layer [40]. Under these circumstances background levels are intrinsic to the particular substrate being measured and are controlled though careful choice of photon energy or scattering geometry.

A significant advantage of these sample geometries is that they allow measurement under equilibrium, or near-equilibrium, conditions. Under these circumstances, damage that is imparted to the crystal surface by the X-ray beam (e.g., roughening) can heal and return to the equilibrium state [220]. In some cases, care must be taken with the thin-film cell to ensure that the environment above the plastic window is

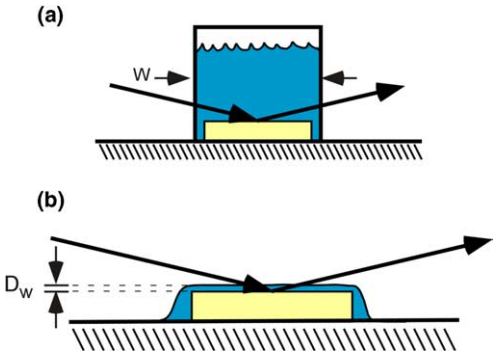

Fig. 7. Schematics of the (a) transmission and (b) thin-film cells for probing the mineral–water interface.

controlled to present modifications to the solution chemistry by reactions with atmospheric gases (e.g., CO_2) that diffuse through the plastic window. In this section we review the individual results of X-ray scattering studies at mineral–water interfaces. The systems and results are briefly summarized in Table 1.

2.1. Oxides

2.1.1. Quartz (101) and (100)

Quartz (α-SiO_2) is second only to feldspars as the most abundant mineral in Earth's continental crust. The quartz structure consists of corner-sharing silicon tetrahedra that form spirals with trigonal symmetry. Quartz is a hexagonal lattice with lattice spacings of $|\boldsymbol{a}| = 4.9137$ Å and $|\boldsymbol{c}| = 5.4047$ Å. Two quartz–water interfaces have been studied with X-ray reflectivity: the $(10\bar{1}0)$ and $(10\bar{1}1)$ surfaces, corresponding to the prismatic and pyramidal faces (referred to as the (100) and (101) surfaces, respectively) of natural growth surfaces of Herkimer "diamonds". The (101) pyramidal surface is the simpler of the two quartz surfaces in having only one likely termination because the lattice structure forms a distinct and stoichiometric layer perpendicular to the (101) surface. The (101) surface unit mesh is oblique, with spacings of $|\boldsymbol{a}_1| = 7.307$ Å, $|\boldsymbol{a}_2| = 4.913$ Å separated by an angle of 110.9°, and a layer spacing of 3.3418 Å (Fig. 8a). This surface is expected to be terminated by two NBOs per surface unit mesh having an area of 33.8 $Å^2$.

Specular X-ray reflectivity measurements revealed a CTR profile for quartz that is nominally featureless, with neither substantial modulations nor sharp intensity minima commonly associated with layered crystals [221] (Fig. 8b). Analysis of these data

Table 1
Summary of water structures at mineral–water interfaces

Mineral	Surface	Formula	Vertical order	Lateral order	Ref.
Quartz	(100)	SiO_2	1 Layer	I[a]	[221]
	(101)		1 Layer	I[a]	
Ruthenium dioxide	(110)	RuO_2	0–2 Layers	Y	[93,234]
	(100)		1 Layer	Y	[235]
Rutile	(110)	TiO_2	1 Layer	Y	[223]
Calcite	(104)	$CaCO_3$	1 Layer (two heights)	Y	[255,256]
Barite	(001)	$BaSO_4$	1 Layer	I[a]	[218]
	(210)		1 Layer	I[a]	
KDP	(101)	$KH_2(PO4)$	n.o.[b]	n.o.[b]	[210,264]
	(100)		n.o.[b]	n.o.[b]	
ADP	(101)	$NH_4H_2(PO_4)$	n.o.[b]	n.o.[b]	[265]
Fluorapatite	(100)	$Ca_5(PO_4)_3F$	2 Layers	I[a]	[216]
Muscovite	(001)	$KAl_2(Al,Si_3)O_{10}(OH)_2$	2 Layers + MF[c]	I[a]	[214]
Orthoclase	(001)	$KAlSi_3O_8$	2 Layer + MF[c]	I[a]	[212,213]
	(010)		2 Layers + MF[c]	I[a]	

[a] Inferred.
[b] Not observed.
[c] Modulated fluid.

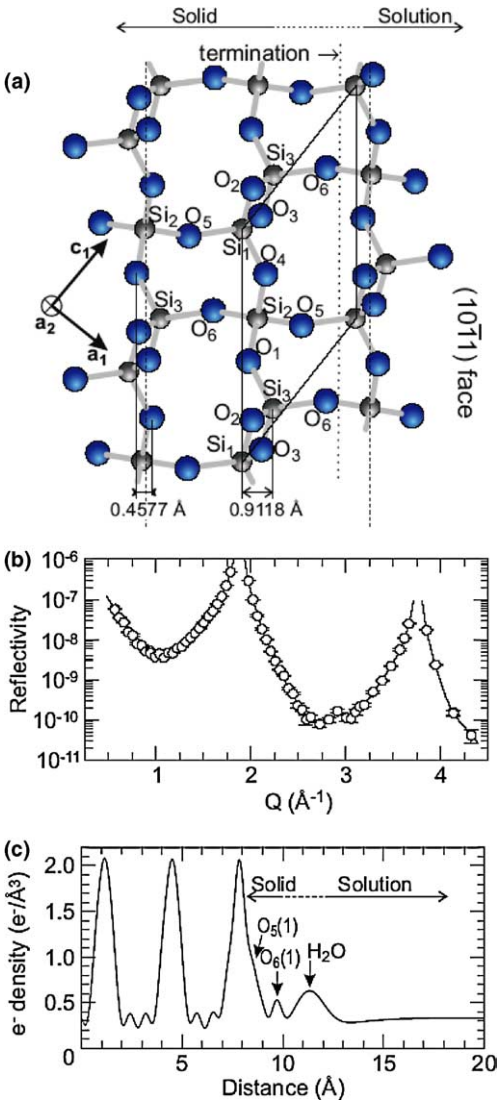

Fig. 8. (a) Schematic structure of the quartz lattice with the (1 0 1) face shown in side view. (b) Specular CTR data of the quartz (1 0 1)–water interface. (c) Derived ''resolution-broadened'' electron density profile from the data in (b) that includes the effect of the finite experimental resolution. These figures are reprinted from M.L. Schlegel, K.L. Nagy, P. Fenter, N.C. Sturchio, Geochimica et Cosmochimica Acta 66 (2002) 3037–3054, with permission from Elsevier.

led to the derived electron density profile shown in Fig. 8c and confirmed that the (1 0 1) surface is terminated by a complete SiO_2 layer, consistent with two surface tetrahedra per unit mesh, with oxygen coordination shells of each completed through the formation of a NBO. Above this fully coordinated silica layer was an additional

discrete layer 1.6 Å above the NBO, followed by a featureless water density profile corresponding to the density of fluid water. Silicon atoms in the outermost quartz layer were vertically displaced by <0.2 Å, with small to negligible displacements in subsequent layers. The surface oxygens were also displaced from their expected bulk-like positions, with vertical displacements of 0.2 Å and 0.4 Å for the two NBOs.

The derived coverage of the adsorbed water layer on quartz (1 0 1) is $\sim 1.8 \pm 0.15$ water molecules per unit mesh (or one water per 19 Å^2). This coverage is equivalent to the density of NBOs on that quartz surface and, interestingly, is substantially smaller than the expected 2D density of a dense water layer (one water per 10 Å^2). This result indicates a degree of crystallographic control over the adsorbed water. Because the specular reflectivity data are insensitive to the lateral location of the adsorbed water molecule, we can only speculate on the relationship of the adsorbed water with the substrate lattice. This water layer is found at a height of only 1.6 Å above the outermost NBO but ~3.1 Å above the outermost BOs. This latter height is comparable to but somewhat larger than the expected value of ~2.8 Å associated with a hydrogen bond between the adsorbed water and the BO.

We can assess these observations from the perspective of bond valence theory. Silicon atoms in the quartz lattice have 4/4 = 1 v.u. per Si–O bond. Therefore an undercoordinated Si atom at the surface cannot associatively adsorb a water molecule. Instead the Si atom is more likely to adsorb an OH^- (0.8 v.u.) to compensate its valence deficit, leaving 0.2 v.u. that might be accommodated by surface structural relaxations that decrease the Si–O bondlength in the NBO. The BO has no associated broken bonds, and therefore its valence is fully saturated through its existing bonds with Si and it is expected to be largely unreactive. Its availability to hydrogen bond with water, however, is closely related to the surface relaxation, because an increase in the Si–O bond length of the BO would decrease its associated Si–O bond valence, thereby freeing up some valence for hydrogen bonding between the BO and adsorbed water. In fact, one of the BOs is relaxed outwardly suggesting an increase in the Si–O bond length. The observed 3.1 Å height therefore suggests the possibility of a weak donating hydrogen bond between the adsorbed water and the BO.

The combined density of the NBO and adsorbed water molecules for the quartz (1 0 1)–water interface is $\sim(1.8 + 2)/33.8 = 0.11$ water/Å^2, consistent, within error, with the expected value of 0.1 water/Å^2 for a dense water layer. Therefore, the adsorbed water and NBOs create a dense layer with minimal corrugation (~1.5 Å) that acts as a template upon which any fluid water structuring can develop. In many respects, this layer resembles the hydration layer observed at the muscovite–water interface [214,222] in which two distinct layers of adsorbed water are observed (Section 2.5.1). In fact, one might expect that this surface could act as a template for ice-like layers if epitaxy between such a layer and the surface was favorable, as found for muscovite. At first view, the correspondence between the hexagonal ice structure and the structure of the quartz (1 0 1) surface appears to be very favorable. For instance, the surface unit cell area of quartz (1 0 1) differs by only 4% from twice the hexagonal ice unit mesh area (33.8 Å^2 vs. $2 \times 17.6 = 35.2$ Å^2). The vertical displacement between the NBO and adsorbed water (~1.5 Å) is similar to the separation of water molecules within a single bilayer of hexagonal ice (0.92 Å). The angular separation between

surface lattice vectors (110° vs. 120°) is also similar for the two structures. Yet the absence of evidence for any extended layering suggests that the continuous water profile above the adsorbed water layer is essentially fluid and poorly ordered. This finding may, in part, be related to geometric or chemical effects. The geometric influences over the structure are derived from the non-hexagonal symmetry of the quartz (1 0 1) surface unit mesh which furthermore has two inequivalent NBOs that are asymmetrically arranged within the unit mesh. The lack of hexagonal symmetry could prevent any simple lattice matching even if the lattice spacings are favorable. Chemical influences derive from the observation that the quartz (1 0 1) surface is terminated with a hydration layer apparently consisting of a hydroxyl as the NBO and an adsorbed water molecule resulting in a chemically modulated surface. In comparison, the muscovite surface is terminated with two adsorbed water molecules (possibly including an adsorbed H_3O^+ ion). This chemical heterogeneity of the quartz (1 0 1) hydration layer could also disrupt a hydration network that might otherwise lead to layering of water above the surface hydration layer.

The behavior of the quartz (1 0 0)–water interface is essentially similar to that of the quartz (1 0 1)–water interface [221]. The (1 0 0) surface is rectangular with lattice spacings of $|\boldsymbol{a}_1| = 5.404$ Å and $|\boldsymbol{a}_2| = 4.914$ Å with a surface unit mesh area of 26.55 Å^2 and a layer spacing of 4.2515 Å. Unlike the (1 0 1) surface, the (1 0 0) surface can be terminated in one of two manners, but determination of the terminating plane for this surface is non-trivial because the two terminations give identical reflectivity profiles when calculated for ideally-terminated lattices [221]. This result is associated with properties of the quartz structure along [1 0 0] in which the α- and β-planes are exactly displaced by $d_{10-10}/2$ [217]. Nevertheless, in the presence of surface structural relaxations the two terminations can be distinguished; the β-termination was observed for two of the three samples that were studied. Reflectivity data for the third sample was consistent with a mixed termination of α- and β-terminated planes, with 2/3 of the surface covered by the β-termination suggesting that the actual termination is controlled by the growth conditions. As for the (1 0 1) surface, the (1 0 0) surface was terminated by a layer that consisted of a mixture of NBOs and adsorbed water molecules. Again, no evidence is found for any layering of fluid water above the adsorbed water layer suggesting fluid-like water structure with minimal layering, consistent with the behavior observed for the (1 0 1) surface.

2.1.2. Rutile (1 1 0)

Rutile (α-TiO_2) has been studied extensively by a wide array of surface analytical techniques and is generally viewed as the model oxide surface [127]. Rutile has a number of applications including its use as a catalyst, as a pigment, and as a coating (e.g., for biological implants). The (1 1 0) surface is the most widely studied surface of rutile. It has a rectangular unit mesh with surface lattice dimensions of $|\boldsymbol{a}_1| = 6.497$ Å along [−1 1 0] and $|\boldsymbol{a}_2| = 2.959$ Å along [0 0 1], and an area of 19.22 Å^2 (Fig. 9a and b). The unit cell has two equivalent layers along the surface-normal direction with an A–B stacking so that the non-primitive unit cell has a dimension of 6.497 Å along the surface-normal direction but a layer spacing of 3.249 Å. The surface can terminated in one of three different manners, each representing a distinct surface chemistry. The

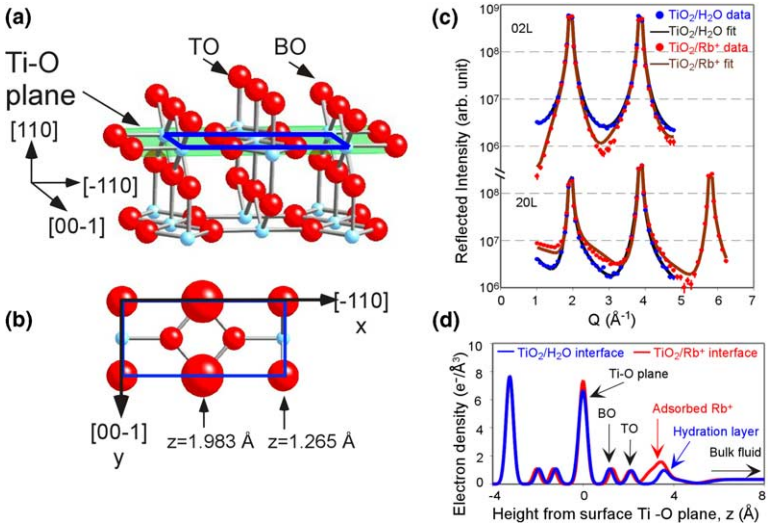

Fig. 9. (a) Perspective view and (b) top view of the rutile (1 1 0) surface, showing the bridging oxygen (BO) and terminal oxygen (TO) rows. (c) Selected non-specular CTRs of the rutile (1 1 0)–water interface (blue) and upon adsorption of Rb^+ (red). (d) Derived resolution-broadened lateral density profiles corresponding to the best-fit models. Figures reprinted in part with permission from Z. Zhang, P. Fenter, L. Cheng, N.C. Sturchio, M.J. Bedzyk, M. Predota, A. Bandura, J.D. Kubicki, S.N. Lvov, P.T. Cummings, A.A. Chialvo, M.K. Ridley, P. Benezeth, L. Anovitz, D.A. Palmer, M.L. Machesky, D.J. Wesolowski, Langmuir 20 (2004) 4954–4969. Copyright 2004 by the American Chemical Society. (For interpretation of the references in color in this figure legend, the reader is referred to the web version of this article.)

Ti–O plane of rutile contains two inequivalent Ti atoms and two co-planar oxygen atoms. Above this plane are two distinct oxygen layers that each form rows along [0 0 1]. The first layer consists of doubly coordinated BOs at a nominal height of 1.265 Å above the Ti–O plane. The second oxygen is a singly-coordinated terminal oxygen (TO) bound to a single Ti atom at a nominal height of 1.983 Å. (TO and NBO are interchangeable and the use of TO as the designation for the singly-coordinated oxygen species follows designation in [223].) CTR measurements in UHV [129] determined that the surface was terminated by the Ti–O plane with the BO, leaving behind a bare 5-fold coordinated Ti atom. This termination can be rationalized as the charge-neutral surface that would result upon cleavage of one Ti–TO bond per surface unit mesh. Not surprisingly, this surface also exhibited large structural displacements in the near-surface region that can be associated with the disruption of the local coordination environment of this surface Ti atom.

Specular and non-specular CTR measurements (Fig. 9c) show nearly ideal CTR profiles, indicating that the rutile (1 1 0)–water interface is only modestly modified with respect to an ideally-terminated lattice [223]. Structure factor fits to these data give the laterally averaged electron density profile (Fig. 9d). This profile reveals that the surface is terminated by (1) both a BO and TO whose locations are near the expected heights, (2) an additional discrete layer at a height of ~3.8 Å above the Ti–O plane, and (3) a featureless (error function) profile at a height of 5.6 Å corresponding

to the fluid water. The layer at ~3.8 Å is interesting because it occurs above the BO and TO layers that complete the coordination shell of the surface metal atoms and is ordered both vertically and laterally.

These data do not uniquely determine the full coordinates of this hydration layer, because the data used to derive the structure consisted of CTRs with surface Miller indices (H, K) having $H + K$ = even, but did not include the $H + K$ = odd rods (e.g., (1,0)) [223]. These latter rods are the "oxygen-only rods" because the scattering amplitude of the two Ti atoms in the bulk lattice exactly cancel for these rods. (Note that surface Ti atoms contribute to these rods if they are displaced from the ideal bulk truncated lattice positions.) The absence of such rods in the data means that the derived lateral locations are degenerate to displacements of $\boldsymbol{a}/2 + \boldsymbol{b}/2$. Analysis of the structure including these oxygen-only rods is being performed [224]. With this degeneracy in mind, plus the fact that the missing amplitudes from the oxygen-only rods are sensitive to details of the surface structure, the hydration layer positions derived from these data must be considered preliminary. Three different adsorption sites were found for water in the hydration layer. One (O1) is bridging between TOs with a lateral displacement of 1.04 Å at a height of 3.51 Å, and an occupation of 0.68 ± 0.1. A second (O2) is bound to a BO at a height of 4.05 ± 0.1 Å with a significant lateral displacement of 1.1 ± 0.1 Å and an occupation of 0.92 ± 0.2. A third (O3) hydration water was also found bridging between BO sites at a height of 3.66 ± 0.07 Å but with a substantially smaller occupation of 0.34 ± 0.06. Although these reported sites are each degenerate with a different site, they were chosen because they retain reasonable O–O distances and coordination suggestive of hydrogen bonds with the BO and TO sites. For instance, O1 has a distance to the TO of 2.3 Å, while O2 has nearly equal distances to the BO and TO of ~3 Å, and the O3 has a distance to the BO of 2.9 Å. Together these three sites provide a net coverage of 1.94 water molecules per unit mesh, in agreement with the expected water monolayer with a two-dimensional density of $0.1 H_2O/Å^2$.

Structural displacements were also determined at the rutile (1 1 0) surface. The BO and TO oxygens were found at heights of 1.17 ± 0.04 Å and 2.13 ± 0.03 Å, similar to, but distinct from, the expected heights of 1.27 Å and 1.98 Å, respectively [223]. The two Ti atoms in the surface plane were displaced vertically by 0.07 ± 0.01 Å and −0.13 ± 0.01 Å, but the actual direction of each is not determined by the degeneracy described above for the surface hydration layer. The oxygen in the Ti–O plane was displaced by only 0.02 ± 0.01 Å vertically and 0.02 ± 0.05 Å laterally along [−1 1 0].

Comparing these results to earlier CTR measurements for the rutile (1 1 0)–vacuum interface [129], we see that in addition to the expected absence of the TO and surface hydration layer under UHV conditions, the major difference between the rutile (1 1 0) surface in vacuum vs. water is that the structural relaxations are substantially reduced in the presence of water. For instance, the BO at the vacuum-terminated surface was displaced by −0.27 ± 0.08 Å, and the Ti atoms were displaced by 0.12 ± 0.05 Å and −0.16 ± 0.05 Å below the TO and BO rows, respectively. The substantially smaller structural relaxations for the rutile surface in water indicate that the coordination environment of the surface Ti atoms is only modestly perturbed with respect to the bulk structure, as compared with the surface in vacuum

where one Ti atom per unit mesh is 5-fold coordinated by oxygen instead of the 6-fold coordination found in the bulk crystal.

These results can be compared to computational studies of the rutile–water interface. For this surface, the role of surface charge must be discussed explicitly because the charge of the rutile surface depends on the solution pH through protonation/deprotonation reactions of surface functional groups (that is, the surface is amphoteric). A neutral rutile (1 1 0) surface results from cleavage of the crystal in which each of the daughter surfaces retains BOs but looses TOs, equivalent to the structure found in UHV [129]. Yet, as observed above, the actual rutile surface structure in water includes the TO rows. If these TOs result from the adsorption of water molecules, two protons should adsorb with each oxygen, forming a TOH_2 species that retains a net neutral surface. Surface complexation models have been used to gain insight into the surface charging of rutile through comparison with rutile powder titration data, but the results are not definitive in terms of the exact nature of the charging. In some cases the proton uptake of rutile is modeled in terms of a 1-pK model with a single reactive site, while in other cases two reactive sites are used.

There has been extensive effort to understand water interaction with titania, and the rutile (1 1 0) surface in particular [130–132,223,225–230]. There has been substantial disagreement concerning the nature of the initial adsorption mechanism, with conflicting results concerning whether the initial adsorption mechanism is associative or dissociative (i.e., adsorbing as intact or dissociated water molecules, respectively). While theoretical studies see dissociative water adsorption even at defect-free surfaces, experimental studies see dissociative water adsorption only with surfaces containing defect sites (see the recent reviews on this subject and references therein for a much more complete discussion [119,127]). Since these X-ray measurements were performed in contact with bulk water, the primary issue is not the initial water adsorption mechanism, but instead the interaction of water with a fully hydroxylated surface. Recent DFT calculations were performed in which two surface unit meshes were included and terminated by complete BO and TO rows, consistent with the CTR results described above. In this study, the water structure was probed as additional water molecules were added, with coverages up to two water molecules per surface unit mesh in addition to the BO and TO [130,131]. Charge neutrality was maintained by multiple surface sites, including an unprotonated BO, a protonated BO, a protonated TO, and a doubly protonated TO (i.e., a non-dissociated water molecule in the TO site). Adsorption of one water molecule per unit mesh (corresponding to $\sim$1/2 of a dense water layer) to a surface having complete BO and TO layers resulted in preferential coordination with the BO. Addition of a second water molecule per unit mesh (resulting in a nominally dense water monolayer) led to coordination of the water with the TO site, but tilted toward the BO site.

A second approach to understanding the structure of interfacial water at the rutile–water interface used large-scale MD simulations containing 2000 water molecules sandwiched between rutile (1 1 0) surfaces [223,226,227]. A key feature of this study was the use of DFT calculations to determine water–rutile interaction potentials [228,231] which were then incorporated into the MD simulations. Interaction potentials for liquid water were derived from the extended simple point charge

(SPC/E) model [232,233], which accurately reproduces the physical and structural properties of real water over a broad range of conditions. Thus, the conceptual simplicity of this model enables observation of the properties of the actual system that was probed with X-ray scattering. A significant challenge in this work was an inability to incorporate protonation reactions directly due to the use of the SPC/E model. The proton distribution of the surface therefore had to be assumed and its effect on the interfacial water structure (and ion adsorption) was evaluated separately to determine the likely proton distribution. Two choices for the surface protonation were made: (1) a non-hydroxlyated model in which the surface is terminated by non-protonated BO sites and water molecules in the TO site (corresponding to the associated adsorption models from UHV studies), and (2) a hydroxylated surface model, in which the surface is terminated uniformly by singly protonated BO and TO sites. In both cases, the MD simulations confirmed the major observations derived from CTR measurements that BO and TO sites are fully occupied, an additional surface hydration layer occurs at ~3.8 Å above the Ti–O plane, and ordering of water beyond the hydration layer (either laterally or vertically) is negligible. Comparison of interfacial water structure and adsorbed ion locations (measured with CTR and X-ray standing wave (XSW) techniques), indicated that the hydroxylated surface provides an excellent description of all relevant X-ray data [223]. In particular, the TO heights were predicted by MD to be 2.0 Å and 2.2 Å for the TOH and TOH_2 sites, respectively, while the experimentally measured value was 2.13 ± 0.03 Å. The surface hydration layer was observed from MD simulations to consist of two discrete lateral sites: one bridging the TOH and BO sites and the other bridging BO sites, with an average height of 3.8 Å, in good agreement with the CTR results.

2.1.3. Ruthenium dioxide (110) and (100)

Ruthenium dioxide (RuO_2) has significant similarities and differences with respect to rutile. RuO_2 has the same lattice structure as rutile, with slightly different lattice spacings. The (1 1 0) surface unit cell has surface dimensions of $|\boldsymbol{a}_1| = 6.36$ Å along [−1 1 0] and $|\boldsymbol{a}_2| = 3.11$ Å along [0 0 1], with a vertical separation between equivalent layers of 3.18 Å. This structure has a surface unit mesh area (19.78 $Å^2$) (Fig. 9a and b) that differs from the area of the rutile surface by only 3%. As for rutile, one can expect the surface of RuO_2 to consist of a mixed Ru–O plane, upon which may be added oxygen rows that consist of BOs or TOs, each completing the coordination shell of the two different Ru atoms within the Ru–O plane (Fig. 10a). The structural similarity of RuO_2 and rutile belies an important difference, in that RuO_2 is electrically conductive due to the partially filled d-shells of the ruthenium atom, unlike rutile (and most other minerals) that are either insulators or large band gap semiconductors. This difference in conductivity allows the RuO_2 surfaces to be studied under potentiometric control, as has been done for many metal surfaces. This opens up the additional thermodynamic variable of the electrochemical potential [114–118], which is unavailable to other mineral surfaces that can only be controlled through changes in pH, solution composition, and (to a limited extent) temperature. Consequently, in addition to applications that RuO_2 has in common with rutile

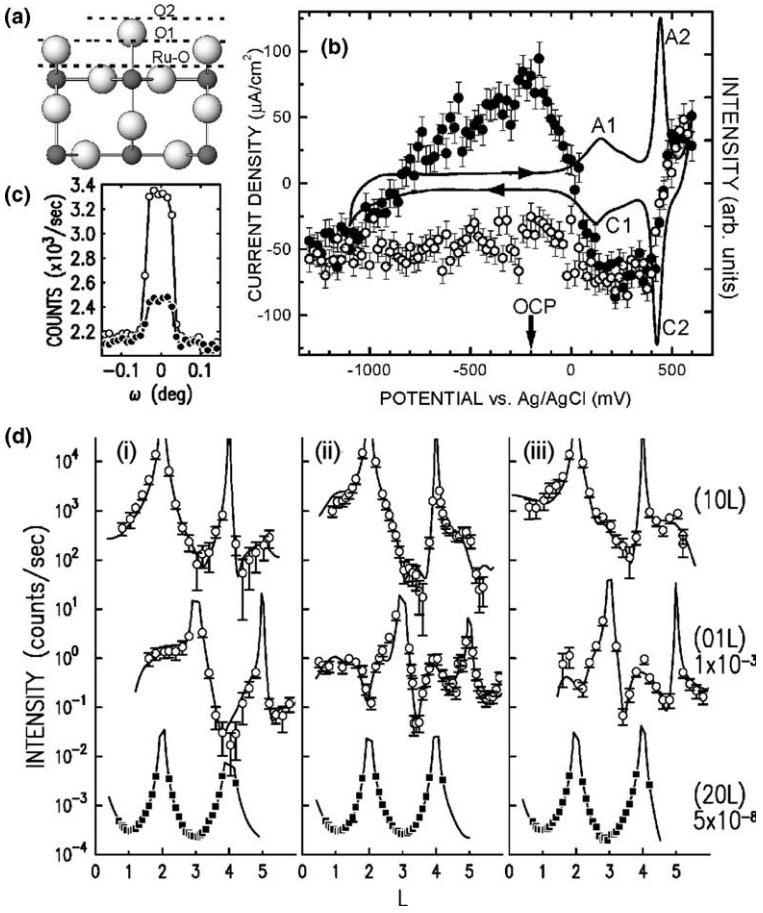

Fig. 10. (a) Side view of the $RuO_2(1\,1\,0)$ surface, showing the three possible terminations. (b) Cyclic voltammogram showing the variation of the current (lines) and X-ray scattering intensity (circles) as a function of electrochemical potential in 0.1 M NaOH. Solid and open circles are X-ray intensities measured at (0 1 4) during cathodic and anodic scans, respectively. (c) Rocking scans at (0 1 4) measured at −200 mV and 330 mV showing differences in the raw data X-ray scattering data indicated in (b). (d) Non-specular CTRs for the $RuO_2(1\,1\,0)$ surface at (i) 300 mV, (ii) 550 mV and (iii) −200 mV, each showing the (1,0), (0,1) and (2,0) CTRs. Note the significant differences in the shape of the CTRs between the Bragg peaks for the different potentials. (e) Derived structural schematics of the $RuO_2(1\,1\,0)$ surface at the potentials corresponding to the data in (d). Figures reprinted with permission from Y.S. Chu, T.E. Lister, W.G. Cullen, H. You, Z. Nagy, Physical Review Letters 86 (2001) 3364–3367. Copyright 2001 by the American Physical Society.

(such as catalysis), its conductivity has also led to applications as an electrode in energy storage and energy conversion.

Cyclic voltammograms of the $RuO_2(1\,1\,0)$ surface (Fig. 10b) in 0.1 M NaOH show two distinct reversible reactions at potentials near 150 mV and 400 mV, as compared with the open circuit potential of approximately −200 mV [93]. X-ray reflectivity data

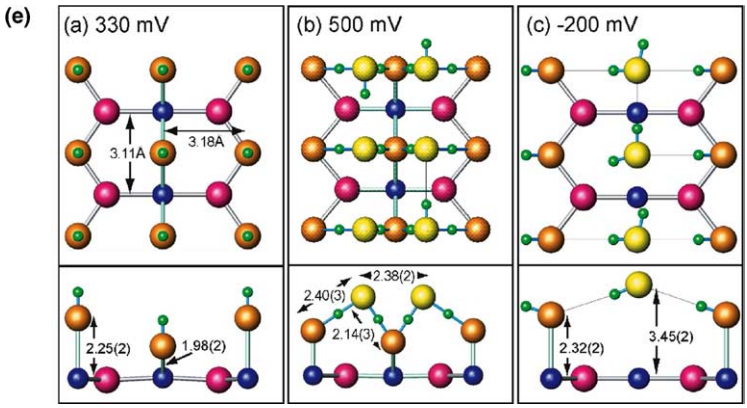

Fig. 10 (*continued*)

as a function of potential for a fixed scattering condition demonstrate that these reactions are associated with changes of the surface structure. In particular, the X-ray reflectivity data show substantial changes with no apparent hysteresis for the reaction near 400 mV, whereas the reaction near 150 mV is associated with substantial hysteresis below this reaction potential. With these results as a guide, full CTR measurements were performed at three potentials characteristic of each regime: 330 mV, 500 mV, and −200 mV (Fig. 10c). As for rutile, a subset of the CTRs (having surface Miller indices of $H + K$ = odd number; e.g., the $(1,0)$ and $(0,1)$ rods in Fig. 10) can be classified as oxygen-only rods because the scattering from the two Ru atoms in the bulk unit cell exactly cancels for these scattering conditions due to destructive interference. The other rods having contributions from both Ru and O are referred to as Ru rods (e.g., the $(2,0)$ rod in Fig. 10). The data show negligible changes in the Ru rods, indicating that the changes in the surface termination do not involve substantial changes in surface relaxations or morphology. Substantial changes observed in the oxygen-only rods indicate that the RuO_2 termination, and especially the distribution of surface oxygen atoms, changed during these electrochemical reactions. This can be seen most clearly in the $(0,1,L)$ rod where a typical "U"-shaped CTR at 330 mV between the Bragg peaks at $L = 3$ and 5 (i.e., with a local minimum in the intensity near $L = 4$), is transformed into a "W"-shaped CTR at both 500 mV and −200 mV (i.e., with a local maximum in the intensity near $L = 4$).

Analysis of these data led to the structural models shown in Fig. 10e [93]. These results show that the RuO_2 surface at a potential of 330 mV has a structure that might naively be expected for a hydrated mineral surface, with completion of the surface metal cations through adsorption of BO and TO species, assumed here to be OH^-, and with no additional adsorbed water layers. Since only non-specular reflectivity data were included in this analysis, layers that are vertically ordered but not laterally ordered would not have been observed. Consequently, the data are not sensitive to the presence of fluid water above the $RuO_2(1\,1\,0)$ surface. At the more positive potential of 500 mV, a similar structure is found with an additional adsorbed

layer that bridges between the BO and TO sites. This layer was interpreted as being an adsorbed water molecule whose coverage was found to be 2 molecules per unit mesh resulting in a 2D density that is similar to that observed in other systems including rutile (1 water/9.9 $Å^2$). This adsorbed species, however, had O–O separations to the TO and BO (2.4 Å and 2.14 Å, respectively) that were substantially smaller than expected for a typical hydrogen-bonded geometry (e.g., as that found in hexagonal ice of ~2.75 Å). Such spacings would be indicative of a symmetric O–H–O bond of the type found in high-pressure phases of ice such as ice X. At the same time the Ru–O bond lengths of the surface oxygens were also substantially changed with an expansion of 0.11 Å, and a contraction of 0.42 Å for the bond lengths to the BO and TO respectively.

A more extreme surface restructuring was found at the open circuit potential of −200 mV [93]. Here the two bonds between each BO and the Ru atoms in the Ru–O plane are disrupted resulting in a commensurate water monolayer that appears to interact through hydrogen bonds with the TO species. This structure is roughly similar to the associative adsorption of water at the rutile (1 1 0) surface observed in MD simulations and theoretical calculations [130,131,226,227] but it differs from those structures in that the bonds between the BO species and the surface are disrupted on RuO_2(1 1 0). In contrast, associative adsorption on rutile (1 1 0) leads to non-bonded water molecules in the TO site [226,227]. Substantial hysteresis was associated with X-ray scattering intensities below potentials of 200 mV, and attributed to differences in the ability of the water monolayer to order at negative potentials. X-ray scattering intensities as a function of applied potential indicate that the transformation of the BO to an adsorbed but non-bonded water species is continuous, with the oxygen atom height increasing continuously with decreasing potential. At sufficiently negative potentials (~−1000 mV) the water monolayer is completely desorbed. The monolayer does not readsorb, however, until increasing the potential to ~150 mV. At this potential the BO directly coordinates with the RuO_2 surface. The inability of the associatively ordered water monolayer to reform at potentials less than ~150 mV suggests a kinetic barrier.

Similar measurements were performed for RuO_2(1 0 0) and (1 1 0) surfaces in 0.5 M H_2SO_4 revealed different electrochemical and structural behavior [234,235]. Unlike the RuO_2(1 1 0) surface in alkaline environments where sensitivity to electrochemical reactions was found in the oxygen-only rods, the changes in the X-ray reflectivity data in acidic environments were primarily found in the Ru rods for both the (1 0 0) and (1 1 0) surfaces, suggesting more extensive restructuring of the surface. This restructuring consisted primarily of a lattice distortion along [−1 1 0] for both surfaces that is associated with a change in oxidation state of the surface from Ru^{4+} to Ru^{3+}. Associated with this restructuring was the inferred adsorption of H_3O^+ that was otherwise invisible to the X-ray data, presumably because of weak interactions with the surface oxygens. Measurements to isolate the structural changes associated with cathodic activation revealed that little or no structural change was associated with activation, except for an increase in surface roughness at extremely negative potentials [235].

2.2. Carbonates: calcite (104)

Calcium carbonate is interesting due to: the relatively rapid dissolution and precipitation kinetics [27]; the sensitivity of calcite solubility to atmospheric CO_2 concentrations and solution pH [46]; and the ability to incorporate trace quantities of various impurities [29–31,236–240]. These properties also make calcite and its polymorphs (including aragonite and vaterite) important biominerals as major constituents of exoskeletons [9,27]. The structure and reactivity of calcite surfaces have been extensively studied by various theoretical and experimental techniques. Most studies have considered the calcite $(10\bar{1}4)$ surface [hereafter referred to as the (104) surface], which is the dominant face exposed in calcite powders and is the perfect cleavage plane of calcite single crystals. These studies include surface complexation models for calcite–solute interactions [241,242], ab initio calculations and MD simulations [243–248], and atomic force microscopy (AFM) [249–253].

High-quality calcite (104) surfaces prepared by cleavage have large flat terraces separated by steps; the same surface is expressed by calcite powders. The expected termination of the calcite lattice consists of a surface unit mesh having lattice spacing of $|\boldsymbol{a}_1| = 8.097$ Å, $|\boldsymbol{a}_2| = 4.991$, a layer spacing of 3.035 Å, and an area of 40.41 Å^2, with an array of co-planar Ca^{2+} and CO_3^{2-} groups (Fig. 11a), roughly analogous to the NaCl (001) surface. The carbonate groups in the bulk truncated structure are tilted at 45.3° with respect to the surface-normal direction (Fig. 11b) so that the three carbonate oxygens are found at heights of +0.79 Å, 0 Å and −0.79 Å with respect to the surface Ca^{2+} ion in the bulk truncated lattice. Alternating CO_3^{2-} groups are related by glide plane symmetry along $\boldsymbol{a}_1$. The calcite (104) cleavage surface is created by breaking one Ca–O bond for each Ca^{2+} and CO_3^{2-} ion in the surface layer (a total of four broken bonds per unit mesh). This results in a nominal 5-fold coordinated Ca^{2+} ion at the surface, as compared with the 6-fold coordination in the bulk calcite. In the absence of any interaction with water, the surface would be terminated with one bare Ca^{2+} and a NBO of the CO_3^{2-} group protruding 0.79 Å above the surface plane.

Early X-ray reflectivity studies demonstrated that calcite surfaces were smooth and reproducible [220,254], consistent with AFM studies [249–253], and provided the first direct experimental observations of mineral–water hydration structures at isolated interfaces [220,254,255]. High-resolution specular CTR data of the calcite–water interface (Fig. 11c) display the expected variation of the CTR, albeit with a small but significant modulation associated with the internal structure of the calcite unit cell (most notably the carbonate oxygen layers at ±0.79 Å with respect to the Ca^{2+} planes) and any surface structural displacements and interfacial water structure [255]. The simplest model consistent with the data was one in which the outermost two calcite layers were relaxed and an adsorbed layer distinct from the fluid water structure was present at the calcite–water interface. Such a layer was unexpected if the calcite (104)–water interface consisted simply of bulk-truncated calcite (104) with featureless bulk water. The 2D density of these molecules was, within experimental error, equal to that of the Ca^{2+} ion if this molecule was reasonably identified as a water molecule. Separate measurements of the structure at calcite saturation

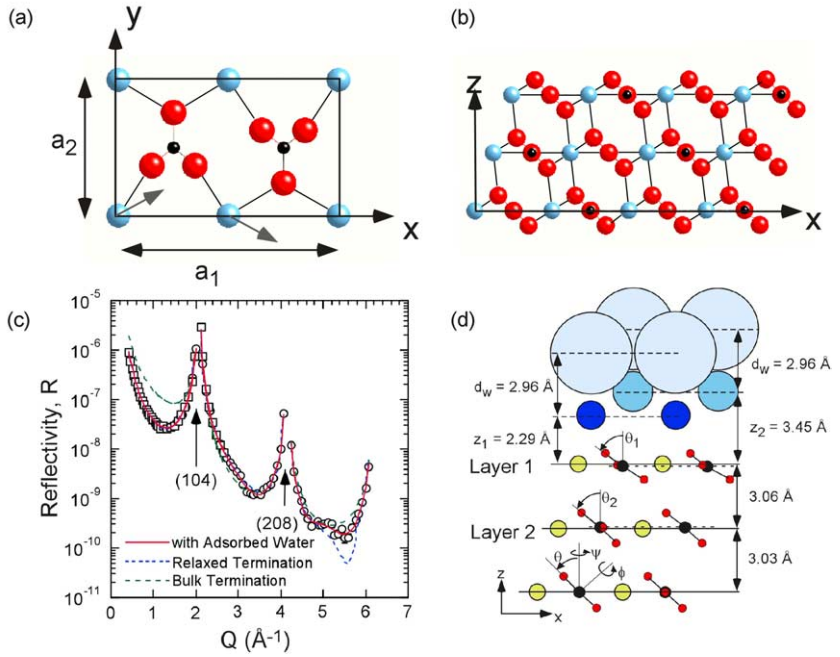

Fig. 11. (a) Lateral and (b) vertical structure of the calcite (1 0 4) surface (calcium: blue; oxygen: red; carbon: black). (c) Specular X-ray reflectivity data are shown. (d) Structural model of the calcite–water interface derived from specular and non-specular reflectivity data. Panel (c) is reproduced from P. Fenter, P. Geissbuhler, E. DiMasi, G. Srajer, L.B. Sorensen, N.C. Sturchio, Geochimica et Cosmochimica Acta 64 (2000) 1221–1228. Panels (a), (b) and (d) are reproduced from P. Geissbühler, P. Fenter, E. DiMasi, G. Srajer, L.B. Sorensen, N.C. Sturchio, Surface Science 573 (2004) 191–203, with permission from Elsevier. (For interpretation of the references in color in this figure legend, the reader is referred to the web version of this article.)

under both acidic and alkaline pH conditions showed no changes in the scattering intensities, indicating that Ca^{2+} and/or CO_3^{2-} ions do not adsorb to the calcite surface terraces.

The height of these adsorbed water molecules was found to be 2.50 ± 0.12 Å with respect to the surface Ca layer [255]. This is consistent with an adsorbed layer consisting of a water molecule with a Ca–O_w bond if that bond were directed largely along the surface-normal direction since the expected Ca–O bond length is 2.4 Å [255]. This can be ascribed to the need to saturate the Ca–O broken bonds. The derived structure reveals negligible "layering" of water beyond this first adsorbed water layer, and it was well-fitted by an error function profile to simulate a featureless water profile. More sophisticated models that include layering of the fluid water beyond the adsorbed water layer were tested, but no further structuring of the interfacial water was dictated by the data.

This simple picture has two serious shortcomings. First, the lateral location of the adsorbed water was not measured, and consequently the consistency of these results

was not uniquely established. Second, the adsorption of a single monolayer of water leaves an equal unoccupied volume within this first adsorbed water layer. The results are thus unsatisfying in that this model fails to satisfy a reasonable space-filling criterion.

Geissbühler et al. recently extended the analysis of the calcite–water interface to include both specular and non-specular reflectivity data [256]. Such data provide direct insight into the lateral interfacial structure. This data set is complete to a lateral resolution of ~1.2–2 Å laterally and ~0.7 Å vertically. These data resolve most of the shortcomings of the specular reflectivity study leading to the model in Fig. 11d. They demonstrate that the adsorbed water layer is laterally ordered, as expected based on chemical arguments, and is found at a height of 2.3 ± 0.1 Å. A second adsorbed water molecule, O_{w2}, is found 3.45 ± 0.2 Å above the surface plane but is located laterally between the O_{w1} molecules and has a larger rms vibrational amplitude. This combination of larger height and rms width suggests that this second water molecule is weakly adsorbed and fills the space between chemically adsorbed O_{w1} molecules. Although the O_{w1} molecule was found to be laterally ordered, a surprising aspect of this result was that this water molecule was laterally displaced away from the location expected if it acts simply to complete the Ca^{2+} ion coordination shell as determined by the calcite lattice (i.e., the lower oxygen of the "next layer" carbonate removed to create the surface). Instead, it was laterally displaced by ~2 Å from the Ca site in the opposite direction. This results in a calcium-water distance of 2.96 ± 0.12 Å that is substantially longer than the expected value of 2.4 Å.

Calcite surface relaxations were also probed, revealing that the surface Ca^{2+} and CO_3^{2-} ions are vertically displaced by -0.02 ± 0.02 Å and -0.124 ± 0.01 Å, respectively [256]. The tilt of the outermost carbonate increased by $11.3 \pm 0.5°$ with respect to its 45.3° tilt in the bulk structure (i.e., it tilted towards the surface plane). Displacements in the second layer were substantially smaller indicating that only the top surface layer is significantly perturbed from its bulk coordination geometry.

Computational studies of the calcite–water interface have focused primarily on MD simulations of calcite surfaces hydrated by the adsorption of a single monolayer of water to the calcite surface [244,245,248], with one water molecule per surface Ca^{2+} ion. These studies all revealed a calcite surface with relatively small structural relaxations and a tilt of the surface CO_3 that reduced the surface corrugation. The height of the adsorbed water monolayer was found at ~2.4 Å above the calcite surface, but results on the orientation of the protons attached to the adsorbed water molecule varied.

These simulations with a single adsorbed water molecule per Ca^{2+} ion provide direct insight into the role of water in stabilizing the calcite surface structure. Wright et al. showed that the calcite surface exhibits large structural displacements (e.g., −0.8 Å inward displacement of the surface Ca) without adsorbed water, and that these displacements are substantially reduced with water adsorption [244]. This directly indicates that water plays a key role in the properties of the mineral–water interface by chemically passivating the calcite surface. Such large structural displacements for dry vs. wet calcite surfaces have yet to be directly observed experimentally. These simulation results are qualitatively consistent with the calcite–water CTR

results, but they may not be directly comparable in detail, because they include only a single monolayer of water (whose density is ~1/2 of a dense water layer) as opposed to a semi-infinite water layer.

Recent MD simulations included a ~30-Å-thick water layer separating equivalent calcite surfaces [246,247] are therefore most comparable to the present X-ray results. These studies show a surface hydration layer consisting of two different water molecules, at heights of 2.2 Å and 3.2 Å above the surface Ca^{2+} ions, with significant modulation of the water density profile to ~10 Å above the calcite surface. These MD results are generally in close agreement with the heights derived from the X-ray data described above for the immediate hydration layer above the calcite surface, but some discrepancy remains concerning the lateral location of the adsorbed water molecules. For instance, the lateral position of the lower hydration layer is displaced in MD simulations by ~1 Å from the Ca site, resulting in a net Ca–O distance of 2.43 Å, while X-ray results find a lateral displacement of ~2 Å. The experimentally-derived Ca–O bond length could be the result of a distortion of the surface Ca^{2+} coordination shell (e.g., due to contraction of the in-plane Ca–O bond lengths and associated expansion of the bond length between the surface Ca^{2+} and the adsorbed water molecule). Bond lengths derived from these particular X-ray data, however, should be treated with some caution as they might be susceptible to systematic errors associated with an observed variability in the raw data in excess of the expected statistical error.

The Kerisit and Parker results revealed the nature of the adsorbed water molecules through the use of density functional theory (DFT) calculations [246]. Although X-ray results are insensitive to the nature of this species [e.g., hydroxyl (OH^-), water (H_2O), or hydronium (H_3O^+)], previous Fourier transform infrared spectroscopy (FT-IR) and X-ray photoelectron spectroscopy (XPS) studies of calcite surfaces showed evidence for the adsorption of hydroxyls at the calcite surface [257–259]. Energy minimization calculations for calcite surfaces that were initially terminated by a single monolayer of either water or hydroxyl ions (OH^-), showed that molecularly adsorbed water is favored energetically over hydroxyl ions on the calcite (1 0 4) surfaces and that the adsorption of hydroxyl ions would take place only on some steps and low-index calcite surfaces. Consequently, the experimentally observed surface hydroxyl ions seen in XPS and FT-IR studies (under vacuum conditions) appear to be inconsistent with the computational studies of the calcite–water interface. This suggests, at a minimum, fundamental differences between the calcite–water and calcite–water vapor interfaces, or that these surface hydroxyl species are indicative of defect sites instead of idealized smooth terraces.

We finish the description of the calcite–water interface with a discussion of the calcite termination in the context of the bond valence model. Calcium has a net valence per bond of 2/6 = 1/3 v.u., while carbon has a valence of 4/3 v.u. per C–O bond. Oxygen atoms have a nominal valence of 4/3 for each C–O bond and 1/3 for each Ca–O bond. The broken bonds in the unit cell associated with the Ca^{2+} ion and the outermost oxygen in the CO_3^{2-} each have a nominal valence of 1/3. We expect the observed structure to compensate for the valence deficit for both the Ca^{2+} and CO_3^{2-} ions. These bond valence considerations show that Ca^{2+} is unlikely to com-

plete its coordination shell by adsorbing a hydroxyl ion because its available bond valence (~0.8 v.u.) is substantially larger than the bond valence deficit of the surface Ca^{2+} ion. Instead, molecular adsorption of water to the Ca^{2+} site through a donating hydrogen bond has a nominal bond valence of 0.2. Compensation for the remaining deficit of 0.13 v.u. can occur by strengthening of the other five Ca–O surface bonds which were not broken in cleaving the surface or the Ca–O_{w1} interaction. Similarly, the 1/3 v.u. deficit for the outermost oxygen in CO_3 is too small to be compensated for by direct adsorption of a proton, but it can be largely compensated for by an accepting hydrogen bond to a water molecule (e.g., through the hydrogen atom associated with O_{w2}). The height difference between the carbonate oxygen and O_{w2}, ~2.7 Å, is typical of the O–O separation of water molecules interacting through hydrogen bond and is consistent with this simple picture. Therefore, the adsorption of both O_{w1} and O_{w2} appears to be needed to properly terminate valence imbalance due to creation of the surface. The bond valence model provides a simple explanation for the molecular (i.e., non-dissociative) adsorption of water to the calcite surface that is directly associated with the magnitude of the surface bond valence deficit upon cleavage of the crystal. The generally excellent agreement between the experimental observations (by X-ray scattering), and the computational studies (DFT calculations and MD simulations) and bond valence model suggests that the bonding and interactions of this surface are generally well understood.

2.3. Sulfates: barite (001) and (210)

Barite ($BaSO_4$) is a molecular ionic crystal, like calcite. Barite is relatively insoluble in aqueous solutions and this is problematic in the oil production industry when Ba-rich oilfield brines encounter SO_4-rich seawater to cause unwanted barite precipitation. Hence considerable efforts have gone into developing surface-active growth inhibitors for barite. In addition, barite's insolubility makes it a good archive of the chemical and isotopic history of seawater [260].

Barite has lattice spacings, $a = 8.884$ Å, $b = 5.457$ Å, $c = 7.157$ Å, with space group Pbnm. This results in a screw axis along (001) and consequently Bragg peaks with $\boldsymbol{H} = (2n + 1)L$ (where n = integer) are missing. The (001) surface is a square lattice with $|\boldsymbol{a}_1| = 8.884$ and $|\boldsymbol{a}_2| = 5.457$ Å. Unlike calcite (104), the barite (001) surface can, in principle, be terminated in more than one manner. Fig. 12a is a side view of the barite surface. Each barite unit cell consists of two equivalent layers (separated by 3.58 Å) that are related by a screw axis along [001]. Within each of these layers, the barite lattice can be terminated by either a complete $BaSO_4$ bilayer or half-bilayer.

The data in Fig. 12b show a typical CTR profile, albeit with a substantial reduction in reflectivity near $L \sim 3$ [218]. This feature is associated with the termination of the lattice with a double $BaSO_4$ layer, as shown in Fig. 12c due to termination interference described in Section 1.5.2. This can be seen using the relations in Section 1.5.2, where an ideally-terminated surface with a complete $BaSO_4$ bilayer should exhibit a node in the substrate structure factor near $L = 3.3$, while a half-bilayer termination has a node near $L = 0.6$. The incorporation of a complete $BaSO_4$ layer plus structural relaxations and an adsorbed water layer was needed to achieve a

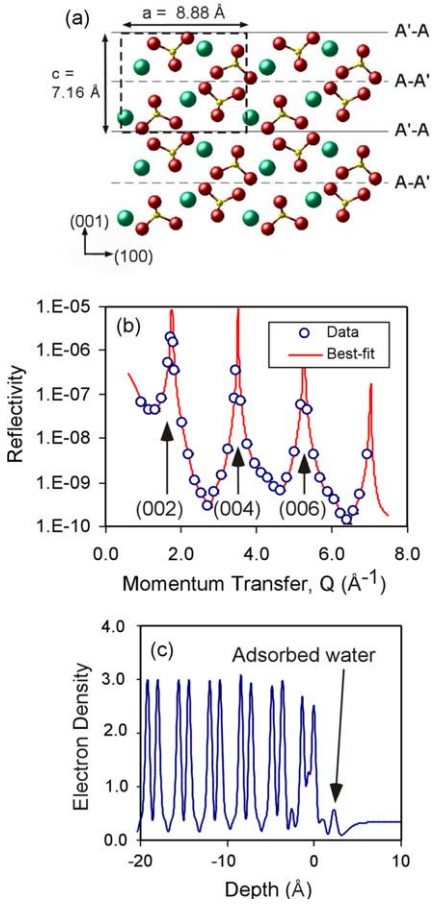

Fig. 12. (a) Schematic view of the barite (0 0 1) surface as seen from the side (barium: green; sulfur: yellow; oxygen: red). (b) Specular reflectivity data. (c) Derived resolution-broadened electron density profile. The adsorbed water feature is associated with the completion of the outermost Ba^{2+} ions coordination shells. Figures reprinted in part with permission from P. Fenter, M.T. McBride, G. Srajer, N.C. Sturchio, D. Bosbach, Structure of barite (0 0 1)- and (2 1 0)–water interfaces, Journal of Physical Chemistry B 105 (2001) 8112–8119. Copyright 2001 by the American Chemical Society. (For interpretation of the references in color in this figure legend, the reader is referred to the web version of this article.)

quantitative fit to the experimental data. The Ba^{2+} ions are displaced from their bulk lattice locations by ~0.07 Å near the surface. The outermost SO_4^{2-} ions show a larger displacement of ~0.4 Å and a rotation of 19° within the outermost $BaSO_4$ bilayer. The best-fit model includes an adsorbed water layer at a height of 2.35 ± 0.13 Å above the outermost Ba^{2+} ion, with 2.7 ± 0.1 water molecules per barite (0 0 1) surface unit mesh ($A_{uc} = 48.4$ Å^2). These measurements are insensitive to the presence of protons, and therefore the molecular species of the water (e.g., hydroxyl or hydronium) cannot be identified uniquely from these data; we refer to these simply as water molecules for convenience.

As in the calcite (1 0 4) specular reflectivity results, the measured water coverage is significantly smaller than that for a close-packed water layer ($\sim 1 H_2O/(10\ \text{Å}^2)$ surface area, or 4.8 water molecules per unit mesh), which would be expected if the barite surface acts a chemically inert hard wall [218]. Instead, we consider that four Ba–O bonds are broken at the (0 0 1) surface per unit mesh by cleavage (three to the outer Ba^{2+} ion, one to the inner). The expected oxygen heights of the lattice oxygens to complete the Ba^{2+} coordination shells are found at 2.4 Å, 2.4 Å, 1.9 Å, and 1.5 Å with respect to the upper Ba^{2+} ion, as derived from the unrelaxed bulk barite structure. The observed height for the adsorbed water layer is similar to the average nominal Ba–O height (2.2 Å) associated with the upper Ba^{2+} ion's three broken bonds, and the number of adsorbed water species is moderately consistent with this value as well (2.7 ± 0.1 vs. 3.0 oxygens). This result suggests that the adsorbed water molecules saturate the broken bonds of the surface Ba^{2+} ions, in analogy to the observations for Ca^{2+} ions at the calcite–water interface (Section 2.2). Similar results were found for the barite (2 1 0)–water interface [218] with respect to the adsorption of water molecules to the surface whose coverage and height are determined by completion of the Ba–O coordination shell, and with structural relaxations penetrating two molecular layers into the lattice.

No theoretical studies have been done for comparison with these results. Elementary bond valence arguments can be used to rationalize the chemical properties of the interface. The Ba^{2+} ion in barite has a nominal 12-fold oxygen coordination shell in the barite lattice, albeit with substantial variation in Ba–O bond lengths of 2.86 Å to 3.32 Å. An analysis of the bulk Ba–O bond lengths shows that each of the four broken bonds has a nominal valence of ~0.25 v.u. This value is small with respect to the valence of an O–H bond in water (~0.8), suggesting that the adsorption of water molecules will complete the Ba–O coordination shell. The same conclusion was reached for calcite (Section 2.2).

As in the case of calcite, where a complete understanding also incorporated the valence deficit of the surface CO_3^{2-} groups, we must consider the valence deficit of the SO_4^{2-} groups that matches that of the undercoordinated Ba^{2+} ions. The valence deficit for SO_4^{2-} appears as three Ba–O broken bonds for the outermost SO_4^{2-} group and one broken bond for the next SO_4^{2-}. Given the small valence deficit per bond (~0.25 v.u.), each of these undercoordinated oxygen atoms could be compensated for by accepting hydrogen bonds with adsorbed water molecules. The observation that the total number of adsorbed water molecules is equal to the number of Ba–O broken bonds could indicate that each water must interact with both the SO_4^{2-} oxygen and the Ba^{2+} ion. Given the variability of Ba^{2+} and oxygen locations at the surface, this possibility is unlikely as a general explanation, although it might occur for a subset of the bonds. Another possibility derives from the relatively large relaxations derived for the surface SO_4^{2-} (with a displacement of ~0.4 Å and rotations as large as 19°), as compared with the small displacements observed for Ba^{2+} (0.07 Å). This observation suggests that compensation for the surface sulfate valence by interaction with water is limited; instead the SO_4^{2-} structural relaxations appear to modify the individual Ba–O bond lengths so as to optimize accommodation of the SO_4^{2-} valence.

2.4. Phosphates

2.4.1. Potassium dihydrogen phosphate (101) and (100)

Potassium dihydrogen phosphate (KH_2PO_4, or KDP) is widely used as an optical element in laser systems. KDP crystals are grown from aqueous solutions and consequently the KDP–water interface has been studied intensively. This attention has led to tests of fundamental theories of crystal growth through direct observations of crystal growth with molecular-scale probes, such as AFM [261]. One fundamental aspect of crystal growth theories centers on understanding the crystal faces that are expressed (i.e., the growth habit) and the crystal termination (i.e., the surface structure) [262]. Experimental control over crystal morphology and habit are often desired. The incorporation of impurities is also an important aspect of crystal growth (i.e., as a growth modifier) [263]. Knowledge of the atomic-scale structure of the KDP–water interface is therefore necessary as a foundation for testing many of these theories.

The habit of KDP crystals grown in aqueous solution has the form of tetragonal prisms with four (1 0 0) prismatic faces doubly-terminated by four pyramidal (1 0 1) faces (Fig. 13a). Although only one surface termination for the prismatic (1 0 0) face is likely (since it consists of co-planar K^+ and PO_4^{3-} ions in each layer), the (1 0 1) surface can have various terminations that cannot be distinguished by theoretical arguments, as can be seen in a side view of the KDP (1 0 1) structure (Fig. 13b).

The KDP (1 0 1) surface mesh consists of surface lattice spacings $|\boldsymbol{a}_1| = |\boldsymbol{a}_2| = 6.316$ Å, with a layer spacing of 10.20 Å along the surface-normal direction. The surface unit mesh is oblique, with 107° angular separation between the surface unit axes, resulting in a quasi-hexagonal surface unit mesh with an area of 38 Å^2. Each KDP unit cell consists of an A–B stacking of two equivalent KDP layers with a vertical separation of 5.10 Å. Each KDP layer consists of two inequivalent KDP molecules in a nominal sequence of K-PO_4-PO_4-K along the surface-normal direction. Consequently, even if the crystal is assumed to have a stoichiometric composition up to the surface, the surface can be terminated by either a K^+ or PO_4^{3-} layer. AFM measurements observe elementary steps with measured heights in multiples of 5.10 Å [261]. This result suggests that only one of the two terminations is expressed at the surface, but AFM measurements do not distinguish between the two possible terminations.

Non-specular X-ray reflectivity measurements were measured for the (1,0), (1,1), and (2,1) CTRs [210] (a subset of these data are shown in Fig. 13c). The (2,0), (2,−1) and (0,1) rods were also reported separately. [210,264] The KDP lattice termination can be assessed directly by comparing the experimental data to structure factor calculations for ideally-terminated lattices. As a layered crystal structure, the reflectivity profiles for KDP (1 0 1) surface can be expected to exhibit substantial differences for the different terminations. The most notable of these is a sharp pseudo-node, L_o, found in calculations of the (10) rod near the bulk Bragg reflection near $L = 1$, where $L_o = 1 - \delta$ for the K^+ terminated lattice, and $L_o = 1 + \delta$ for the PO_4 terminated lattice with $\delta \sim 0.2$. These values are characteristic of termination interference and, although no true node is observed in the experimental data, a substantial intensity asymmetry above and below the (1 0 1) Bragg reflection suggests that the KDP

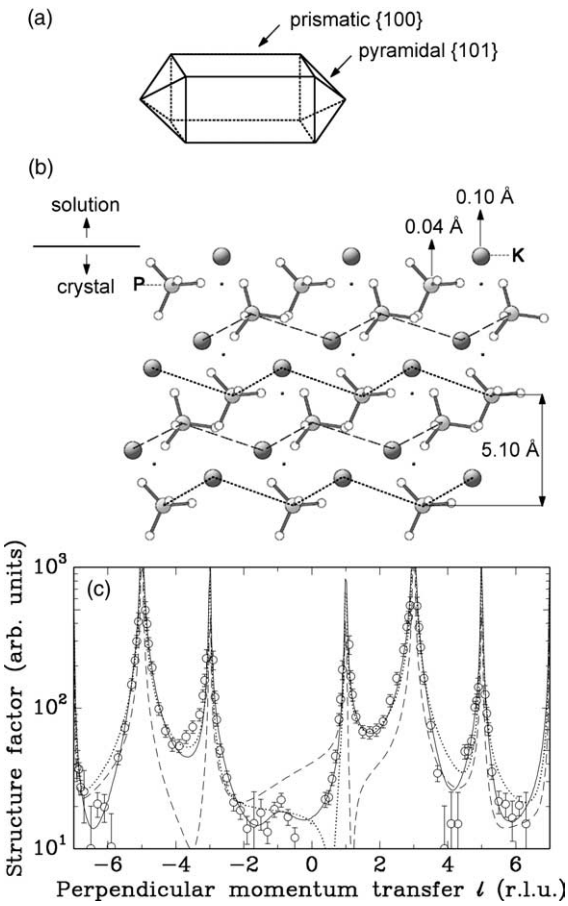

Fig. 13. (a) Growth form of KDP expressing prismatic (1 0 0) and pyramidal (1 0 1) surfaces. (b) Structural schematic of the KDP–water interface, with derived structural displacements shown. (c) CTR data for the KDP–water interface. Figures reprinted with permission from S.A. de Vries, P. Goedtkindt, S.L. Bennett, W.J. Huisman, M.J. Zwanenburg, D.M. Smilgies, J.J. De Yoreo, W.J.P. van Enckevort, P. Bennema, E. Vlieg, Physical Review Letters 80 (1998) 2229–2232. Copyright 1998 by the American Physical Society.

(1 0 1) surface is K^+-terminated. A fully optimized structural model providing a quantitative description of the experimental data indicated that the K^+ ions in the top layer relaxed outward by 0.10 ± 0.05 Å, while the PO_4^{3-} groups relaxed by 0.04 ± 0.05 Å.

Similar measurements were performed on the KDP (1 0 0) (prismatic) surface [210]. In that case the K^+ and PO_4^{3-} ions are co-planar and only one termination is expected. An optimized model of this surface is consistent with the experimental data and demonstrated that the substrate surface relaxations were <0.1 Å.

No discussion concerning the structure of water adjacent to the KDP surface was included for these measurements of the KDP–water interface. A more detailed

description of the structure of water adjacent to the KDP–water vapor interface is in Section 3.2.1.

2.4.2. Ammonium dihydrogen phosphate (101)

Measurements performed to determine the structure of ammonium dihydrogen phosphate ($NH_4H_2PO_4$, or ADP) (1 0 1) surface explored the role of the lattice cation in controlling the surface structure and termination [265]. ADP and KDP have similar crystal structures with K^+ replaced by the ammonium ion (NH_4^+). ADP and KDP grow with identical crystal morphologies, exposing the (1 0 0) prismatic and (1 0 1) pyramidal surfaces. A significant difference between these two lattices is the nature of interactions. ADP is known to have strong hydrogen bonds which might alter the character of the surface with respect to the KDP surface. The observation of elementary steps by AFM with a minimum step height of 5.3 Å suggests that the growth surface has a single crystallographic termination [265].

Comparison of the (1,0), (0,1), and (1,1) rods to structure factor calculations again showed substantial differences for NH_4^+ and PO_4^{3-} terminations, with the NH_4^+ terminated lattice showing better qualitative agreement with the experimental data [265]. A full optimization of the structural model allowing structural displacements in the top two layers confirmed this assignment and revealed surface lattice displacements with an inward relaxation of the surface NH_4^+ by -0.34 ± 0.13 Å and an outward relaxation of PO_4^{3-} by 0.27 ± 0.11 Å. No significant contributions were identified that indicated water structure at the ADP–water interface. This observation suggests that any water structure is limited to vertical ordering because these non-specular CTR data require lateral ordering to observe interfacial water structure.

The most striking aspect of these observations is that the displacements of K^+ at KDP (1 0 1) and NH_4^+ at ADP (1 0 1) are in opposite directions [265]. The difference in behavior of the surface relaxation is attributed to the absence of hydrogen bonds in the KDP structure. Creation of the ADP surface disrupts two hydrogen bonds per unit mesh, one for each of the NH_4^+ and PO_4^{3-} species. The substantial reduction of the vertical distance between the NH_4^+ and PO_4^{3-} layers compensated for the loss of hydrogen bonds by providing for additional interaction between the nitrogen atom in NH_4^+ and the oxygen atom in PO_4^{3-}.

2.4.3. Fluorapatite (100)

Apatite is an important biomineral as a major constituent of teeth and bone and is known for its extremely low solubility. Apatite minerals have variable anionic compositions including pure end members with fluoride (fluorapatite, FAp), hydroxyl (hydroxyapatite) and chloride (chlorapatite), as well as a high capacity to incorporate trace elements. The nominal FAp composition is $Ca_{10}(PO_4)_6F_2$. FAp is hexagonal having space group P63/m and lattice spacings $a = 9.37$ Å and $c = 6.88$ Å. The (1 0 0) growth surface of a natural gem-quality FAp from Cerro de Mercado, Durango, Mexico was studied (Fig. 14a). This surface has an orthogonal unit mesh with dimensions $|\boldsymbol{a}_1| = 9.37$ Å and $|\boldsymbol{a}_2| = 6.88$ Å, with a surface unit mesh area of

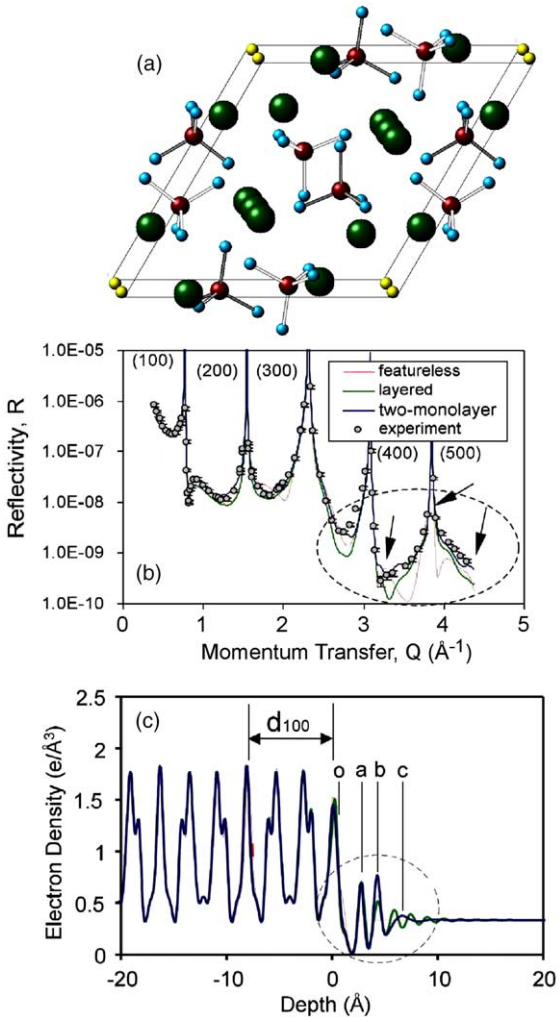

Fig. 14. (a) Structural schematic of the fluorapatite (100) surface in perspective view (calcium: green; fluorine: yellow; phosphor: red; oxygen: blue). (b) Specular CTR data for the fluorapatite-water interface with calculations corresponding to various models. (c) Derived resolution-broadened density profiles for the models calculations in (b). The blue line indicates the best-fit structure. Figures are reproduced with permission from C. Park, P. Fenter, Z. Zhang, L. Cheng, N.C. Sturchio, American Mineralogist 89 (2004) 1647–1654. (For interpretation of the references in color in this figure legend, the reader is referred to the web version of this article.)

64.5 Å^2. The sample was taken from a rock specimen containing individual crystals, ~2–3 mm wide and ~5–6 mm long in a rock matrix. The crystals were terminated by hexagonal prismatic (100) and hexagonal dipyramidal (101) faces.

As with any growth surface, an a priori determination of the terminating plane is non-trivial. For FAp, additional conceptual difficulties are derived from (1) the dual

ionic and covalent character of its bonds; (2) a multiplicity of lattice terminations. Three distinct terminations consist of a mixed Ca–PO_4 termination at the traditional unit cell border (as shown in Fig. 14a), a Ca-terminated lattice, and a PO_4 terminated lattice obtained by terminating the lattice half-way between the traditional unit cell boundaries; and (3) the possibility that the surface composition is not stoichiometric. In spite of these possible difficulties, the specular reflectivity showed a sharp dip in intensity just above the (1 0 0) Bragg peak (Fig. 14b) that is characteristic of the termination interference described in Section 1.5.2 [216]. Model calculations for various terminating planes (some showing a dip above or below the (1 0 0) Bragg peak, and others showing no such dip), indicated that the FAp lattice is terminated at the plane consisting of the traditional unit cell boundary shown in Fig. 14a.

Completion of the structural model to obtain quantitative agreement with the experimental data required the inclusion of changes in the surface stoichiometry, surface structural relaxations, and interfacial water structure [216] (Fig. 14c). The outermost surface layer was found to be deficient in Ca^{2+} and/or F^- ions (non-specular reflectivity would be needed to distinguish between these two sites), with a nominal composition of $\theta_{Ca} = 1.67 \pm 0.33$ with fixed $\theta_F = 1.0$ (with respect to the ideal occupation of 2 for Ca^{2+} and F^-). This surface Ca^{2+} deficiency suggests that the FAp had partially dissolved, either naturally or during preparation of the crystal for the X-ray measurements. Surface structural relaxations included small displacements of the surface Ca^{2+} ion (0.01 ± 0.14 Å) and relatively large displacements of the surface PO_4^{3-} (-0.34 ± 0.12 Å) and F^- ion (0.38 ± 0.37 Å).

Substantial structuring was observed above the mineral surface [216]. Although the composition of this layer is uncertain (due to its history as a natural growth surface and the potentially complex surface chemistry of apatite), it was analyzed in the context of an ordered hydration structure, with two distinct layers at heights of 2.64 ± 0.09 Å and 4.17 ± 0.14 Å and occupation factors of 3.5 ± 1.3 and 4.1 ± 2.2 water molecules per unit mesh. Again, as found in other systems described above, this occupation factor is substantially smaller than one would expect for a dense water layer, which would result in an occupation factor of ~6.5 per unit mesh.

In the context of the broken bonds associated with the creation of the FAp (1 0 0) surface, the completion of the oxygen coordination shell surrounding the two undercoordinated surface Ca^{2+} ions would result in three oxygen atoms at heights of 2.16, 2.16, and 2.693 Å, at an average height of 2.33 Å. This result is consistent in number and modestly consistent in height with the first hydration layer observed at a height of 2.64 Å. In the bond valence picture, this presumed hydration layer would probably consist of water molecules (as opposed to OH^-) since the Ca–O bond valence of $\sim 2/6 = 1/3$ v.u. is relatively small and similar to that found at the calcite–water interface.

More generally, this two-layer structure is difficult to understand in simple geometric terms because of the relatively low density of these layers. This observation suggests that an additional, potentially fluid or less ordered, component to the interfacial water structure was not observed much as the measurements of the calcite–water interface using specular reflectivity were insensitive to the more poorly ordered

interfacial water, resulting in a structure that suggested a low-density water layer. In this respect, it is interesting that the derived interfacial structure is consistent with the formation of a partial layer of octacalcium phosphate (OCP; $Ca_8H_2(PO_4)_6 \cdot 5H_2O$), a "hydrous defective apatite" [266,267] that has been proposed as a metastable precursor phase in the formation of thermodynamically stable hydroxyapatite (Hap) [267–269]. The replacement of Ca^{2+} in the OCP half unit cell with water and the removal of some PO_4^{3-} ions reproduce a structure similar to the layered water structure derived for the FAp (1 0 0) surface.

2.5. Silicates

2.5.1. Muscovite (0 0 1)

Muscovite is a widely studied mineral substrate. The muscovite crystal structure consists of silicate sheets separated by K^+ ions (Fig. 15a). Each silicate sheet consists of three distinct layers: a layer of octahedrally coordinated Al^{3+} cations sandwiched between two layers consisting of tetrahedrally-coordinated Si^{4+} and Al^{3+} cations. Muscovite is often studied as a model clay mineral because it can be obtained in large single crystals with atomically smooth basal planes. Muscovite is also used as the primary substrate for studies using the surface force apparatus, in which the forces between two cylindrically bent muscovite lattices are measured as a function of the separation of the two surfaces [69,70].

The relative ease with which muscovite (0 0 1) surfaces are cleaved is a result of the absence of covalent bonds between neighboring silicate sheets that are bound electrostatically. The resulting cleavage surfaces have an exceptionally low step density. The nominal muscovite (0 0 1) cleavage surface is composed of the basal planes of SiO_4 tetrahedra arranged in ditrigonal rings. The surface lattice is approximately hexagonal with lattice spacings of $|\boldsymbol{a}_1| = 5.189$ Å and $|\boldsymbol{a}_2| = 9.007$ Å for a rectangular surface unit mesh with area 46.7 Å^2. The muscovite sheets have an oblique A–B stacking with $|\boldsymbol{a}_3| = 20.048$ Å and $\beta = 95.779°$ resulting in a vertical separation of 9.97 Å between neighboring sheets. Cleavage can be expected to lead to the creation of two neutral surfaces, each with half of the K^+ ions to compensate for the fixed lattice charge due to isomorphic substitution of Al^{3+} for Si^{4+} in the tetrahedral layer. In contact with water under ambient conditions, the K^+ ions are expected to exchange for hydronium (H_3O^+) [270,271], making this surface effectively a hard wall (defined by the basal-plane O atoms) augmented with an array of ditrigonal cavities.

The specular X-ray reflectivity data of the muscovite (0 0 1)–water interface are shown in Fig. 15b with a calculation corresponding to the best-fit model of the interface structure [214]. The optimized structural parameters from the best-fit model show minimal surface structural relaxations that are significant primarily for atoms within the outermost polyhedral layer, with predominantly inward displacements as large as 0.04 ± 0.02 Å. The derived interfacial water structure (i.e., the water O density profile) (Fig. 15c) includes broadening due to the finite experimental resolution (~1.1 Å) [218]. Features that are resolved in this presentation are expected to be uniquely determined. The adsorbed layer was located at 1.3 ± 0.2 Å above the mean position of the relaxed surface oxygen, comparable to but smaller than the height

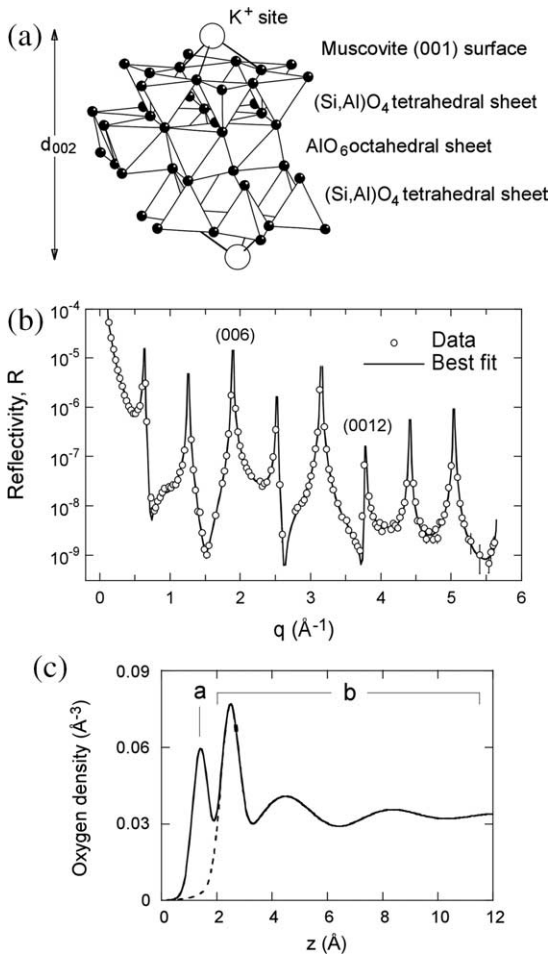

Fig. 15. (a) Schematic perspective view of the muscovite (001) surface showing the tetrahedral–octahedral–tetrahedra layer structure and a K^+ ion above the ditrigonal site. (b) Specular CTR data of the muscovite–water interface. (c) Derived resolution-broadened density profile of water above the muscovite–water interface. Figures reprinted with permission from L. Cheng, P. Fenter, K.L. Nagy, M.L. Schlegel, N.C. Sturchio, Physical Review Letters 87 (2001) 156103. Copyright 2001 by the American Physical Society.

of 1.6 Å for the unrelaxed K ion (Fig. 15c) and with a coverage of 1.0 ± 0.2 water molecules per unit mesh consistent with direct incorporation of water molecules (or H_3O^+) within each ditrigonal site. In this geometry, the O_{water}–$O_{silicate}$ distance of 2.6 Å is comparable to the O–O hydrogen bonding distance in water. Consequently this water molecule could have each of its two protons pointing toward two of the three silicate oxygens that extend into the ditrigonal site. The hydration structure beyond this first adsorbed layer has a narrow first layer and substantially damped oscillatory density profile for subsequent layers extending ~10 Å above the

surface with a period of 3.7 ± 0.3 Å. The first peak in the hydration layer has a lateral density equivalent to 1.3 ± 0.2 water molecules per ditrigonal ring and is located 2.5 ± 0.2 Å above the surface. This position compares well with the oxygen heights of ~2.6–2.8 Å for water molecules directly hydrating the (0 0 1) face of vermiculite, montmorillonite, and talc [57,78,79] and it is comparable to the O–O distance for a hydrogen bond.

Because these data derive from only the vertical structure, any interpretation of the lateral structure and order must be treated cautiously. For instance, the nominal correlation between the adsorbed water layer coverage and the ditrigonal site density suggests that this species is laterally ordered. Beyond this layer, the marginally larger lateral density of the first hydration layer (of 1.3 ± 0.2 water molecules per unit mesh at a height of 2.5 Å above the surface plane) suggests that this first hydration layer may not have a simple epitaxial arrangement.

The extended hydration structure observed for muscovite suggests the presence of a hydrogen bonding network near the interface. This interpretation was recently confirmed by MD simulations [222], with good agreement on the locations of the first two peaks in the water density profile and a weakly modulated water layer within ~10 Å of the muscovite surface. In particular, this simulation also shows that the second water layer has its hydrogen atom pointing toward the surface plane, directly indicating the formation of a hydrogen bond with the surface. This illustrates that combining X-ray based methods with computational results can be a powerful approach to extend the understanding of these complex systems to aspects of the structure that cannot be probed directly by experiments. However, this simulation was performed in a confined geometry in which the surface K^+ ions, while desorbed, remained closely associated from the surface (in contrast to the experimental conditions in which they were likely completely removed from the surface). Consequently, some of the agreement between the simulated and experimentally-derived water oxygen profiles may be fortuitous.

Both experimental and simulation results suggest that a hydrogen bonding network exists in the interfacial water at muscovite and that the ordering of the interfacial water is more extended than at any other mineral–water interface studied to date. In considering evidence that this hydration layer may be ice-like, as has been suggested in the case of thin water films adsorbed on muscovite surfaces [133,272], we might expect that any such ice-like layer would be lattice-matched to the muscovite lattice. The similarities between hexagonal ice (Fig. 3a), the most likely ice structure (found near 0 °C and 1 bar), and the muscovite lattice are interesting. The (0 0 1) ice structure has a ~14% lattice mismatch with respect to the muscovite basal plane, with hexagonal-equivalent lattice spacings for the two structures of 5.2 Å and 4.5 Å, respectively. These are relatively large differences for a true epitaxial relationship between an ice-like layer and muscovite. The layer spacing of hexagonal ice along [0 0 1] is 3.64 Å, within error of the layer distance (3.7 ± 0.3 Å) observed in experiment and simulation adjacent to the muscovite surface. The correlation length of the interfacial water can be estimated from the widths of the individual layers. Aside from the first two water layers in direct contact with the muscovite surface, the correlation length of the interfacial water is seen to be comparable to molecular dimensions

(since the widths of neighboring layers are larger than the layer spacing). Together, these observations suggest that the interfacial ordering in this case is not the result of the formation of an ice-like layer, but instead an ordered fluid–water structure that retains some of the local structure found in an ice lattice.

2.5.2. Orthoclase (0 0 1) and (0 1 0)

Orthoclase ($KAlSi_3O_8$) is a member of the feldspar group, which includes the most common minerals in Earth's crust. Consequently, feldspars have been studied intensively in the context of mineral weathering and related geochemical cycles [2]. Orthoclase is a framework silicate in which silicon and aluminum tetrahedra are linked to each other by shared oxygens arranged in a 3D network, unlike muscovite, in which they are linked in 2D sheets. K^+ ions balance the lattice charge associated with the substitution of Al^{3+} for Si^{4+}, each randomly distributed in the two tetrahedral sites. The (0 0 1) and (0 1 0) cleavage surfaces are expected to be structurally similar, and both surface orientations have perfect cleavage.

The (0 0 1) surface is rectangular with lattice spacings $|\boldsymbol{a}_1| = 8.57$ Å and $|\boldsymbol{a}_2| = 13.006$ Å, resulting in a unit cell area of 111.5 Å^2 per unit mesh, each having two equivalent tetrahedral rings and two surface K^+ ions. The two likely terminations can be identified by bond counting and have two and four broken bonds per tetrahedral ring for the α- and β-terminated planes, respectively, as shown in Fig. 16a. The determination of the orthoclase (0 0 1) terminating plane is straightforward because the two halves of the unit cell along [0 0 1] are related by symmetry. Consequently, the position of a node in the substrate structure factor along the CTR is directly related to the terminating plane of the lattice [217]. This finger-print analysis of whether the node appears just above or below the (0 0 1) Bragg reflection is directly related to the average separation of the A- and B-layers, which for orthoclase deviates only slightly from $d_{0\,0\,1}/2$ [217]. The appearance of a pseudo-node just above (0 0 1) indicates that the surface has the α-termination as shown in Fig. 16a. This termination is reproduced by model structure factor calculations and is confirmed by least-squares fitting of the data to models [212,213].

Least-squares analysis of the reflectivity data (Fig. 16b) led to the model shown in Fig. 16c. The two bonds broken to create the α-termination are saturated by the completion of the surface tetrahedron at a height of 1.4 ± 0.15 Å above the tetrahedral site [212,213]. The surface K^+ ions are displaced by water molecules (and/or H_3O^+) as judged by the ~2-fold reduction in electron density with respect to a K^+ adsorbed layer, with a derived height of 0.7 ± 0.3 Å above the tetrahedral site and an occupation of 1.35 ± 0.5 water molecules for each surface K^+ ion. The resulting structure, having four NBOs and 4 * 1.35 water molecules per unit mesh, corresponding to an oxygen layer density of 0.08 water/Å^2, again suggests that the NBO and adsorbed water molecules together form a layer whose density is consistent with the formation of a dense water layer. Above this layer, additional layering is observed in the nominal fluid water profile, with a distinct first peak at a height of 2.75 ± 0.1 Å above the tetrahedral site and a fluid water layer spacing of 2.6 ± 0.3 Å. The water density profile converges rapidly to an average fluid-like water density, as dictated by the layer-broadening term, $\sigma_{bar} = 1.0 \pm 0.2$ Å. The

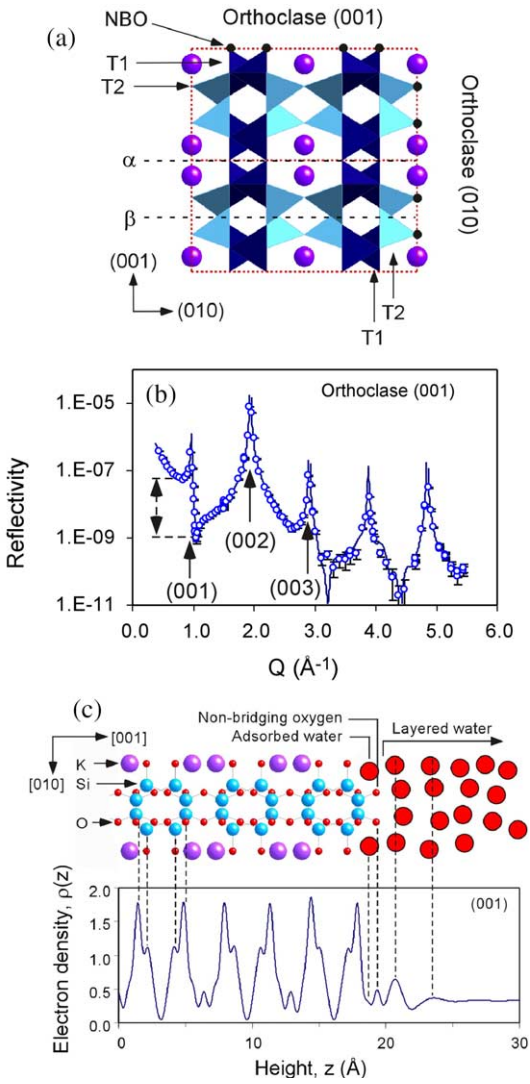

Fig. 16. (a) Schematic side view of the orthoclase (0 0 1) and (0 1 0) surfaces. (b) Specular CTR data for the orthoclase (0 0 1) surface. (C) Structural schematic and derived electron density profile of the orthoclase–water interface. Figures reproduced from P. Fenter, L. Cheng, C. Park, Z. Zhang, N.C. Sturchio, Geochimica et Cosmochimica Acta 67 (2003) 4267–4275, with permission from Elsevier.

correlation length of the interfacial water, derived from Eq. (7), is ~2.8 Å, which is similar to the value derived from studies of supercooled water [166] and clearly suggests a fluid-like nature to the interfacial water. This significant but limited vertical ordering of the fluid water suggests a hydrogen-bonded network, similar to that described for muscovite (Section 2.5.1). However, no lateral structural information is available for testing this idea.

Measurements of the orthoclase (0 1 0) surface showed that it is quite similar to the (0 0 1) surface in all respects [212]. The coordination shells of the surface lattice cations (Si^{4+} and Al^{3+}) are completed through formation of an NBO, and the K^+ ions in the outermost layer are displaced by adsorbed water molecules that interact with BOs. An additional layer of adsorbed water is observed, with weak layering of the fluid water density.

No theoretical studies have addressed the orthoclase–water interface structure, either with MD simulations or ab initio calculations. Given the greater complexity of orthoclase vs. simpler minerals such as calcite, and the relatively large bond valence of Si ($\sim$1 v.u. per bond), we can expect that the completion of the surface tetrahedron with an NBO after cleavage will not be an adsorbed water molecule, but instead is likely to be an adsorbed OH^- which will have $\sim$0.8 v.u. to compensate for the undercoordinated tetrahedral cation. Similarly, the displacement of the K^+ ions will likely be in the form of adsorbed water molecules that are weakly bound to the BO sites, presumably through a hydrogen bond.

These results for the orthoclase–water interface are intermediate between the rather dramatic layering observed for the muscovite–water interface and the much simpler structure found for the quartz–water interface. The observed layering of fluid water is less pronounced than for muscovite. On the other hand, the chemical termination of the lattice through the formation of an NBO and the association of adsorbed water with a BO is similar to results for quartz. However, a second adsorbed water layer observed for orthoclase (0 0 1) and (0 1 0) surfaces is not found as a distinct layer for the quartz (1 0 0) and (1 0 1) surfaces.

3. Mineral–water vapor interface structures

The adsorption of water vapor on mineral surfaces represents a distinct environment in which to study the interaction of water with minerals, and where the presence of bulk water may not be relevant to the phenomena of interest. For example, the knowledge of water films on particle surfaces in humid environments is of primary interest in areas such as atmospheric chemistry [13,14], where such films may play an important role in mediating reactions with reactive atmospheric gases (e.g., NO_x and SO_x). In other cases, the presence of a bulk water film and associated plastic membrane can lead to experimental limitations for the X-ray scattering measurements because of beam attenuation or increased background signals. Direct measurements of water films on mineral surfaces under hydrating conditions (typically humid vapor environments) can provide direct insight in the interaction of these thin water films with the substrate lattice. In this case, the signal and background signals can approach the optimized values that can otherwise only be obtained for studies of mineral surfaces in ultra-high vacuum conditions. For mineral–water vapor interface studies, an ''environmental cell'' can be used (Fig. 17). Here, a water reservoir is maintained separately from the sample and the relative humidity (RH) can be controlled, e.g., through changes in the water reservoir temperature. RH is a thermodynamic variable that is unavailable to studies of min-

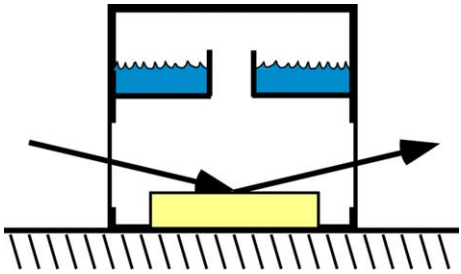

Fig. 17. Schematic of an environmental cell used to probe mineral surfaces in contact with water vapor.

eral–water interface, and it opens up the possibility of gaining more insight into the interactions in these systems through systematic structural measurements (e.g., as a function of RH and temperature). But this extra degree of freedom comes with a price: other thermodynamic quantities such as the pH of the water film cannot be measured and the surface energy can be reduced by adsorption of extraneous species, such as adventitious carbon. Consequently, maintaining the cleanliness of mineral surfaces under these conditions is generally more difficult than mineral–water interfaces. In this section we review the individual results of X-ray scattering studies at mineral–water vapor interfaces. The systems and results are briefly summarized in Table 2.

3.1. Oxides

3.1.1. α-Alumina (0001) and (1−102)

α-Alumina (Al_2O_3, otherwise known as corundum and, with appropriate impurities, sapphire and ruby) is a largely inert high-temperature oxide that is a widely used substrate for thin-film metal growth and catalysis. Because of its hardness, it is also widely used in polishing compounds. Its structure is relatively complex, having six formula units per unit cell of dimensions $a = 4.757$ Å and $c = 12.988$ Å. The lattice structure along [0001] consists of six symmetry-equivalent layers that would express chemically equivalent surfaces, vertically displaced by $c/6 = 2.165$ Å. The alumina

Table 2
Summary of water structures at mineral–water vapor interfaces

Mineral	Surface	Formula	Vertical order	Lateral order	Ref.
α-Alumina	(0001)	Al_2O_3	1 Layer (broad)	N	[147]
	(1−102)		n.o.[a]	n.o.[a]	[287]
Hematite	(0001)	Fe_2O_3	1 Layer	Y	[304]
KDP	(101)	KH_2PO_4	2 Layers	Y	[307]
Brushite	(010)	$CaHPO_4 \cdot 2(H_2O)$	2 Layers	Y	[312]
Halite	(001)	NaCl	1–4 Layers	Y	[322]
KBC	(001)	$K(CrO_3)_2$	n.o.[a]	n.o.[a]	[215]

[a] Not observed.

(0001) surface lattice has three distinct terminations depending on the terminating plane. These are the oxygen, single aluminum, and double aluminum terminations.

Early efforts to understand the structure of alumina surfaces involved mostly UHV studies, such as X-ray CTR measurements [273], low energy electron diffraction (LEED) [274] and ion recoil spectroscopy [275]. These results found inconsistent terminations: Al-terminated surfaces with inwardly relaxed Al atoms for X-ray and ion recoil spectroscopy (Fig. 18a), and a mixed O/Al termination with an outward surface structural relaxation for LEED studies. Theoretical studies using high-level quantum-mechanical approaches generally confirmed the Al-terminated structure as the lowest-energy structure with inward displacements of the surface Al atoms [276–278]. Although these results might have suggested that the behavior of alumina surfaces is relatively simple and well understood, experimental and theoretical advances clearly showed that the interaction of this surface with water exhibits a number of interesting and unexpected properties. Spectroscopic studies demonstrated that the alumina surface becomes hydroxylated at elevated water partial pressures, leading to the formation of surface OH^- species with a threshold pressure of $\sim$2 Torr [101]. Meanwhile, thermal desorption measurements of isotopically labeled water demonstrated that water was dissociatively adsorbed to the alumina (0001) surface as indicated by the observation of isotopically exchanged water upon thermal desorption. This demonstrated that oxygen in thermally desorbed water was derived from both lattice oxygens and adsorbed OH^- [279]. This behavior is very different from earlier studies of the hydroxylation of MgO surfaces which showed that mineral reactivity was associated with surface defect sites [100,280].

Such observations demonstrated that alumina surfaces are chemically active with respect to hydroxylation. At this point, intense theoretical efforts led to a deeper understanding of the reactivity of alumina (0001) surfaces, including the effect of water adsorption dynamics and reaction pathways [281,282], comparison of chemisorption and physisorption modes [283,284], hydrogen adsorption [285], and thermodynamic stability vs. oxygen and hydrogen chemical potentials. Some of the important conclusions derived from these studies include the observation that water chemisorption and dissociation are activated processes that are nonetheless kinetically and thermodynamically favored; understanding these processes was also complicated by the need for large computational cells to accommodate the adsorbed proton [282]. At the same time, the kinetic pathways for observations of isotopic exchange were found, and further disruption of the surface lattice by additional water adsorption suggested the possibility of a transformation to a gibbsite-like oxygen-terminated surface [282]. Further theoretical studies also demonstrated that the thermodynamic stability of the Al-terminated surface depended strongly on the oxygen and hydrogen chemical potentials; in particular the ability to transform into an oxygen-terminated lattice was thermodynamically impeded in the absence of hydrogen [286]. This sensitivity to the presence of adsorbed hydrogen provided a consistent framework with which to understand the apparently contradictory experimental results.

The first structural results of the hydrated alumina surface were performed with CTR measurements [147] of the alumina (0001) surface in 40% RH (after washing

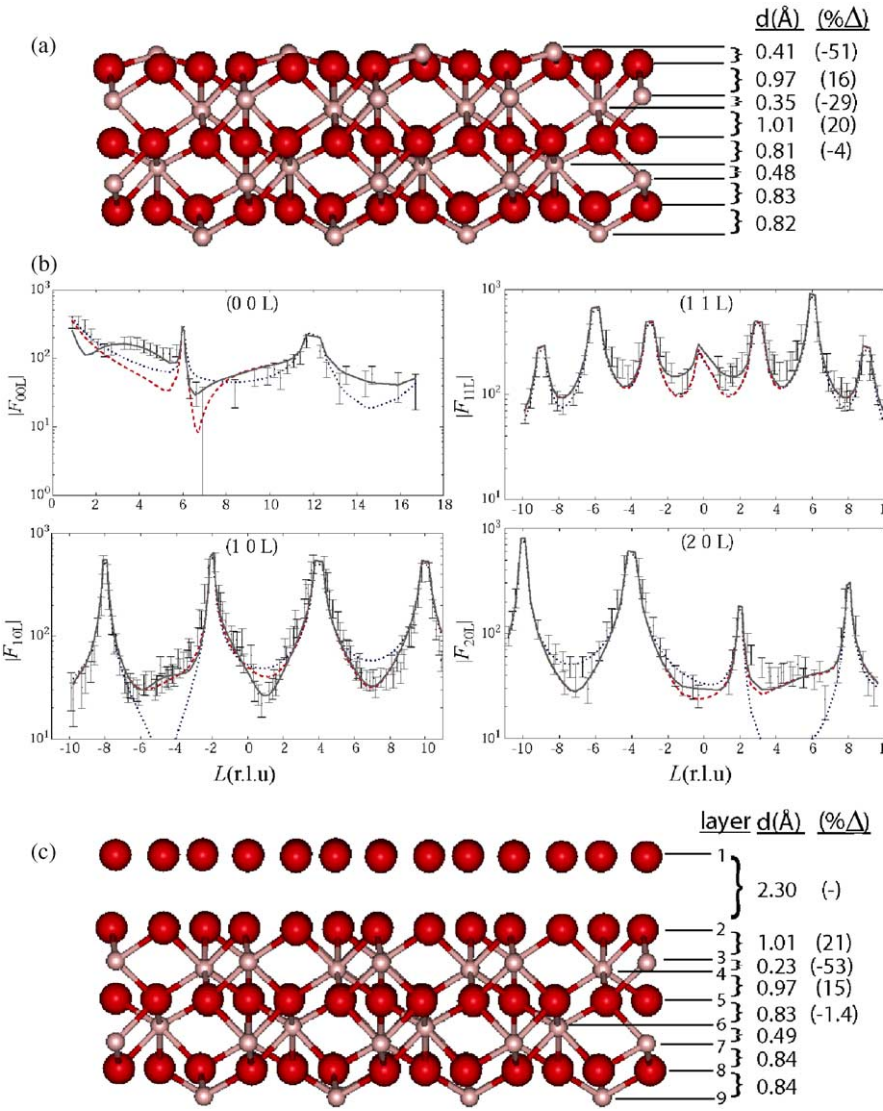

Fig. 18. (a) Structure of the $Al_2O_3(0001)$ surface as measured in ultra-high vacuum condition. (b) Specular and non-specular CTR data of the $Al_2O_3(0001)$–water vapor interface. (c) Derived structural model corresponding to the data in (b). Figures are reproduced from P.J. Eng, T.P. Trainor, G.E. Brown, G.A. Waychunas, M. Newville, S.R. Sutton, M.L. Rivers, Science 288 (2000) 1029–1033. Copyright 2000 AAAS.

the polished surface with water), including both specular and non-specular reflectivity measurements (Fig. 18b). Direct comparison of these data with previous UHV measurements [129] directly confirmed that the surface termination in a water vapor environment is distinct from that found in vacuum. In particular, whereas the

surface in vacuum has a CTR profile that is substantially modulated in intensity between the Bragg peaks (i.e., with respect to the generic variation associated with a CTR), the surface in water vapor has a much simpler CTR profile that was only weakly modulated with respect to the expected intensity profiles. Calculations of model-terminated alumina lattices showed best agreement with the oxygen-terminated surface, but deviations between measured and calculated intensities were substantial. Inclusion of surface structural displacements improved the fit substantially. A quantitative fit to the data was obtained when an overlayer was included in the structure (Fig. 18c). Displacements of the substrate lattice atoms were significant only in the outermost O–Al–Al–O layer. These displacements are large as measured in fractional changes in the interlayer spacings (~50%) but are comparable in size to surface relaxations found in many minerals (<0.26 Å in absolute magnitude). Furthermore, the displacements of these atoms with respect to the ideally-terminated lattice are significant primarily for the Al atoms in the outermost O–Al–Al–O layer. The relatively large Debye–Waller layer of the outermost oxygen layer could indicate small differential displacements of the three surface oxygens that are not resolved by the data, or dynamic fluctuations (e.g., as a result of lateral hydrogen bonding). An overlayer was found 2.3 Å above the surface oxygen atom location with a large Debye–Waller factor (with a rms displacement amplitude of ~1 Å). This was interpreted as a layer of adsorbed water molecules. However the observation of surface carbon by XPS measurements implied that the hydration layer may, in part, be associated with adventitious carbon, possibly explaining the unusually large Debye–Waller parameter for this layer.

A bond valence analysis of lattice atoms at the Al_2O_3(0 0 0 1) surface showed that all surface atoms, except surface oxygen atoms, had their expected bond valences [147]. In contrast, the surface oxygen atoms had a valence of ~1 v.u., in comparison to the expected value of 2 v.u. This suggests that the surface oxygen atoms are coordinated with an adsorbed proton and probably an accepting hydrogen bond from intralayer hydrogen bonds and/or adsorbed water molecules. This layer of adsorbed hydrogen atoms agrees with computational studies showing the importance of hydrogen in the transformation of the surface from an Al- to an O-terminated lattices [286] and the idea that the bond valence lost upon desorption of the surface Al atom could be replaced by adding one hydrogen atom to each of the three oxygen atoms to which the Al atom was coordinated. This example illustrates the usefulness of the bond valence approach to understanding mineral–water terminations as a complement to high-level theoretical approaches that have been applied only to a handful of systems to date.

The alumina (1 −1 0 2) surface was also studied [287]. The (1 −1 0 2) surface can be described as monoclinic and has a unit cell with orthogonal surface parameters of $|\boldsymbol{a}_1| = 4.757$ Å and $|\boldsymbol{a}_2| = 5.127$ Å within the surface plane and a vertical spacing of $\boldsymbol{a}_3 \cdot \boldsymbol{n} = 6.957$ Å. This unit cell has two structurally equivalent $(Al_2O_3)_2$ units with a vertical separation of 3.48 Å between each Al_2O_3 layer. Significant differences with respect to the alumina (0 0 0 1) results described above include a different surface orientation and the use of UHV techniques for surface preparation and environmental control data acquisition. Instead of measuring the surface structure in water vapor as

was done for the (0 0 0 1) surface, the (1 −1 0 2) surface was exposed to water vapor in vacuo with water partial pressures ranging from 1×10^{-8} to 1.6 Torr (with exposures as long as 15 min). Measurements were performed on five non-specular CTRs, including (1, 0), (1, 1), (0, 2), (2, −1), and (2, 0). The primary observation was the absence of measurable changes associated with water dosing, suggesting a weak water–substrate interaction. Analysis of the CTR data led to two models that could not be distinguished based on the basis of X-ray data alone: one model consists of the surface terminated with a partial Al_2O_3 layer and capped by a partial oxygen atom to complete the coordination shell of surface aluminum atoms. The second was fully stoichiometric with a complete Al_2O_3 layer that had undercoordinated surface aluminum atoms missing part of its oxygen coordination shell. Bond valence considerations led to the conclusion that the first model was more chemically plausible, especially after considering the role that adsorbed hydrogen atoms may play to saturate the bond valence of surface oxygen atoms.

3.1.2. Hematite (0 0 0 1)

Iron oxides are pervasive components in various geochemical, environmental, and industrial processes. Iron containing compounds have a rich chemistry that includes various phases (i.e., oxide, hydroxide and oxyhydroxide) and oxidation states (i.e., +2 and +3). Fe is most commonly arranged in an octahedral coordination but tetrahedral coordination is also observed [288]. Iron oxide surface structures are therefore likely to exhibit rich structural and chemical behavior and direct information is needed [47,289]. Hematite (α-Fe_2O_3) is isostructural with α-alumina (α-Al_2O_3) with bulk unit cell dimensions of $a = 5.035$ Å and $c = 13.747$ Å.

The (0 0 0 1) surface of hematite is known to be substantially more reactive than that of α-alumina. For example, hydroxylation of the hematite surface occurs at water partial pressures ~4 orders of magnitude lower than that observed for α-alumina surfaces [101]. Furthermore, it has been observed that this hydroxylated hematite surface is more reactive than the corresponding α-alumina surface with respect to the binding of Pb(II) ions from aqueous solution [290–292]. The relatively low reactivity of the α-alumina (0 0 0 1) surface can be understood through bond valence arguments [293] and such arguments imply that a similar low reactivity should be observed at hematite (0 0 0 1) as well for a similar crystallographic termination.

The hematite (0 0 0 1) surface has been extensively studied under various environments ranging from ultra-high vacuum to aqueous conditions [294–302]. While measurements in ultra-high vacuum conditions initially led to the conclusion that there exists a single highly distorted surface termination [294–296], measurements at higher oxygen and/or water partial pressures found that this surface exhibited two distinct terminations [297,303]. Recent CTR measurements and DFT calculations provide new insight into the structure and reactivity of the hydroxylated hematite (0 0 0 1) surface [304]. Both specular and non-specular CTR data were obtained for the hydrated hematite (0 0 0 1) surface at room temperature with >90% RH [304]. A key experimental result of the CTR measurements was the observation that the surface consists of a partial layer of O–Fe–O species (with an occupancy of ~0.24) on top of a complete and fully hydroxylated O–Fe–Fe–O terminated surface. This

is distinct from what was observed previously for the α-alumina (0001) surface where the surface was uniformly terminated by an hydroxylated O–Al–Al–O layer. An important distinction for the hematite (0001) surface is whether the partial layer is in the form of stoichiometric islands having the O–Fe–O termination surrounded by O–Fe–Fe–O terminated regions, or if the partial layer is in the form of isolated adatoms. While this distinction could not be made solely from the CTR data, previous microscopy studies also identified domains having two distinct terminations of the Fe_2O_3(0001) surface in both vacuum and aqueous conditions [300,305]. An analysis of the CTR data that included two distinct domains provided some additional structural detail, including the observation of a partially ordered water monolayer on each termination, with no additional (fluid) water adsorption [18].

An important feature of this recent work on the hematite (0001) surface was the inclusion of high level computational studies that probed the energetics of various terminations [304]. As in other cases described above, computational tools can be used in conjunction with the X-ray scattering results to provide insights about interfacial proton distributions, which are invisible to the X-ray scattering technique. In this case, the calculations for the hydrated hematite surface [304] incorporated a recently developed approach coupling $T = 0$ K DFT results with thermodynamic information to project the predicted energetics to the temperatures and pressures at which the experiments were performed [286,300,306]. The results show that the most stable surface configurations for hematite (0001) have hydroxylated surface oxygen atoms, with the outer two oxygen layers having one proton per oxygen atom. The water partial pressure threshold for hydroxylation was determined to be several orders of magnitude lower than that for the α-alumina (0001) surface. The absence of two distinct terminations in the DFT calculations with similar energetics is inconsistent with the experimental observation on multiple samples of two co-existing terminations. It was suggested that these differences might reflect experimental details not included in the theoretical models. For instance, a partial layer of Fe adatoms might be derived from the adsorption of aqueous Fe^{3+} species produced by dissolution during sample preparation. Together, these results demonstrate that the hematite (0001) surface has three types of surface hydroxylated oxygen functional groups, including singly, doubly and triply coordinated surface oxygens, and provide a structural explanation for the known differences in reactivity with the corresponding α-alumina surface.

3.2. Phosphates

3.2.1. Potassium dihydrogen phosphate (101)

The structure of the KDP–water interface in contact with bulk water was discussed above in Section 2.4.1. Additional measurements probed the structure of thin water films adsorbed to the KDP surface in an environmental cell with an atmosphere of variable humidity [307]. These measurements in water vapor environments included specular and non-specular reflectivity profiles measured to high resolution (<1 Å vertical spatial resolution). Inspection of the data (Fig. 19a) and comparison to the calculated intensities corresponding to the structure of KDP in contact with

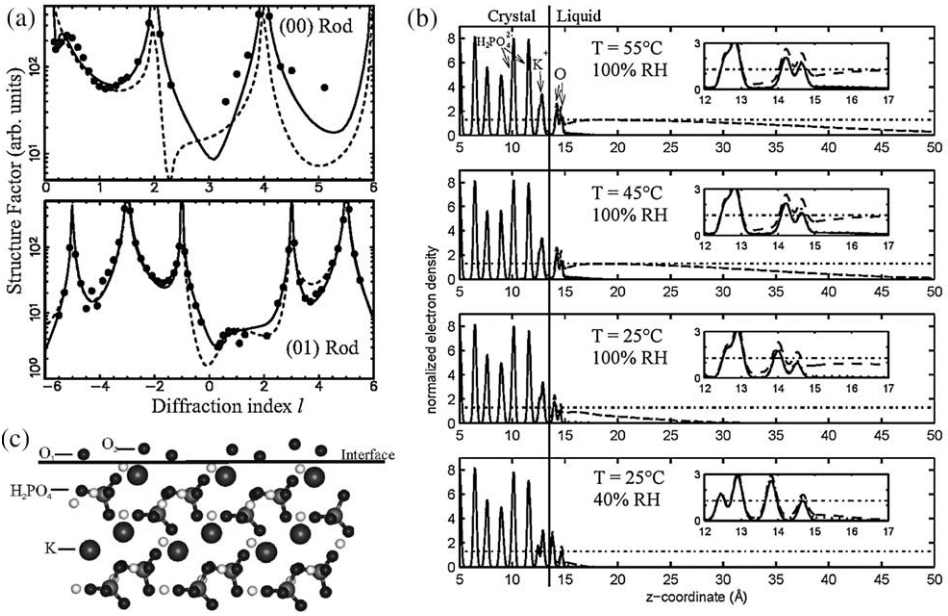

Fig. 19. (a) Specular and non-specular CTRs of the KDP–water vapor interface. (b) Derived electron density profiles. The dashed line shows the actual density profile, and the solid line shows its laterally ordered components. (c) Structural schematic showing the lateral locations of the two laterally ordered ice-like layers. Panels (a) and (c) are reprinted with permission from M.F. Reedijk, J. Arsic, F.F.A. Hollander, S.A. de Vries, E. Vlieg, Liquid order at the interface of KDP crystals with water: evidence for icelike layers, Physical Review Letters 90 (2003) 066103. Copyright 2003 by the American Physical Society. Panel (b) is reprinted with permission from M.F. Reedijk, Ordering at Solid–Liquid Interfaces, Ph.D. thesis, University of Nijmegen, The Netherlands, 2003.

bulk water (dashed line, Fig. 19a) immediately reveals some central features of the system. Data for KDP–water vapor interface are in modest agreement with the calculated non-specular CTR intensities for the KDP–water interface, suggesting that the lateral features are similar for the two systems. A large discrepancy observed for the specular CTRs in these two environments, however, suggests that the vertical structures are distinct, as might be expected for the micrometer vs. nanometer-thick water films in the two studies. What is not immediately clear from these data is whether these differences are extrinsic (i.e., due solely to the difference in water film thickness) or intrinsic (i.e., with different interfacial water structures. A dip in the specular intensity at small Q provides a direct indication of the water film thickness at the KDP–water vapor interface. Since the adsorbed water film has an electron density less than the substrate, the film thickness, W, can be estimated directly from the dip location by $W \sim \pi/Q_0$, where Q_0 is the momentum transfer at the dip location [181]. From this we see that $W \sim 20$ Å, which is similar to the derived value of 22 Å. This suggests that the differences between the measured vs. calculated specular reflectivities largely reflect differences in water film thicknesses.

Structural models for the KDP–water vapor interface were derived by including substrate surface displacements, adsorbed water layers, overlayers that were allowed to have either vertical or lateral order (as described by the Debye–Waller parameters), and a continuous electron density corresponding to that of a fluid water layer [307]. Measurements were performed at ambient conditions, and in a sealed environmental chamber at 25 °C, 45 °C and 55 °C (at 100% RH) and in an ambient environment at 25 °C and 40% RH. The derived density profiles are shown in Fig. 19b [308]. These profiles show the actual laterally averaged electron density (i.e., as derived from the least-squares fitting to structural models), revealing the substrate lattice structure, the presence of two discrete peaks in the electron density associated with adsorbed water molecules, and a broad distribution associated with the fluid water profile. Also shown in Fig. 19b is the part of that electron density that is laterally ordered (highlighted in the insets), accomplished by multiplying each peak in the actual density profile with that atom's Debye–Waller factor. This calculation has the effect of removing from the electron density profile elements that are not laterally ordered and illustrating the relative sensitivity of the CTRs to the derived profile. The results show that although the two adsorbed layers are laterally ordered, the more diffuse continuous electron density profile above the surface is not.

The laterally ordered part of the structure is shown schematically in Fig. 19c [307]. Here, the two ordered adsorbed components are associated with adsorbed water molecules. The first, O_1, sits in a site consistent with the "next layer" K^+ ion that is absent because of the termination of the lattice. The elemental identity of this species is not directly determined, however, and secondary indications are needed. When the species is identified as a water molecule, the derived coverage is 2.1 ± 0.1 waters per unit mesh, double the expected coverage for that site. If this species were identified as K^+, the expected coverage should be reduced by a factor of approximately $Z_O/Z_K = 8/19$, bringing it in line with the coverage expected from crystallographic considerations. The derived height of this species, however, had a substantial inward displacement so that this species, if identified as K^+, would have a 30% reduction in vertical K–K spacing, a result considered unrealistic. The second species, O_2, was also identified as a water species. O_2 was found near the surface K^+ layer and was thought to shield the charge of the K^+ ions. Beyond these two laterally and vertically ordered layers, the contributions to the density profile broadened rapidly indicating a more fluid-like behavior, with a partially ordered oxygen-containing layer, followed by layers that were neither vertically nor laterally ordered. This fluid-like water layer had a rather diffuse profile that decayed slowly away from the interface (over $\sim$30 Å). These results were discussed in the context of ice-like layers and the influence that such layers might have on crystal growth. In particular, if such layers were ice-like, the terrace areas would be expected to be unreactive, because any reactants would need to penetrate through a solid film before reaching the KDP surface and this process should be slow.

The systematic changes in the derived structures in Fig. 19b are an important feature of these measurements [308]. Comparison of the results show important systematic variations in the interfacial structure that are controlled by the sample environment. Substantial changes were observed in the thickness of the continuous

density profile associated with the fluid water layer above the interface, with negligible fluid water under ambient conditions and a ~30-Å-thick film at 55 °C. At the same time, two discrete peaks associated with the adsorbed water were observed under all of these conditions, even at ambient conditions and 40% RH when the fluid water film was largely absent. Perhaps the most interesting aspect of these data concerns the variation of the adsorbed water heights. While substantial changes (~1/2 Å) in the heights of these adsorbed water molecules are observed between ambient conditions and at 25 °C and 45 °C in the environmental chamber, no substantial differences were observed between 45 °C and 55 °C even though the water film thickness changed by ~20%. Furthermore, the high-temperature structure was found to be equivalent to that found previously in measurements of the KDP–water interface (i.e., as described in Section 2.4.1) [309]. The sensitivity of the adsorbed water layer height, especially under the driest conditions, suggests that the coordination of water to the substrate lattice is directly influenced by the availability of fluid water molecules to complete the adsorbed water molecules coordination shell. In particular, the overall reduction in adsorbed water height with decreasing RH is consistent with the increased bonding strength for undercoordinated species as expected from the bond valence model. These results also directly highlight the important structural differences in mineral–water and mineral–water vapor environments, as well as demonstrating the potential to bridge these differences under sufficiently wet conditions.

No theoretical studies have yet been performed to which these results can be compared directly. The crystal structure of KDP has, however, been discussed in the context of bond valence analysis, in which the lattice is stabilized through strong hydrogen bonding between chemically equivalent phosphate units [143]. Although normal hydrogen bonds are expected to provide ~0.8 v.u. when directly bound to an oxygen atom and ~0.2 v.u. when associated with an oxygen atom through a hydrogen bond, the donating and accepting hydrogen bonds in KDP provide 0.6 v.u. and 0.4 v.u., respectively. This difference, if extrapolated to the KDP surface, might explain the high degree of order found in this system, as these stronger hydrogen bonds might lead to a larger adsorption energy of the adsorbed water species.

3.2.2. Brushite (0 1 0)

Brushite, $CaHPO_4 \cdot 2(H_2O)$, is a model biomineral with a structure and composition that are more complex than those of other biominerals (e.g., calcite, apatite) since it incorporates water into the bulk crystal structure. Brushite is a major component of kidney stones and may be involved in the mineralization of bone and teeth [310,311]. Unlike apatite, brushite is a layered structure with alternating $CaHPO_4$ bilayers separated by water bilayers. When grown in gels, brushite crystals form platelets expressing the (0 1 0) surface that are parallel to the $CaHPO_4$ layers. Because water is a primary component of the lattice, one might expect the water structure at brushite surfaces to be more extended and/or ordered than hydration structures found at other minerals, for which an inherent lattice mismatch or strain might preclude extended ordering. Consequently although a water termination of the lattice might be expected, the nature of that termination is unknown. The brushite lattice is monoclinic with surface lattice vectors $|\boldsymbol{a}_1| = 6.239$ Å, $|\boldsymbol{a}_2| = 5.812$ Å, and

$|\boldsymbol{a}_3|$ = 15.18 Å. Due to the A–B stacking of the brushite layers along [0 1 0], the distance between subsequent $CaHPO_4$ bilayers is $|\boldsymbol{a}_3|/2$ = 7.59 Å.

The brushite lattice has four possible terminations because of its lattice structure (single or double layers of either water or $CaHPO_4$). Measurements of the brushite–water vapor interface, including the specular (0,0) rod, plus the (2,0) and (2,−2) non-specular rods, were made in an environmental sample chamber in which the humidity in the vapor phase was fixed at 100% [312]. The vertical structure in brushite is symmetrical about the unit cell center. The specular CTR intensity should exhibit a pseudo-node near the (0 2 0) Bragg peak by termination interference, if the outermost unit cell of brushite—as defined by the lattice termination—retains a center of symmetry [217]. For brushite, the two terminations that satisfy this condition correspond to lattice terminations of either a single water bilayer or a single $CaHPO_4$ bilayer. A calculation of the specular reflectivity for the case of a single water bilayer (Fig. 20a), shows a pseudo-node (i.e., a sharp dip in the reflectivity whose minimum is nonetheless non-zero) just above the (0 2 0) Bragg peak. A similar result with a pseudo-node just below (0 2 0) would be found for the single $CaHPO_4$ termination [217]. The experimental specular reflectivity data do not exhibit these pseudo-nodes and therefore these terminations can be ruled out. The other two possible terminations correspond to the double-water bilayer termination, or to the double-$CaHPO_4$ bilayer termination (i.e., without vertically organized water layers). Such terminations are not distinguished, however, by the specular reflectivity data for an

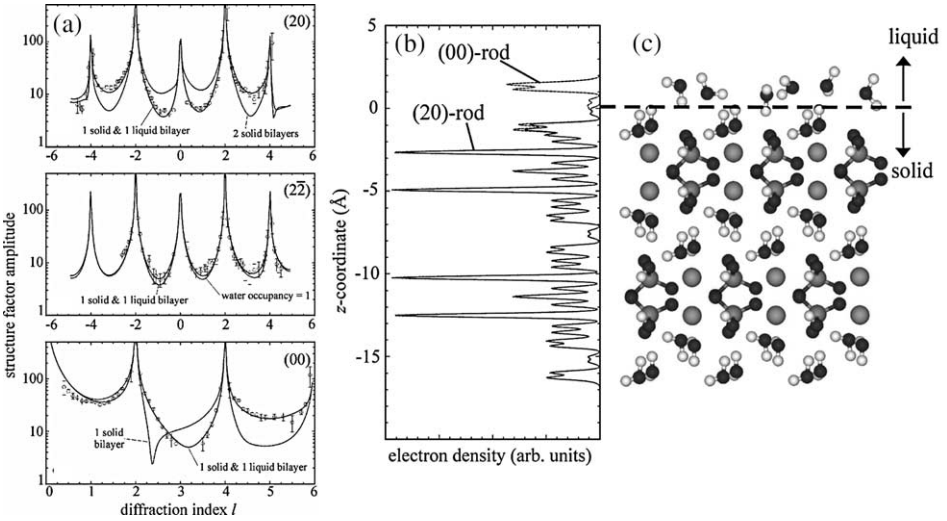

Fig. 20. (a) Specular and non-specular CTRs of the brushite (0 1 0)–water vapor interface. (b) Electron density profiles and (c) structural schematic of the derived interfacial structure. As in Fig. 19, density profiles are shown corresponding to the actual profile and the part of that profile that is laterally ordered. Figures reprinted with permission from J. Arsic, D. Kaminski, P. Poodt, E. Vlieg, Liquid ordering at the brushite-{0 1 0}–water interface, Physical Review B 69 (2004) 245406. Copyright 2004 by the American Physical Society.

ideally-terminated lattice [217]. This ambiguity is resolved by measuring non-specular reflectivity data. Intensity calculations for the (2,0) CTR show substantial disagreement with the data when two laterally ordered water bilayers are included, but they show agreement for a surface with only a single laterally ordered bilayer. This result suggests that although two water bilayers are present, both *vertically* ordered, only the first bilayer is *laterally* ordered and consequently visible to the non-specular CTRs. Refinement of this structure revealed that the first bilayer was displaced from its bulk position by only −0.15 Å, while the second bilayer was outwardly displaced by a larger 0.3 Å. This outward displacement of the second bilayer is consistent with a laterally disordered layer that is presumably only loosely associated with the interface. Internal displacements within a given water bilayer were not included in the analysis, because the Q range of the experimental data does not resolve the two water molecules along the surface-normal direction, since they are separated by ~0.5 Å along this direction whereas the vertical spatial resolution of the X-ray scattering data is $\pi/Q_{max} \sim 1.2$ Å.

No computational studies of the brushite–water interface have yet been done to which these results can be compared. However, indirect insight into the properties of interfacial water has been probed through the adsorption of a fibronectin, a protein associated with the adhesion of cells to extra-cellular materials [313]. In particular, fibronectin did not adsorb to the (0 1 0) surface of brushite, but it did adsorb to {1 0 0} faces. Parallel studies showed that fibronectin also adsorbed to the calcite (1 0 4) surface. Since the brushite (0 1 0) surface is the only one of these that expresses water molecules as part of the crystal structure, it was assumed that these differences in protein–mineral interactions reflected the role of "crystal-bound" water in the brushite (0 1 0) surface lattice. These results for brushite, and those discussed above for calcite (Section 2.2), suggest instead that these differences cannot be simply associated with the presence or absence of a hydration layer, since a hydration layer is observed for both systems. The brushite (0 1 0) hydration layer (in contact with water vapor) is ~4 Å thick and consists of two water bilayers, while for calcite a single hydration layer is found having roughly half that thickness. This suggests that the difference in protein–surface interactions may be derived primarily from the thickness of the two mineral's surface hydration layers.

3.3. Halides: sodium chloride (0 0 1)

The sodium chloride (NaCl) (0 0 1) surface (Fig. 21a) is perhaps one of the simplest mineral–water interfaces in terms of both structure and chemistry. The (0 0 1) surface has perfect cleavage and a square lattice with two interpenetrating face-centered cubic lattices occupied separately by Na^+ and Cl^-. Consequently each ion is octahedrally coordinated by ions of the opposite charge and the two ions are expressed with equal density at the (0 0 1) surface. The crystal structure is cubic with a conventional unit cell lattice spacing of $a = 5.62$ Å. This results in a surface unit mesh with an area of 15.8 $Å^2$ having two Na^+ ions per unit mesh.

Early measurements of water adsorption to NaCl(0 0 1) surfaces performed by FT-IR showed no evidence for an ordered water monolayer [314]. Subsequent

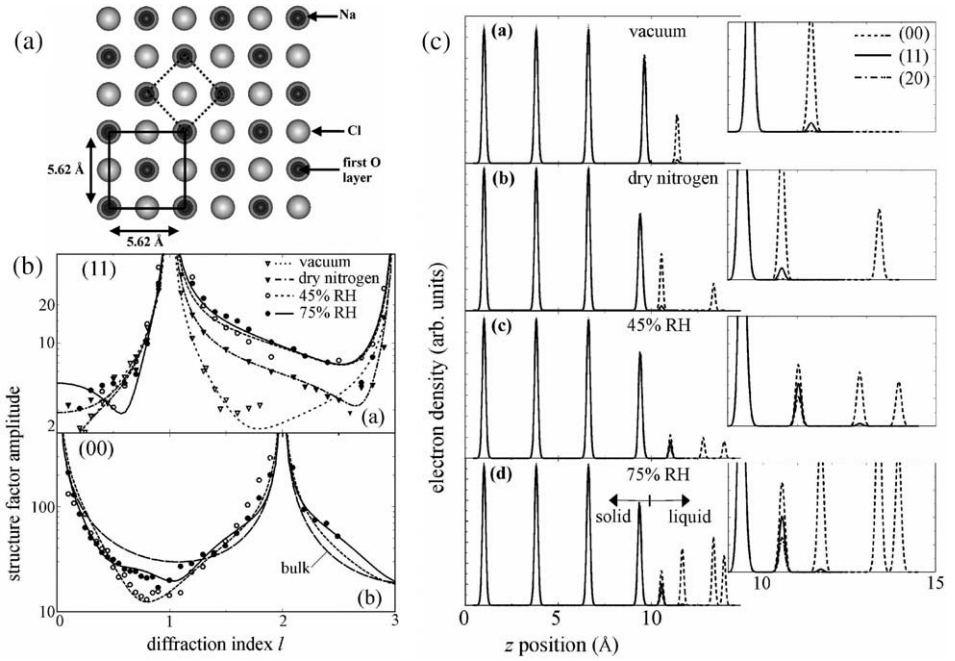

Fig. 21. (a) Top view of the NaCl(1 0 0) surface, indicating the derived location of the first adsorbed water layer. (b) Specular and non-specular CTRs of the NaCl surface at various levels of hydration. (c) Derived total and laterally ordered electron density profiles (dashed and solid lines, respectively) as a function of hydration. Figures are reproduced from [322]. Reprinted with permission from J. Arsic, D.M. Kaminski, N. Radenovic, P. Poodt, W.S. Graswinckel, H.M. Cuppen, E. Vlieg, Journal of Chemical Physics 120 (2004) 9720–9724. Copyright 2004 by the American Institute of Physics.

UHV studies at cryogenic temperatures (~150 K) by LEED and photoelectron spectroscopies showed evidence for distinct gas, 2D, and 3D adsorption regimes [315]. In the 2D adsorption regime, a well-defined monolayer phase having a C(4 × 2) structure [315] was interpreted in the context of a distorted ice bilayer structure. Helium atom diffraction studies at cryogenic temperatures confirmed the presence of a water monolayer adsorbed under UHV conditions but showed a (1 × 1) diffraction pattern that was identical to that of the substrate, indicating no ordered superstructure and implying that each water molecule was adsorbed to a single site. Theoretical models performed in conjunction with the He atom scattering results revealed an adsorption energy of ~50 kJ/mol, explained solely in terms of electrostatic interactions. Atomic force microscopy studies of NaCl(0 0 1) surfaces in contact with both aqueous solutions [316] and as a function of relative humidity [317] clearly demonstrate that the morphology of cleaved NaCl surfaces in contact with water is dynamic.

Quantum-mechanical calculations show that although individual water molecules adsorb with a dipole moment along the surface-normal direction [318], the water molecules adsorb associatively at a height of ~2.3–2.5 Å above the Na^+ site with the water dipole oriented parallel to the surface [318–320]. A more complex

C(4 × 2) structure found at higher coverage is similar to the hexagonal ice structure with water molecules in multiple local environments and two distinct heights of 2.5 and 3.5 Å [320]. Calculations that include surface displacements in the substrate lattice find that the C(4 × 2) bilayer structure is disrupted at 150 K. Molecular dynamics simulations of the NaCl(1 0 0)–water interface [59,321] show that the first three layers of water molecules adjacent to the interface tend to form discrete layers at heights of ~2.2 Å, ~3.5 Å and 6 Å and that the water dipole moment for the first layer is oriented parallel to the surface. Simulations for monolayer and submonolayer coverages show that water molecules are adsorbed to the Na^+ sites, in agreement with earlier quantum-mechanical calculations [59].

Measurements of specular and non-specular reflectivity by Arsic et al. (Fig. 21b) directly probed the variation of the NaCl structure using the (0, 0), (1, 1) and (2, 0) CTRs at various hydration conditions: at UHV, in a dry N_2 atmosphere, and finally at 45% and 75% RH [322]. The data show clear trends as a function of water partial pressure: although the non-specular (1, 1) rod shows a substantial increase in the scattering intensity between the substrate Bragg peaks as the water partial pressure is increased, the specular rod shows a decrease in the measured scattering intensity at the mid-zone position, $L \sim 1$, as well as a small but significant higher-frequency modulation suggesting the formation of a multi-layer water film. Analysis of these data revealed the structures in Fig. 21c. As in the KDP–water interfaces, the results are presented to highlight the total electron densities as well as the effective density profiles as seen in the non-specular CTRs which show only the laterally ordered material.

Measurements of the NaCl(1 0 0) surface in vacuum (after cleavage in air and subsequent annealing for 30 min at 60 °C in vacuum) show the presence of an adsorbate layer interpreted as a water layer [322]. Indeed, analysis of this surface revealed that the adsorbate is consistent with a complete water monolayer (1 water per surface Na^+ ion) located 1.55 Å above the surface Na^+ ion. This water layer has a well-defined height with a rms height distribution of 0.1 Å but a lateral rms width of 1.5 Å, suggesting it is well-ordered in the vertical direction, but is poorly ordered in the lateral direction. The lateral disorder does not appear to be consistent with the lateral static structural displacement of 0.8 Å that was derived from theoretical work for an ordered monolayer of water [320,323]. Measurements show that the surface Na^+ and Cl^- ions have similar outward displacements of 0.22 and 0.16 Å, respectively, corresponding to a fractional displacement of 6.7% with respect to the traditional unit cell spacing of 5.62 Å (consisting of two NaCl layers).

Measurements in dry N_2 show significant changes with respect to the surface in UHV [322]. The first water layer observed in UHV was still present with similar coverage, lateral position, and rms widths, but it had a height with respect to the surface Na^+ ion of only 1.06 Å. In addition to this first layer, a second water layer was observed at a height of 3.93 Å having an occupancy of 0.7 Å but with no evidence for lateral order. Consequently this second layer is not visible in the density profiles derived from the non-specular rods. The structural displacements of the NaCl surface become substantially smaller in dry N_2 and have vertical surface displacements of 0.06 Å and −0.04 Å for Na^+ and Cl^-, respectively.

When RH is increased to 45% and 75%, significant changes took place involving the occupation, height, and rms widths of the subsequent water layers [322]. The first water layer in direct contact with the NaCl surface had a significantly smaller lateral rms width of ~0.6 Å and was found at heights of 1.54 Å and 1.19 Å, at 45% and 75% RH, respectively. The second water layer, which was not laterally ordered in dry N_2, became modestly more ordered at 45% and 75% RH, with a lateral rms width of ~1.6 Å. At the same time, its height decreased monotonically with increasing RH with heights of 3.4 Å at 45% RH and 2.3 Å at 75% RH. A third and fourth water layer are observed at 45% and 75% RH, respectively. These layers did not acquire any lateral order, but the third layer had a height that was sensitive to RH (as had been found for the second layer), with heights of 4.5 Å at 45% RH and 4.0 Å at 75% RH. The fourth layer was found at a height of 4.6 Å at 75% RH.

Comparison of these results to the previous experimental and computational results is difficult because of the differences in experimental conditions (e.g., cryogenic temperatures in vacuum vs. ambient conditions with controlled humidity). However, with those differences in mind, comparisons can still be made. The observation that the NaCl surface in vacuum retains a single hydration layer (after cleavage in air) is consistent with previous measurements showing differences for air- and vacuum-cleaved samples [324]. The surface structural displacements for the air-cleaved sample in vacuum, however, were substantially larger (~6%) than those observed for samples cleaved in vacuum [315,324], and those at ambient conditions for RH of 0%, 45%, and 75%. The most surprising result of these measurements is the observation that the first water layer was found at heights ranging from 1.1 Å to 1.6 Å. This height is substantially smaller than the values of ~2.3–2.5 Å derived from theoretical studies and the expected Na–O bondlength of ~2.4 Å based upon the crystallographic radii of Na^+ and O^{2-}.

3.4. Chromates: potassium dichromate (001)

Potassium dichromate (KBC, $K_2Cr_2O_7$), has been studied for many years primarily from the context of crystal growth [325–327] but also in the context of the morphology of cleaved surfaces [328,329]. The KBC crystal structure consists of alternating A–B–A–B layers along [001], where the A- and B-layers each contain of two $K_2Cr_2O_7$ molecules. An interesting aspect of the KBC system is that it exhibits the phenomenon of hypomorphism, in which the macroscopically observed growth structure shows a lower symmetry than that determined by X-ray crystallography. This is reflected by observations that the growth morphology of the (001) and (00−1) surfaces are different: the (001) surface is a smooth face with larger spirals while the (00−1) surface is rougher [330]. Another key feature of the KBC structure is that the A- and B-layers, while structurally similar are not related by symmetry and the A-terminated face is found to be thermodynamically favored. Consequently, the cleavage of KBC results in two non-identical twin (001) cleavage faces having distinct A- and B-terminated surfaces. While the (001) surface is stable in contact with the growth solution, KBC is known to develop an "etch-resistant layer" when placed

in contact with air [330]. This layer can be removed by etching the surface in de-ionized water but passivates the surface with respect to weaker etching solutions.

X-ray scattering measurements provided direct insight into many of these complex interfacial phenomena, but especially the formation of the etch-resistant layer [215]. Measurements of the (0 0 1) surface as a function of time in air showed that the specular CTR exhibited strong changes (particularly at small Q) indicating the formation of an etch-resistant layer. At the same time, there were no significant changes to the non-specular (1, 0) CTR. This indicates that the etch-resistant layer is not laterally coherent with the substrate lattice. After etching this surface with water, specular reflectivity measurements showed that the etch-resistant layer was removed.

Measurements of the non-specular (1, 0) and (2, 1) CTRs were obtained at 40% and 100% humidity, making use of the insensitivity of the non-specular CTRs to the etch-resistant layer to obtain insight into the interface between the undisturbed KBC crystal and the etch-resistant layer [215]. These results showed surprising sensitivity to RH, with substantially weaker scattering and increased background at 100% RH with respect to the data at 40% RH that was similar to that found in air. Analysis of these data by comparing to structural models leads to the conclusion that KBC crystal retains the A-termination for both humidities with K^+ at the surface, but with different surface structural relaxations. The ability of the KBC surface to restructure when changing from 40% to 100% RH suggests that the etch-resistant layer is permeable to water.

Beyond the specific interest in KBC and crystal growth, an important aspect of this work is that it demonstrates the potentially high sensitivity of a mineral surface to its environment, especially as it is changed from a mineral–water interface to a mineral–water vapor interface, and when the RH is changed. In particular, these data suggest that while KBC in contract with its growth solution at thermodynamic equilibrium is stable and morphologically smooth, when transferred to air and/or environments with controlled humidity, significant changes were observed in the surface structure and termination which were directly sensitive to changes in RH. These structural changes include the development of an etch-resistant layer and a structurally distorted interfacial structure. Separate AFM measurements suggest that an additional water layer may be found on top of the etch-resistant layer, although this was not observed in the X-ray results [331]. These results reveal a much more complex surface termination than is found for any of the other mineral interfaces described above.

4. Discussion and conclusions

4.1. Mineral surface termination

Mineral surfaces in contact with water (either as bulk water films or water vapor) were found to have well-defined terminations and only minor structural displacements with respect to the bulk lattice locations in most studies measured by X-ray

reflectivity. In systems where comparable studies have been performed in UHV, mineral terminations are clearly sensitive to their environment. For example, $Al_2O_3(0\,0\,0\,1)$ has an Al-terminated structure in vacuum [273], but an oxygen-terminated structure in contact with water vapor (and after washing in water) [147], presumably because of the removal of the surface Al atom. Similarly, rutile $(1\,1\,0)$ is terminated by BOs and 5-fold coordinated Ti atoms in vacuum [129], but upon exposure to water, the coordination of water to the bare Ti atoms results in complete passivation of the exposed Ti atoms leading to an oxygen-terminated surface [223].

A general conclusion of these studies is that structural displacements in the near-surface region are generally small (in absolute displacements) and do not extend deeply into the crystal. Even for systems such as $Al_2O_3(0\,0\,0\,1)$, where the fractional changes in interlayer spacing are large (~50%), the absolute displacements are modest in size (<0.3 Å) and comparable, if somewhat larger than, surface displacements found for other mineral–water interfaces. For nearly all of these systems, RH does not influence the mineral termination but instead affects only the behavior of adsorbed water layers and fluid water films. One important exception is the KBC $(0\,0\,1)$ surface which develops a larger-scale etch-resistant layer when the surface is in contact with air, and the KBC–etch-resistant layer interface structure is shown to be sensitive to RH.

4.2. Surface hydration layers

A common feature of mineral–water interfaces is the nearly universal observation of "hydration layers" immediately adjacent to the mineral surface, as summarized in Table 1. Beyond this first hydration layer, the degree to which these layers are influenced by the mineral surface varies greatly. At one extreme, the interfacial water structure at the muscovite–water interface includes a surface hydration layer, plus what appears to be a weakly modulated fluid layer extending ~10 Å from the surface. This profile is qualitatively similar to the O–O pair correlation function in liquid water. In some cases, including the orthoclase and fluorapatite surfaces, a less-extended interfacial water structure is observed with a weak but significant modulation of the fluid water beyond the surface hydration layer. In other cases, including calcite, rutile, RuO_2, quartz, and barite surfaces, the only significant ordering observed was the formation of the hydration layer itself. Measurements at the KDP– and ADP–water interfaces did not identify any interfacial water structure, but only non-specular CTRs were included in these measurements, and therefore features of the interfacial structure that are not laterally ordered would not be observed. These observations indicate that the nature and extent of any interfacial water layer is quite sensitive to the details of the mineral surface. That is, both steric and chemical effects play direct roles in the ordering of interfacial water. This is not surprising from a fundamental perspective, because the structure and stability of an adsorbate layer are normally intimately associated with molecular-scale features such as bonding, steric effects, and lattice strain.

The primary surface hydration layer at these mineral–water interfaces was laterally ordered in all cases where such layers are known to exist and where the lateral

structures were measured (rutile, calcite, RuO_2). In each case, the order could be identified either as due to the completion of surface cation coordination shells (i.e., calcite, barite) or due to an interaction between the water molecules in the hydration layer and the surface lattice oxygens. In the case of RuO_2, both the surface hydration layer and the surface oxygen lattice could be substantially changed with the electrochemical potential: a surface hydration layer above the surface BO and TO sites is formed at sufficiently positive potentials and is comparable to that observed at the rutile–water interface. This shows that such layers may not be general for all surfaces. Additional changes to the surface oxygen lattice are also observed, but are probably outside the realm of control expected solely due to changes in solution chemistry (pH, ionic strength, etc.). Nevertheless, these results demonstrate that there is thermodynamic control over the hydration layer. Therefore, we might expect significant changes to the nature or degree of order in the surface hydration layer as a function of solution chemistry, at least for systems where the surface layers are weakly bound. Even where lateral structures were not probed, the derived water molecule coverage corresponded to a crystallographically dictated coverage associated with a particular surface site (e.g., the surface metal cation at barite, the BO site for quartz, the ditrigonal site in muscovite). In each case, these crystallographically dictated coverages are substantially smaller than that of a dense water monolayer, suggesting that epitaxy with the substrate is a dominant factor and implying (but not proving) that such species are laterally ordered. Studies that probe only the vertical structure (i.e., with specular reflectivity) are likely to miss aspects of the structure that are only weakly ordered. For example, non-specular reflectivity data were needed to see the complete surface hydration layer for calcite, whereas only the most ordered part of that layer could be seen with specular reflectivity. The observation of 2D ordered water structures in these hydration layers confirms the critical surface-specific control of the ordering of interfacial water.

Studies of mineral–water vapor interfaces show similar richness in behavior, as summarized in Table 2. Surface hydration layers were observed in nearly all cases and were vertically ordered with respect to the substrate lattice. A continuous electron density profile associated with a water film was also observed for KDP. In most cases, the hydration layer in direct contact with the substrate was laterally ordered. An exception to this trend is the $Al_2O_3(0\,0\,0\,1)$ surface, where the surface hydration layer was only weakly ordered vertically, with no evidence for lateral order. Similarly, measurements of $Al_2O_3(1\,-1\,0\,2)$ in vacuum showed no evidence for adsorption of water at vapor pressures as high as $\sim$2 Torr. Although all of these studies were performed in contact with water vapor, studies at the NaCl surface made full use of this extra degree of freedom to observe changes in the surface hydration layers as a function of RH. In these studies, an interesting result concerned the development of order in the hydration layer. A primary surface hydration layer was found even under UHV conditions (after cleavage of the surface in air) but this layer was only weakly ordered in the lateral direction. The same layer was found to acquire more lateral order in dry N_2 and an even higher degree of lateral order with respect to the substrate lattice at 45% and 75% RH. In the case of KDP, a primary hydration layer was observed under all conditions studied, but the precise position of the

adsorbed water molecules depended upon the environmental conditions. Consistency of this primary hydration layer structure with results at the KDP–water interface was observed only when the laterally disordered fluid-like water layer exceeded ~25 Å.

Another interesting aspect of these data is the vertical extent of the hydration layer formed mineral–water vapor interfaces. For $Al_2O_3(0001)$ and brushite (010), only a primary hydration layer was observed, even when measurements were performed at 100% RH [147,312] with no evidence for any fluid-like layers. Similarly, no adsorbed water layers were observed for $Al_2O_3(1\bar{1}02)$ surfaces in UHV, even after exposures to ~1.6 Torr of water vapor [287]. However, measurements of the KDP (101) surface at 100% RH showed both a discrete hydration layer and a ~20 Å thick fluid-like water layer whose thickness varied from 10 Å to 30 Å when controlled by temperature [308]. These observations show that the properties of the thin-water films are strongly governed by the substrate surface, presumably described by the wetting characteristics of water on these surfaces.

An important technical issue related to the mineral–water vapor studies concerns the composition of the apparent hydration layers. Adventitious carbon can readily adsorb to mineral surfaces in contact with ambient atmospheres. In nearly every case described above, sample processing or transport through the ambient environment means that such layers can be present. Interaction with fluid water might be expected to displace adventitious carbon layers at the mineral–water interface because these interfaces are close to equilibrium and are in contact with an effectively infinite reservoir. Such layers are difficult to avoid at mineral–vapor interfaces; their formation is likely to be thermodynamically driven because they can reduce the surface energy of mineral surfaces, especially at low RH. At the same time, these layers tend to have high X-ray contrast for mineral–water vapor measurements since their electron densities can be roughly one-half of the substrate electron density. In the case of $Al_2O_3(0001)$, XPS studies showed that a fraction of the nominal hydration layer could be attributed to adventitious carbon [147]. Such layers might account for some of the unexpected variability observed in precise hydration layer heights as a function of RH [322]. Completely eliminating the sources of such adventitious carbon (e.g., as impurities in the water vapor carrier gas) is exceedingly difficult except through the use of UHV techniques. The UHV approach is often not appropriate for these studies as the ambient atmosphere is an intrinsic part of the system. However, it should be possible to address the role that adventitious carbon might play in these systems by measuring the reversibility of the X-ray scattering data directly as a function of RH. To our knowledge, such studies have not been reported. Measurements of the KDP– and NaCl–water vapor interfaces at multiple conditions, however, showed systematic variations of water film thickness, which is an important first step in this direction [308,322].

4.2.1. "Ice-like" vs. "water-like" hydration layers

Much discussion in the literature has suggested the presence of ice-like behavior of interfacial water, not only at mineral–water [93] and mineral–vapor interfaces [109,272,307], but also at metal–aqueous interfaces [91,92,94] and at free water sur-

faces [108,110,332]. These ideas derive from both spectroscopic measurements (primarily non-linear optical studies) and structural measurements (e.g., X-ray scattering and AFM measurements). Surface-specific spectroscopic measurements (using optical sum frequency generation, SFG) typically see both ice-like and 'water-like' behavior at solid–liquid interfaces, where this identification of behavior derives from comparison of O–H vibrational stretch frequency shifts with respect to those found in different phases of water. A more detailed analysis of the non-linear optical spectra for water vapor interfaces suggests a more liquid-like interfacial structure [123,333]. This behavior has been observed over a range of solid–liquid and solid–vapor interfaces, suggesting that the results are general. In particular, two systems in which SFG measurements have been reported that are most closely related to results derived from X-ray scattering measurements are the quartz–water interface (for both fused quartz and crystalline quartz) [109,112] and the muscovite–water vapor interface [272]. The correspondence between these measurements and the structural results discussed above suggests that the ice-like water layer identified in SFG studies corresponds to the primary hydration layer observed in X-ray diffraction studies, as was first suggested by Reedijk et al. for the KDP–water vapor system [307]. In this respect, the water-like peak in the SFG spectra may correspond to either the more weakly vertically ordered water layers near the interface or to water molecules that are orientationally aligned by the static electric field derived from the mineral surface charge.

To what extent do these spectroscopically-identified ice-like surface layers have properties associated with ice? Should this layer simply be viewed as a hydration layer or adsorbed water layer? If the hydration layer is truly ice-like, its tendency to form would be strongly controlled by the substrate lattice spacings, symmetry, and interactions (covalent vs. ionic interactions). In addition, such layers should have a structure corresponding to that of one of the many bulk ice structures. These layers form on substrates of widely varying lattice spacings and are also laterally ordered. If these layers were truly ice-like, the epitaxial relationships between the water and the substrate lattice should have a very strong influence upon the ability to form such ice-like layers, much as the epitaxy of inorganic materials is strongly dependent on lattice matching and strain. The generality of ordered surface hydration layers suggests that it is unlikely that such layers can be characterized structurally as ice-like.

In the case of muscovite, where the substrate lattice spacing and symmetry approaches that of hexagonal ice most closely (i.e., with a vertical spacing between water molecules of $\sim$1.2 Å in the hydration layer, similar to the spacing of 0.9 Å within a bilayer of hexagonal ice, and with a 14% difference in 2D lattice spacing between muscovite and ice structures), the most extended interfacial water structure is found, having a complete hydration layer and weak modulation of the fluid water structure $\sim$1 nm from the interface. Results of MD simulations, which show overall agreement with the density profile derived from X-ray scattering results for the muscovite–water interface, show that only the first adsorbed water layer is laterally ordered, corresponding to the substitution of water (and/or H_3O^+) into the ditrigonal sites on the muscovite surface lattice. The lack of any lateral order in subsequent

layers suggests that this hydration layer should be interpreted in the context of a modulated fluid. However, the SFG studies for muscovite were performed in contact with water vapor, and substantial differences in structure and dynamics for mineral–water and mineral–water vapor interfaces cannot be excluded.

Perhaps the closest comparison can be made for quartz surfaces. SFG studies show the ice-like and water-like spectroscopic features, both for the surface of fused quartz (which is amorphous) and for the quartz (0 0 0 1) surface [109,110,112]. The X-ray scattering results for the quartz (1 0 1) and (1 0 0) surfaces in water clearly show the presence of a hydration layer with little or no modulation of the fluid water structure farther from the interface [221]. Analysis of the hydration layer height and occupancy shows that the hydration layer is likely due to water hydrogen bonding to the bridging oxygens exposed at these surfaces. The overall similarity of the SFG data for fused and (0 0 0 1) quartz surfaces (with, however, subtle spectroscopic differences in the ice-like layer for the two systems), plus the absence of any ice-like structures in the X-ray reflectivity results, suggests again that the ice-like layers seen in SFG studies correspond to the hydration layer identified by X-ray reflectivity.

A separate indication of the nature of these hydration layers derives from their properties. In particular, the formation of an ice-like layer might be expected to lead to low reactivity of flat terraces on mineral surfaces by physical passivation (e.g., by forming a solid surface coating that prevents the exchange of ions to and from the solution). This has been proposed as an explanation for the observation that mineral growth often occurs primarily at steps, as opposed to through homogeneous nucleation at terraces [307]. This idea can be probed directly through measurements of ion adsorption sites at mineral–water interfaces. Recent measurements at the rutile (1 1 0) surface [223,334] clearly show that mono-, di- and trivalent ions are adsorbed as inner-sphere adsorbates and can readily penetrate the hydration layer when they are adsorbed at the interface. Similar observations have been made for muscovite surfaces [214,335], where ice-like layers have been spectroscopically identified [272].

Within the expected distribution of behavior and properties, especially given the various structures and interactions of these diverse systems, we can reasonably infer that the hydration layers observed in X-ray scattering measurements correspond to the spectroscopically-identified ice-like features. The ice-like character of these layers presumably derive from the restricted geometry of these adsorbed water molecules, perhaps resulting in a hydrogen bonding environment that is locally similar to that found in ice. This assignment suggests that the relative inertness of terraces at the mineral–water interface is not a result of a physical passivation of the surface by a solid ice-like layer, but instead by a chemical passivation of the terraces by the adsorption of water molecules (e.g., by either completion of lattice cation coordination shells, or by hydrogen bonding to surface oxygens). The ability of ions to penetrate this layer suggests that the hydration layer is dynamic and not static, and is consistent with NMR data showing that exchange rates of oxygen in hydration layers varies by many orders of magnitude [336–338]. Definitive tests concerning the nature of the spectroscopically-identified ice-like layers could be performed by observing the effect of adsorbed ions on the SFG spectra in systems where inner-

sphere ion adsorption is known to displace water molecules from the surface hydration layer.

4.2.2. Spatial extent of surface hydration layers

A number of interrelated formalisms and concepts can be used to consider the extent of ordering in surface hydration layers. As seen from the perspective of the bond valence model, the net bonding strength available to a water molecule is fixed. Consequently, a water molecule with one strong hydrogen bond will have correspondingly weakened hydrogen bonding strength in its other interactions. This suggests that water molecules in strongly bound hydration layers tend to have weakened interactions with other water molecules, leading to compact hydration layers that interact only weakly with fluid water. The ability to form an extended hydrogen-bonded network in a surface hydration layer then necessarily requires an interaction between water and the mineral surface that is relatively weak and comparable to water–water hydrogen bonding interactions. This conclusion is consistent with the observation that mineral–water interfaces having exposed metal cations (e.g., calcite, barite) with strong substrate–water interactions show very compact hydration layers. In contrast, the most extended hydration layers are found for silicates, in which broken bonds are saturated through formation of NBOs, and in which much of the water interaction can be thought of as due to hydrogen bonding to the lattice oxygens. The limitation of this simple picture can be seen by noting that quartz surfaces do not show extended ordering, even though its surface is similar to the orthoclase surface which shows a greater extent of ordering.

The observation of lateral order in hydration layers that is commensurate with the substrate lattice, both at mineral–water and mineral–water vapor interfaces, means that adsorbed water molecules generally adopt the substrate lattice spacings. In this respect these hydration layers might be considered in the context of strained layer epitaxy with hexagonal ice as the reference phase for the hydration layer. From the large literature of inorganic epitaxy, it is clear that the vertical extent of any such ordering is limited when there is significant strain. In particular, beyond a critical thickness determined by the degree of film lattice strain, the film energy will be decreased either by changes in film morphology (e.g., islands vs. uniform film) or by the introduction of dislocations. A typical critical thickness of $\sim$10 Å is found for lattice strain of $\sim$4% [339]. Because the system with the best lattice match to hexagonal ice was found in muscovite, albeit with a $\sim$14% lattice mismatch, we can expect that any coherent ice-like lattice would be extremely thin, probably only one molecular water layer thick. This observation is consistent with experimental observations by X-ray scattering for muscovite and other systems discussed above, in which ordering of water is limited.

The literature of the wetting of fluids on solid substrates provides some additional insight. Here the ability of a fluid to form a continuous film depends on both the interface energies and the long-range van der Waals interactions of the water film with the substrate lattice [340–342]. Wetting behavior can be probed by contact angles between the fluid and substrate lattices, or by measuring the thickness of the wetting film as a function of vapor pressure. In this respect, wetting behavior is

separated into regimes: non-wetting (large contact angles, no adsorption), incomplete wetting (formation of a thin film that is otherwise non-wetting to further adsorption), and wetting (zero contact angle and diverging film thickness). The ready formation of hydration layers in the mineral–vapor studies discussed above suggests that formation of the initial ordered layer is due to relatively strong water–mineral interaction, while the subsequent system-specific development of additional, often laterally disordered layers are associated with the specific interactions of these systems.

Finally, we compare to the ordering found at liquid–vapor interfaces by X-ray scattering techniques. No evidence for layering of water at the water–vapor interface is observed [343,344]. In contrast, similar measurements of liquid metal and binary-metal alloy surfaces show layering that is qualitatively comparable to that found for water at the mineral–water interface [204,345–349]. In particular, the correlation length of the modulated surface layer was typically comparable to that in the bulk liquid metal [343]. Because the correlation length of water is comparable to the water molecule size, the perturbations of the fluid–water structure at mineral–water interfaces should be limited to a narrow region near the interface. The lack of observable ordering of water at water–vapor interfaces highlights the central role of the mineral surface in inducing order in the hydration layer, consistent with the expected strong mineral–water interactions.

4.3. Summary

The work described here gives a snapshot of an area that is young but growing rapidly, with the earliest work reviewed here appearing only in 2000. These data provide the first "structural" views of mineral–water interface structures and the properties of interfacial water that were previously accessible only through spectroscopic and theoretical approaches. In particular, these results demonstrate that surface hydration layers (that are vertically, and often laterally, ordered) appear to be a general characteristic of mineral–water and mineral–water vapor interfaces. Given the relatively recent appearance of work in this area, further developments in many other mineral–water systems can be expected, as well as the fine-tuning of these initial results as more complete data are obtained and more systematic studies are performed.

There are many areas where extensions of this work can be expected. Certainly experimental results will be obtained for additional minerals and more detailed results for systems that have already been studied. These initial results show very clearly that direct comparison of structural results derived from X-ray scattering measurements with spectroscopic and computational studies has led to a deeper, more complete understanding of these systems and has allowed potential gaps in our understanding (either theoretical or experimental) to be identified. Additional efforts to combine experimentally measured structures with computational results are likely to yield substantial new insights. Such comparisons will certainly lead to a better understanding of protonation at mineral–water interfaces, because protons are essentially invisible to X-ray scattering. This may be addressed by neutron scattering,

by making use of the strong contrast between protons and deuterons [105]. Measurements of changes to the interfacial water structure as a function of pH are likely to provide a new understanding of charged interfaces that is highly complementary to earlier spectroscopic results [107,109–111]. The application of these techniques to probe the properties of interfacial water at elevated temperatures, and especially under hydrothermal conditions, is another important opportunity.

A major direction of future study concerns the extension of this work to probe ion adsorption at mineral–water interfaces. Such studies can lead to a more complete understanding of the electrical double layer structure. In these systems we can anticipate additional complexity of phenomena, as competition between mineral and ion hydration and long-ranged electrostatic attraction/repulsion to introduce an additional balance into the interfacial energetics, and direct competition for available surface sites between adsorbing ions and the interfacial water. Although such behavior has been extensively studied with X-ray absorption spectroscopy [38], only recently has X-ray scattering been applied to such systems [223]. Use of other complementary techniques such as X-ray standing waves [223,334] is likely to provide a powerful complement to these X-ray scattering techniques.

Recent studies have shown the feasibility of probing the structure of fluids confined between two solid walls [88,89]. Such studies, especially when applied with higher resolution to understand the structure of confined water films, will bring these techniques full circle back to some of the original phenomena that were a significant motivation for much of the work described here.

Acknowledgments

We would like to acknowledge the many contributions that made this review possible. Part of the original work reviewed here was done by the Interfacial Processes Group at Argonne National Laboratory and involved a large number of researchers. Key contributions to this work were made by Likwan Cheng, Ron Chiarello, Phillip Geissbühler, Changyong Park, Michel Schlegel, and Zhan Zhang. We also acknowledge ongoing interactions with Michael J. Bedzyk, Michael L. Machesky, Kathryn L. Nagy, and David J. Wesolowski. This work was supported by the Department of Energy, through the Office of Basic Energy Sciences (Division of Chemical Sciences, Geosciences and Biosciences). We would also like to thank Elias Vlieg for supplying pre-prints and other unpublished results, and Hoydoo You, Marianne Reedijk, Thomas Trainor, and Jon Sorenson for permission to reprint figures.

All of the work described in this manuscript is possible only as a result of the many synchrotron radiation user facilities that have become available in the past decades. Measurements by the Interfacial Processes Group were done at the Advanced Photon Source (Argonne National Laboratory) and the National Synchrotron Light Source (Brookhaven National Laboratory). The Advanced Photon Source was supported by the US Department of Energy, Office of Science, Office of Basic Energy Sciences, under Contract No. W-31-109-ENG-38. The National Synchrotron Light Source is supported by the US Department of Energy, Division

of Materials Sciences and Division of Chemical Sciences, under Contract No. DE-AC02-98CH10886.

References

[1] L.R. Kump, S.L. Brantley, M.A. Arthur, Chemical, weathering, atmospheric CO_2, and climate, Annual Review of Earth and Planetary Sciences 28 (2000) 611–667.
[2] A.F. White, S.L. Brantley (Eds.), Chemical Weathering Rates of Silicate Minerals, vol. 31, Mineralogical Society of America, Washington, DC, 1995, p. 583.
[3] A. Berman, L. Addadi, A. Kvick, L. Leiserowitz, M. Nelson, S. Weiner, Intercalation of sea-urchin proteins in calcite—study of a crystalline composite-material, Science 250 (1990) 664–667.
[4] A. Berman, L. Addadi, S. Weiner, Interactions of sea-urchin skeleton macromolecules with growing calcite crystals—a study of intracrystalline proteins, Nature 331 (1988) 546–548.
[5] I. Weissbuch, L. Addadi, M. Lahav, L. Leiserowitz, Molecular recognition at crystal interfaces, Science 253 (1991) 637–645.
[6] B.R. Heywood, S. Mann, Molecular construction of oriented inorganic materials—controlled nucleation of calcite and aragonite under compressed Langmuir monolayers, Chemistry of Materials 6 (1994) 311–318.
[7] Q.L. Feng, G. Pu, Y. Pei, F.Z. Cui, H.D. Li, T.N. Kim, Polymorph and morphology of calcium carbonate crystals induced by proteins extracted from mollusk shell, Journal of Crystal Growth 216 (2000) 459–465.
[8] S. Mann, D.D. Archibald, J.M. Didymus, T. Douglas, B.R. Heywood, F.C. Meldrum, N.J. Reeves, Crystallization at inorganic–organic interfaces—biominerals and biomimetic synthesis, Science 261 (1993) 1286–1292.
[9] L. Addadi, S. Weiner, Control and design principles in biological mineralization, Angewandte Chemie—International Edition in English 31 (1992) 153–169.
[10] A. Berman, J. Hanson, L. Leiserowitz, T.F. Koetzle, S. Weiner, L. Addadi, Biological-control of crystal texture—a widespread strategy for adapting crystal properties to function, Science 259 (1993) 776–779.
[11] R.K. Tang, C.A. Orme, G.H. Nancollas, A new understanding of demineralization: the dynamics of brushite dissolution, Journal of Physical Chemistry B 107 (2003) 10653–10657.
[12] R.K. Tang, G.H. Nancollas, C.A. Orme, Mechanism of dissolution of sparingly soluble electrolytes, Journal of the American Chemical Society 123 (2001) 5437–5443.
[13] C.R. Usher, A.E. Michel, V.H. Grassian, Reactions on mineral dust, Chemical Reviews 103 (2003) 4883–4939.
[14] H.A. Al-Abadleh, V.H. Grassian, Oxide surfaces as environmental interfaces, Surface Science Reports 52 (2003) 63–161.
[15] M.L. Brusseau, Transport of reactive contaminants in heterogeneous porous-media, Reviews of Geophysics 32 (1994) 285–313.
[16] J.P. Richardson, J.W. Nicklow, In situ permeable reactive barriers for groundwater contamination, Soil & Sediment Contamination 11 (2002) 241–268.
[17] R.M. Powell, R.W. Puls, Proton generation by dissolution of intrinsic or augmented aluminosilicate minerals for in situ contaminant remediation by zero valence state iron, Environmental Science & Technology 31 (1997) 2244–2251.
[18] E. Vlieg, Understanding crystal growth in vacuum and beyond, Surface Science 500 (2002) 458–474.
[19] E. Vlieg, M. Lohmeier, H.A. Vandervegt, Surface X-ray crystallography of growing crystals and interfaces, Nuclear Instruments & Methods in Physics Research Section B—Beam Interactions with Materials and Atoms 97 (1995) 358–363.
[20] A.J. Malkin, T.A. Land, Y.G. Kuznetsov, A. Mcpherson, J.J. DeYoreo, Investigation of virus crystal-growth mechanisms by in-situ atomic-force microscopy, Physical Review Letters 75 (1995) 2778–2781.

[21] T.A. Land, A.J. Malkin, Y.G. Kuznetsov, A. Mcpherson, J.J. DeYoreo, Mechanisms of protein crystal-growth—an atomic-force microscopy study of canavalin crystallization, Physical Review Letters 75 (1995) 2774–2777.
[22] A.J. Malkin, Y.G. Kuznetsov, T.A. Land, J.J. DeYoreo, A. Mcpherson, Mechanisms of growth for protein and virus crystals, Nature Structural Biology 2 (1995) 956–959.
[23] S.D. Durbin, G. Feher, Protein crystallization, Annual Review of Physical Chemistry 47 (1996) 171–204.
[24] X.Y. Liu, E.S. Boek, W.J. Briels, P. Bennema, Prediction of crystal growth morphology based on structural analysis of the solid–fluid interface, Nature 374 (1995) 342–345.
[25] K. Sangwal, Effects of impurities on crystal growth processes, Progress in Crystal Growth and Characterization of Materials 32 (1996) 3–43.
[26] P.M. Dove, M.F. Hochella, Calcite precipitation mechanisms and inhibition by orthophosphate—in situ observations by scanning force microscopy, Geochimica et Cosmochimica Acta 57 (1993) 705–714.
[27] H.H. Teng, P.M. Dove, C.A. Orme, J.J. De Yoreo, Thermodynamics of calcite growth: baseline for understanding biomineral formation, Science 282 (1998) 724–727.
[28] K.S. Wang, R. Resch, B.E. Koel, P.J. Shuler, Y.C. Tang, H.J. Chen, T.F. Yen, Study of the dissolution of the barium sulfate (0 0 1) surface with hydrochloric acid by atomic force microscopy, Journal of Colloid and Interface Science 219 (1999) 212–215.
[29] E.J. Elzinga, R.J. Reeder, X-ray absorption spectroscopy study of Cu^{2+} and Zn^{2+} adsorption complexes at the calcite surface: implications for site-specific metal incorporation preferences during calcite crystal growth, Geochimica et Cosmochimica Acta 66 (2002) 3943–3954.
[30] Y.L. Qian, N.C. Sturchio, R.P. Chiarello, P.F. Lyman, T.L. Lee, M.J. Bedzyk, Lattice location of trace-elements within minerals and at their surfaces with X-ray standing waves, Science 265 (1994) 1555–1557.
[31] N.C. Sturchio, M.R. Antonio, L. Soderholm, S.R. Sutton, J.C. Brannon, Tetravalent uranium in calcite, Science 281 (1998) 971–973.
[32] V.I. Parvulescu, P. Grange, B. Delmon, Catalytic removal of NO, Catalysis Today 46 (1998) 233–316.
[33] D.P. Woodruff, T.A. Delchar, Modern Techniques of Surface Science, Cambridge University Press, Cambridge, New York, 1994, p. xviii, 586 p.
[34] G. Binnig, H. Rohrer, Scanning tunneling microscopy—from birth to adolescence, Reviews of Modern Physics 59 (1987) 615–625.
[35] G. Binnig, C.F. Quate, C. Gerber, Atomic force microscope, Physical Review Letters 56 (1986) 930–933.
[36] G.E. Brown, G. Calas, G.A. Waychunas, J. Petiau, X-ray absorption-spectroscopy and its applications in mineralogy and geochemistry, Reviews in Mineralogy 18 (1988) 432–512.
[37] G.E. Brown, G.A. Parks, Synchrotron-based X-ray absorption studies of cation environments in earth materials, Reviews of Geophysics 27 (1989) 519–533.
[38] G.E. Brown, G.A. Parks, Sorption of trace elements on mineral surfaces: modern perspectives from spectroscopic studies, and comments on sorption in the marine environment, International Geology Review 43 (2001) 963–1073.
[39] M.J. Bedzyk, L.W. Cheng, X-ray standing wave studies of minerals and mineral surfaces: principles and applications, Applications of Synchrotron Radiation in Low-Temperature Geochemistry and Environmental Sciences, Reviews in Mineralogy and Geochemistry vol. 49 (2002) 221–266.
[40] P.A. Fenter, in: P. Fenter, M. Rivers, N.C. Sturchio, S.R. Sutton (Eds.), Applications of Synchrotron Radiation in Low-Temperature Geochemistry and Environmental Sciences, Reviews in Mineralogy and Geochemistry vol. 49 (2002) 149–220.
[41] R. Feidenhansl, Surface-structure determination by X-ray-diffraction, Surface Science Reports 10 (1989) 105–188.
[42] I.K. Robinson, D.J. Tweet, Surface X-ray-diffraction, Reports on Progress in Physics 55 (1992) 599–651.
[43] D.P. Woodruff, The Solid–Liquid Interface, Cambridge University Press, London, 1973, p. 182.

[44] A.A. Gewirth, H. Siegenthaler, Nanoscale Probes of the Solid/Liquid Interface, Kluwer Academic Publishers, Boston, 1995, p. xv, 334 p.
[45] M.F. Hochella, A.F. White (Eds.), Mineral–Water Interface Geochemistry, vol. 23, Mineralogical Society of America, Washington, DC, 1990.
[46] W. Stumm, L. Sigg, B. Sulzberger, Chemistry of the Solid–Water Interface: Processes at the Mineral–Water and Particle–Water Interface in Natural Systems, Wiley, New York, 1992, p. x, 428 p.
[47] G.E. Brown, V.E. Henrich, W.H. Casey, D.L. Clark, C. Eggleston, A. Felmy, D.W. Goodman, M. Gratzel, G. Maciel, M.I. McCarthy, K.H. Nealson, D.A. Sverjensky, M.F. Toney, J.M. Zachara, Metal oxide surfaces and their interactions with aqueous solutions and microbial organisms, Chemical Reviews 99 (1999) 77–174.
[48] S. Mann, J. Webb, R.J.P. Williams, Biomineralization: Chemical and Biochemical Perspectives, VCH, New York, NY, USA, 1989, p. xxiv, 541 p.
[49] P.V. Brady, Physics and Chemistry of Mineral Surfaces, CRC Press, Boca Raton, FL, 1996, p. 268.
[50] D.J. Vaughan, Mineral Surfaces, Chapman & Hall, New York, 1994.
[51] R.T. Cygan, J.D. Kubicki, Mineralogical Society of America, Molecular Modeling Theory: Applications in the Geosciences, Mineralogical Society of America, Washington, DC, 2001, p. xii, 531 p.
[52] G.E. Brown, How minerals react with water, Science 294 (2001) 67–70.
[53] F.F. Abraham, The interfacial density profile of a Lennard–Jones fluid in contact with a (1 0 0) Lennard–Jones wall and its relationship to idealized fluid-wall systems: a Monte-Carlo simulation, Journal of Chemical Physics 68 (1978) 3713–3716.
[54] W.A. Curtin, Density-functional theory of the solid–liquid interface, Physical Review Letters 59 (1987) 1228–1231.
[55] F. Spaepen, Structural model for the solid–liquid interface in monoatomic systems, Acta Mettallurgica 23 (1975) 729–743.
[56] D.T. Richens, The Chemistry of Aqua-Ions, John Wiley & Sons, Chichester, 1997.
[57] C.H. Bridgeman, N.T. Skipper, A Monte Carlo study of water at an uncharged clay surface, Journal of Physics—Condensed Matter 9 (1997) 4081–4087.
[58] C.H. Bridgeman, A.D. Buckingham, N.T. Skipper, M.C. Payne, Ab-initio total energy study of uncharged 2:1 clays and their interaction with water, Molecular Physics 89 (1996) 879–888.
[59] E. Stockelmann, R. Hentschke, A molecular-dynamics simulation study of water on NaCl(1 0 0) using a polarizable water model, Journal of Chemical Physics 110 (1999) 12097–12107.
[60] I.C. Yeh, M.L. Berkowitz, Structure and dynamics of water at water vertical bar Pt interface as seen by molecular dynamics computer simulation, Journal of Electroanalytical Chemistry 450 (1998) 313–325.
[61] I.C. Yeh, M.L. Berkowitz, Aqueous solution near charged Ag(1 1 1) surfaces: comparison between a computer simulation and experiment, Chemical Physics Letters 301 (1999) 81–86.
[62] R. Akiyama, F. Hirata, Theoretical study for water structure at highly ordered surface: effect of surface structure, Journal of Chemical Physics 108 (1998) 4904–4911.
[63] X.F. Xia, L. Perera, U. Essmann, M.L. Berkowitz, The structure of water at platinum/water interfaces—molecular-dynamics computer-simulations, Surface Science 335 (1995) 401–415.
[64] M. Vossen, F. Forstmann, The structure of water at a planar wall—an integral-equation approach with the central force model, Journal of Chemical Physics 101 (1994) 2379–2390.
[65] S.H. Lee, P.J. Rossky, A comparison of the structure and dynamics of liquid water at hydrophobic and hydrophilic surfaces—a molecular-dynamics simulation study, Journal of Chemical Physics 100 (1994) 3334–3345.
[66] A. Delville, S. Sokolowski, Adsorption of vapor at a solid interface—a molecular-model of clay wetting, Journal of Physical Chemistry 97 (1993) 6261–6271.
[67] A. Delville, Structure and properties of confined liquids—a molecular-model of the clay water interface, Journal of Physical Chemistry 97 (1993) 9703–9712.
[68] E. Spohr, Computer-simulation of the water platinum interface, Journal of Physical Chemistry 93 (1989) 6171–6180.

[69] R.M. Pashley, J.N. Israelachvili, Molecular layering of water in thin films between mica surfaces and its relation to hydration forces, Journal of Colloid and Interface Science 101 (1984) 511–523.
[70] J.N. Israelachvili, R.M. Pashley, Molecular layering of water at surfaces and origin of repulsive hydration forces, Nature 306 (1983) 249–250.
[71] J.N. Israelachvili, H. Wennerstrom, Role of hydration and water structure in biological and colloidal interactions, Nature 379 (1996) 219–225.
[72] U. Raviv, J. Klein, Fluidity of bound hydration layers, Science 297 (2002) 1540–1543.
[73] Y.X. Zhu, S. Granick, Viscosity of interfacial water, Physical Review Letters 87 (2001) 096104.
[74] J.P. Cleveland, T.E. Schaffer, P.K. Hansma, Probing oscillatory hydration potentials using thermal-mechanical noise in an atomic-force microscope, Physical Review B 52 (1995) R8692–R8695.
[75] M. Hugelmann, W. Schindler, Tunnel barrier height oscillations at the solid/liquid interface, Surface Science 541 (2003) L643–L648.
[76] X.Y. Zhang, Y.X. Zhu, S. Granick, Hydrophobicity at a Janus interface, Science 295 (2002) 663–666.
[77] P.G. de Gennes, Anomalous friction at a 'Janus interface': the possible role of blisters, Advances in Colloid and Interface Science 100 (2003) 129–135.
[78] S. Karaborni, B. Smit, W. Heidug, J. Urai, E. van Oort, The swelling of clays: molecular simulations of the hydration of montmorillonite, Science 271 (1996) 1102–1104.
[79] N.T. Skipper, A.K. Soper, J.D.C. McConnell, The structure of interlayer water in vermiculite, Journal of Chemical Physics 94 (1991) 5751–5760.
[80] G. Sposito, N.T. Skipper, R. Sutton, S.H. Park, A.K. Soper, J.A. Greathouse, Surface geochemistry of the clay minerals, Proceedings of the National Academy of Sciences of the United States of America 96 (1999) 3358–3364.
[81] N.T. Skipper, G.D. Williams, A.V.C. de Siqueira, C. Lobban, A.K. Soper, Time-of-flight neutron diffraction studies of clay–fluid interactions under basin conditions, Clay Minerals 35 (2000) 283–290.
[82] W.J. Huisman, J.F. Peters, M.J. Zwanenburg, S.A. deVries, T.E. Derry, D. Abernathy, J.F. van der Veen, Layering of a liquid metal in contact with a hard wall, Nature 390 (1997) 379–381.
[83] C.J. Yu, A.G. Richter, J. Kmetko, A. Datta, P. Dutta, X-ray diffraction evidence of ordering in a normal liquid near the solid–liquid interface, Europhysics Letters 50 (2000) 487–493.
[84] C.J. Yu, A.G. Richter, A. Datta, M.K. Durbin, P. Dutta, Observation of molecular layering in thin liquid films using X-ray reflectivity, Physical Review Letters 82 (1999) 2326–2329.
[85] A.K. Doerr, M. Tolan, J.P. Schlomka, W. Press, Evidence for density anomalies of liquids at the solid/liquid interface, Europhysics Letters 52 (2000) 330–336.
[86] C.J. Yu, G. Evmenenko, J. Kmetko, P. Dutta, Effects of shear flow on interfacial ordering in liquids: X-ray scattering studies, Langmuir 19 (2003) 9558–9561.
[87] H. Reichert, O. Klein, H. Dosch, M. Denk, V. Honklmaki, T. Lippmann, G. Reiter, Observation of five-fold local symmetry in liquid lead, Nature 408 (2000) 839–841.
[88] O.H. Seeck, H. Kim, D.R. Lee, D. Shu, I.D. Kaendler, J.K. Basu, S.K. Sinha, Observation of thickness quantization in liquid films confined to molecular dimension, Europhysics Letters 60 (2002) 376–382.
[89] M.J. Zwanenburg, J.H.H. Bongaerts, J.F. Peters, D.O. Riese, J.F. van der Veen, X-ray waveguiding studies of ordering phenomena in confined fluids, Physical Review Letters 85 (2000) 5154–5157.
[90] S.E. Donnelly, R.C. Birtcher, C.W. Allen, I. Morrison, K. Furuya, M.H. Song, K. Mitsuishi, U. Dahmen, Ordering in a fluid inert gas confined by flat surfaces, Science 296 (2002) 507–510.
[91] M.F. Toney, J.N. Howard, J. Richer, G.L. Borges, J.G. Gordon, O.R. Melroy, D.G. Wiesler, D. Yee, L.B. Sorensen, Voltage-dependent ordering of water-molecules at an electrode–electrolyte interface, Nature 368 (1994) 444–446.
[92] M.F. Toney, J.N. Howard, J. Richer, G.L. Borges, J.G. Gordon, O.R. Melroy, D.G. Wiesler, D. Yee, L.B. Sorensen, Distribution of water-molecules at Ag(1 1 1)/electrolyte interface as studied with surface X-ray-scattering, Surface Science 335 (1995) 326–332.
[93] Y.S. Chu, T.E. Lister, W.G. Cullen, H. You, Z. Nagy, Commensurate water monolayer at the RuO_2 (1 1 0)/water interface, Physical Review Letters 86 (2001) 3364–3367.

[94] J. Wang, B.M. Ocko, A.J. Davenport, H.S. Isaacs, Insitu X-ray-diffraction and X-ray-reflectivity studies of the Au(1 1 1) electrolyte interface—reconstruction and anion adsorption, Physical Review B 46 (1992) 10321–10338.
[95] F. Morel, Principles of Aquatic Chemistry, John Wiley, New York, 1983, p. ix, 446 p.
[96] W. Stumm, Aquatic Surface Chemistry: Chemical Processes at the Particle–Water Interface, Wiley, New York, 1987, p. xix, 520 p.
[97] G. Sposito, The Surface Chemistry of Soils, Oxford University Press, New York, 1984, p. xii, 234 p.
[98] J. Westall, H. Hohl, A comparison of electrostatic models for the oxide solution interface, Advances in Colloid and Interface Science 12 (1980) 265–294.
[99] H.A. Al-Abadleh, V.H. Grassian, FT-IR study of water adsorption on aluminum oxide surfaces, Langmuir 19 (2003) 341–347.
[100] P. Liu, T. Kendelewicz, G.E. Brown, Reaction of water with MgO(1 0 0) surfaces. Part II: Synchrotron photoemission studies of defective surfaces, Surface Science 413 (1998) 315–332.
[101] P. Liu, T. Kendelewicz, G.E. Brown, E.J. Nelson, S.A. Chambers, Reaction of water vapor with α-Al_2O_3(0 0 0 1) and α-Fe_2O_3(0 0 0 1) surfaces: synchrotron X-ray photoemission studies and thermodynamic calculations, Surface Science 417 (1998) 53–65.
[102] T. Kendelewicz, P. Liu, C.S. Doyle, G.E. Brown, E.J. Nelson, S.A. Chambers, Reaction of water with the (1 0 0) and (1 1 1) surfaces of Fe_3O_4, Surface Science 453 (2000) 32–46.
[103] M.A. Blesa, A.D. Weisz, P.J. Morando, J.A. Salfity, G.E. Magaz, A.E. Regazzoni, The interaction of metal oxide surfaces with complexing agents dissolved in water, Coordination Chemistry Reviews 196 (2000) 31–63.
[104] S. Garoff, E.B. Sirota, S.K. Sinha, H.B. Stanley, The effects of substrate roughness on ultrathin water films, Journal of Chemical Physics 90 (1989) 7505–7515.
[105] J.R. Lu, R.K. Thomas, Neutron reflection from wet interfaces, Journal of the Chemical Society—Faraday Transactions 94 (1998) 995–1018.
[106] D. Schwendel, T. Hayashi, R. Dahint, A. Pertsin, M. Grunze, R. Steitz, F. Schreiber, Interaction of water with self-assembled monolayers: neutron reflectivity measurements of the water density in the interface region, Langmuir 19 (2003) 2284–2293.
[107] S.W. Ong, X.L. Zhao, K.B. Eisenthal, Polarization of water-molecules at a charged interface—2nd harmonic studies of the silica water interface, Chemical Physics Letters 191 (1992) 327–335.
[108] Q. Du, R. Superfine, E. Freysz, Y.R. Shen, Vibrational spectroscopy of water at the vapor water interface, Physical Review Letters 70 (1993) 2313–2316.
[109] Q. Du, E. Freysz, Y.R. Shen, Vibrational-spectra of water-molecules at quartz water interfaces, Physical Review Letters 72 (1994) 238–241.
[110] Q. Du, E. Freysz, Y.R. Shen, Surface vibrational spectroscopic studies of hydrogen-bonding and hydrophobicity, Science 264 (1994) 826–828.
[111] M.S. Yeganeh, S.M. Dougal, H.S. Pink, Vibrational spectroscopy of water at liquid/solid interfaces: crossing the isoelectric point of a solid surface, Physical Review Letters 83 (1999) 1179–1182.
[112] V. Ostroverkhov, G.A. Waychunas, Y.R. Shen, Vibrational spectra of water at water/alpha-quartz (0 0 0 1) interface, Chemical Physics Letters 386 (2004) 144–148.
[113] Z. Nagy, H. You, Applications of surface X-ray scattering to electrochemistry problems, Electrochimica Acta 47 (2002) 3037–3055.
[114] N.M. Markovic, P.N. Ross, Surface science studies of model fuel cell electrocatalysts, Surface Science Reports 45 (2002) 121–229.
[115] H.D. Abruna, J.H. White, M.J. Albarelli, G.M. Bommarito, M.J. Bedzyk, M. Mcmillan, Is there any beam yet—uses of synchrotron radiation in the in situ study of electrochemical interfaces, Journal of Physical Chemistry 92 (1988) 7045–7052.
[116] H. You, Z. Nagy, Applications of synchrotron surface X-ray scattering studies of electrochemical interfaces, MRS Bulletin 24 (1999) 36–40.
[117] C.A. Melendres, A. Tadjeddine, Synchrotron Techniques in Interfacial Electrochemistry, Kluwer Academic, Dordrecht, 1994, p. xviii, 479 p.
[118] E. Vlieg, in: X.Y. Liu, J.J. De Yoreo (Eds.), Nanoscale Structure and Assembly at Solid–Fluid Interfaces, vol. 1, Kluwer, Dordrecht, The Netherlands, 2004.

[119] M.A. Henderson, The interaction of water with solid surfaces: fundamental aspects revisited, Surface Science Reports 46 (2002) 5–308.
[120] P.A. Thiel, T.E. Madey, The interaction of water with solid–surfaces—fundamental-aspects, Surface Science Reports 7 (1987) 211–385.
[121] L.J. Michot, F. Villieras, M. Francois, I. Bihannic, M. Pelletier, J.M. Cases, Water organisation at the solid–aqueous solution interface, Comptes Rendus Geoscience 334 (2002) 611–631.
[122] A.L. Summer, E.J. Menke, Y. Dubowski, J.T. Newberg, R.M. Penner, J.C. Hemminger, L.M. Wingen, T. Brauers, B.J. Finlayson-Pitts, The nature of water on surfaces of laboratory systems and implications for heterogeneous chemistry in the troposphere, Physical Chemistry Chemical Physics 6 (2004) 604–613.
[123] G.L. Richmond, Molecular bonding and interactions at aqueous surfaces as probed by vibrational sum frequency spectroscopy, Chemical Reviews 102 (2002) 2693–2724.
[124] L.R. Pratt, A. Pohorille, Hydrophobic effects and modeling of biophysical aqueous solution interfaces, Chemical Reviews 102 (2002) 2671–2691.
[125] V.E. Henrich, P.A. Cox, The Surface Science of Metal Oxides, Cambridge University Press, Cambridge; New York, 1994, p. xiv, 464 p.
[126] G. Renaud, Oxide surfaces and metal/oxide interfaces studied by grazing incidence X-ray scattering, Surface Science Reports 32 (1998) 5–90.
[127] U. Diebold, The surface science of titanium dioxide, Surface Science Reports 48 (2003) 53–229.
[128] C.B. Duke (Ed.), Surface Science, The First Thirty Years, New Holland, Amsterdam, 1994, pp. 1–1054.
[129] G. Charlton, P.B. Howes, C.L. Nicklin, P. Steadman, J.S.G. Taylor, C.A. Muryn, S.P. Harte, J. Mercer, R. McGrath, D. Norman, T.S. Turner, G. Thornton, Relaxation of $TiO_2(1\,1\,0)$-(1×1) using surface X-ray diffraction, Physical Review Letters 78 (1997) 495–498.
[130] C. Zhang, P.J.D. Lindan, Towards a first-principles picture of the oxide–water interface, Journal of Chemical Physics 119 (2003) 9183–9190.
[131] C. Zhang, P.J.D. Lindan, Multilayer water adsorption on rutile $TiO_2(1\,1\,0)$: a first-principles study, Journal of Chemical Physics 118 (2003) 4620–4630.
[132] P.J.D. Lindan, N.M. Harrison, J.M. Holender, M.J. Gillan, First-principles molecular dynamics simulation of water dissociation on $TiO_2(1\,1\,0)$, Chemical Physics Letters 261 (1996) 246–252.
[133] M. Odelius, M. Bernasconi, M. Parrinello, Two dimensional ice adsorbed on mica surface, Physical Review Letters 78 (1997) 2855–2858.
[134] A. Stirling, M. Bernasconi, M. Parrinello, Ab initio simulation of water interaction with the $(1\,0\,0)$ surface of pyrite, Journal of Chemical Physics 118 (2003) 8917–8926.
[135] R. Car, M. Parrinello, Structural, dynamical and electronic-properties of amorphous-silicon—an ab initio molecular dynamics study, Physical Review Letters 60 (1988) 204–207.
[136] M. Allesch, E. Schwegler, F. Gygi, G. Galli, A first principles simulation of rigid water, Journal of Chemical Physics 120 (2004) 5192–5198.
[137] M. Krack, A. Gambirasio, M. Parrinello, Ab initio X-ray scattering of liquid water, Journal of Chemical Physics 117 (2002) 9409–9412.
[138] A. Tilocca, A. Selloni, Structure and reactivity of water layers on defect-free and defective anatase $TiO_2(1\,0\,1)$ surfaces, Journal of Physical Chemistry B 108 (2004) 4743–4751.
[139] E. Spohr, Some recent trends in computer simulations of aqueous double layers, Electrochimica Acta 49 (2003) 23–27.
[140] W. Langel, Car–Parrinello simulation of H_2O dissociation on rutile, Surface Science 496 (2002) 141–150.
[141] S. Izvekov, G.A. Voth, Ab initio molecular dynamics simulation of the $Ag(1\,1\,1)$–water interface, Journal of Chemical Physics 115 (2001) 7196–7206.
[142] L. Pauling, Principles determining the structure of complex ionic solids, Journal of the American Chemical Society 51 (1929) 1010–1026.
[143] I.D. Brown, The Chemical Bond in Inorganic Chemistry, The Bond Valence Model, Oxford Scientific Publications, 2002.

[144] I.D. Brown, Recent developments in the bond valence model of inorganic bonding, Physics and Chemistry of Minerals 15 (1987) 30–34.
[145] I.D. Brown, The bond valence model as a tool for teaching inorganic chemistry: the ionic model revisited, Journal of Chemical Education 77 (2000) 1070–1075.
[146] R. Rossano, F. Farges, A. Ramos, J.M. Delaye, G.E. Brown, Bond valence in silicate glasses, Journal of Non-Crystalline Solids 304 (2002) 167–173.
[147] P.J. Eng, T.P. Trainor, G.E. Brown, G.A. Waychunas, M. Newville, S.R. Sutton, M.L. Rivers, Structure of the hydrated α-Al_2O_3 (0001) surface, Science 288 (2000) 1029–1033.
[148] G.A. Parks, P.L. DeBruyn, The zero point of charge of oxides, Journal of Physical Chemistry 66 (1962) 967–973.
[149] P.W. Schindler, W. Stumm, in: W. Stumm (Ed.), Aquatic Surface Chemistry, Wiley-Interscience, New York, 1987, pp. 83–110.
[150] J.A. Davis, D.B. Kent, Surface complexation modeling in aqueous geochemistry, Reviews in Mineralogy 23 (1990) 177–260.
[151] D.A. Dzombak, F.M.M. Morel, Surface Complexation Modeling: Hydrous Ferric Oxide, Wiley, New York, 1990, p. xvii, 393 p.
[152] T. Hiemstra, W.H. Vanriemsdijk, G.H. Bolt, Multisite proton adsorption modeling at the solid–solution interface of (hydr)oxides—a new approach. 1. Model description and evaluation of intrinsic reaction constants, Journal of Colloid and Interface Science 133 (1989) 91–104.
[153] M.L. Machesky, D.J. Wesolowski, D.A. Palmer, M.K. Ridley, On the temperature dependence of intrinsic surface protonation equilibrium constants: an extension of the revised MUSIC model, Journal of Colloid and Interface Science 239 (2001) 314–327.
[154] D.A. Sverjensky, Interpretation and prediction of triple-layer model capacitances and the structure of the oxide–electrolyte–water interface, Geochimica et Cosmochimica Acta 65 (2001) 3643–3655.
[155] D.A. Sverjensky, Physical surface-complexation models for sorption at the mineral–water interface, Nature 364 (1993) 776–780.
[156] D.A. Sverjensky, N. Sahai, Theoretical prediction of single-site surface-protonation equilibrium constants for oxides and silicates in water, Geochimica et Cosmochimica Acta 60 (1996) 3773–3797.
[157] J. Lyklema, Fundamentals of Interface and Colloid Science, Academic Press, New York, 1995.
[158] T. Hiemstra, W.H. Van Riemsdijk, in: A.T. Hubbard (Ed.), Encyclopedia of Colloid and Interface Science, Marcel Dekker, New York, 2002, pp. 3773–3799.
[159] F. Franks, Water, A Comprehensive Treatise, Plenum Publishing, New York, 1982, p. 484.
[160] A.K. Soper, The radial distribution functions of water and ice from 220 to 673 K and at pressures up to 400 MPa, Chemical Physics 258 (2000) 121–137.
[161] T. Head-Gordon, G. Hura, Water structure from scattering experiments and simulation, Chemical Reviews 102 (2002) 2651–2669.
[162] M.C.R. Symons, Structure of liquid water, Nature 239 (1972) 257–259.
[163] K. Lonsdale, Structure of ice, Proceedings of the Royal Society (London) A 247 (1958) 424–434.
[164] G. Hura, J.M. Sorenson, R.M. Glaeser, T. Head-Gordon, A high-quality X-ray scattering experiment on liquid water at ambient conditions, Journal of Chemical Physics 113 (2000) 9140–9148.
[165] J.M. Sorenson, G. Hura, R.M. Glaeser, T. Head-Gordon, What can X-ray scattering tell us about the radial distribution functions of water?, Journal of Chemical Physics 113 (2000) 9149–9161.
[166] Y.L. Xie, K.F. Ludwig, G. Morales, D.E. Hare, C.M. Sorensen, Noncritical behavior of density-fluctuations in supercooled water, Physical Review Letters 71 (1993) 2050–2053.
[167] P. Wernet, D. Nordlund, U. Bergmann, M. Cavalleri, M. Odelius, H. Ogasawara, L.A. Naslund, T.K. Hirsch, L. Ojamae, P. Glatzel, L.G.M. Pettersson, A. Nilsson, The structure of the first coordination shell in liquid water, Science 304 (2004) 995–999.
[168] U. Bergmann, P. Wernet, P. Glatzel, M. Cavalleri, L.G.M. Pettersson, A. Nilsson, S.P. Cramer, X-ray Raman spectroscopy at the oxygen K edge of water and ice: implications on local structure models, Physical Review B 66 (2002) 092107.
[169] E.D. Isaacs, A. Shukla, P.M. Platzman, D.R. Hamann, B. Barbiellini, C.A. Tulk, Covalency of the hydrogen bond in ice: a direct X-ray measurement, Physical Review Letters 82 (1999) 600–603.

[170] E.D. Isaacs, A. Shukla, P.M. Platzman, D.R. Hamann, B. Barbiellini, C.A. Tulk, Compton scattering evidence for covalency of the hydrogen bond in ice, Journal of Physics and Chemistry of Solids 61 (2000) 403–406.
[171] B.E. Warren, X-ray Diffraction, Dover, Mineola, 1990.
[172] J. Als-Nielsen, D. McMorrow, Elements of Modern X-ray Physics, John Wiley and Sons, Chichester, 2001.
[173] P. Eisenberger, W.C. Marra, X-ray diffraction study of the Ge(0 0 1) reconstructed surface, Physical Review Letters 46 (1981) 1081–1084.
[174] L.G. Parratt, Surface studies of solids by total reflection X-rays, Physical Review 95 (1954) 359–369.
[175] S.R. Andrews, R.A. Cowley, Scattering of X-rays from crystal surfaces, Journal of Physics C: Solid State Physics 18 (1985) 6427–7439.
[176] I.K. Robinson, Crystal truncation rods and surface-roughness, Physical Review B 33 (1986) 3830–3836.
[177] J. Als-Nielsen, Solid and liquid interfaces studied by synchrotron X-ray diffraction, Topics in Current Physics 43 (1987) 181–222.
[178] J. Als-Nielsen, Synchrotron X-ray studies of liquid–vapor interfaces, Physica A 140 (1986) 376–389.
[179] J. Als-Nielsen, H. Mohwald, in: S. Ebashi, M. Koch, E. Rubenstein (Eds.), Handbook on Synchrotron Radiation, vol. 4, North Holland, New York, 1991, pp. 1–53.
[180] I.K. Robinson, in: G.S. Brown, D.E. Moncton (Eds.), Handbook on Synchrotron Radiation, vol. 3, North Holland, New York, 1991, pp. 223–266.
[181] I.M. Tidswell, B.M. Ocko, P.S. Pershan, S.R. Wasserman, G.M. Whitesides, J.D. Axe, X-ray specular reflection studies of silicon coated by organic monolayers (alkylsiloxanes), Physical Review B 41 (1990) 1111–1128.
[182] B.W. Batterman, Detection of foreign atoms sites by their X-ray fluorescence scattering, Physical Review Letters 22 (1969) 703–705.
[183] B.W. Batterman, H. Cole, Dynamical diffraction of X-rays by perfect crystals, Reviews on Modern Physics 36 (1964) 681–787.
[184] P.L. Cowan, J.A. Golovchenko, M.F. Robbins, X-ray standing waves at crystal surfaces, Physical Review Letters 44 (1980) 1680–1683.
[185] D.P. Woodruff, D.L. Seymour, C.F. Mcconville, C.E. Riley, M.D. Crapper, N.P. Prince, Simple X-ray standing-wave technique and its application to the investigation of the Cu(1 1 1) $(\sqrt{3}\times\sqrt{3})$R30°-Cl structure, Physical Review Letters 58 (1987) 1460–1462.
[186] M.J. Bedzyk, D.H. Bilderback, G.M. Bommarito, M. Caffrey, J.S. Schildkraut, X-ray standing waves—a molecular yardstick for biological-membranes, Science 241 (1988) 1788–1791.
[187] M.J. Bedzyk, G.M. Bommarito, M. Caffrey, T.L. Penner, Diffuse-double layer at a membrane-aqueous interface measured with X-ray standing waves, Science 248 (1990) 52–56.
[188] J. Wang, M.J. Bedzyk, T.L. Penner, M. Caffrey, Structural studies of membranes and surface-layers up to 1,000 a thick using X-ray standing waves, Nature 354 (1991) 377–380.
[189] I.K. Robinson, W.K. Waskiewicz, P.H. Fuoss, J.B. Stark, P.A. Bennett, X-ray-diffraction evidence of adatoms in the Si(1 1 1)7×7 reconstructed surface, Physical Review B 33 (1986) 7013–7016.
[190] S.G.J. Mochrie, D.M. Zehner, B.M. Ocko, D. Gibbs, Structure and phases of the Au(0 0 1) surface—X-ray-scattering measurements, Physical Review Letters 64 (1990) 2925–2928.
[191] K.G. Huang, D. Gibbs, D.M. Zehner, A.R. Sandy, S.G.J. Mochrie, Phase-behavior of the Au(1 1 1) surface—discommensurations and kinks, Physical Review Letters 65 (1990) 3313–3316.
[192] D. Gibbs, G. Grubel, D.M. Zehner, D.L. Abernathy, S.G.J. Mochrie, Orientational epitaxy of the hexagonally reconstructed Pt(0 0 1) surface, Physical Review Letters 67 (1991) 3117–3120.
[193] D. Gibbs, B.M. Ocko, D.M. Zehner, S.G.J. Mochrie, Absolute X-ray reflectivity study of the Au(1 0 0) surface, Physical Review B 38 (1988) 7303–7310.
[194] M.G. Samant, M.F. Toney, G.L. Borges, L. Blum, O.R. Melroy, Grazing-incidence X-ray-diffraction of lead monolayers at a silver (1 1 1) and gold (1 1 1) electrode–electrolyte interface, Journal of Physical Chemistry 92 (1988) 220–225.
[195] H. You, Y.S. Chu, T.E. Lister, Z. Nagy, A.L. Ankudiniv, J.J. Rehr, Resonance X-ray scattering from Pt(1 1 1) surfaces under water, Physica B 283 (2000) 212–216.

[196] W.R. Busing, H.A. Levy, Angle calculations for 3- and 4-circle X-ray and neutron diffractometers, Acta Crystallographica 22 (1967) 457–464.
[197] S.G.J. Mochrie, Four-circle angle calculations for surface diffraction, Journal of Applied Crystallography 21 (1988) 1–3.
[198] E. Vlieg, J.F. van der Veen, J.E. Macdonald, M. Miller, Angle calculations for a five-circle diffractometer used for surface X-ray diffraction, Journal of Applied Crystallography 20 (1987) 330–337.
[199] J.M. Bloch, Angle and index calculations for a *z*-axis X-ray diffractometer, Journal of Applied Crystallography 18 (1985) 33–36.
[200] M. Lohmeier, E. Vlieg, Angle calculations for a six-circle X-ray diffractometer, Journal of Applied Crystallography 26 (1993) 706–716.
[201] I.K. Robinson, H. Graafsma, A. Kvick, J. Linderholm, First testing of the fast kappa diffractometers at National Synchrotron Light Source and European Synchrotron Radiation Facility, Review of Scientific Instruments 66 (1995) 1765–1767.
[202] H. You, Angle calculations for 4S+2D six-circle diffractometer, Journal of Applied Crystallography 32 (1999) 614–623.
[203] E. Vlieg, ROD: a program for surface X-ray crystallography, Journal of Applied Crystallography 33 (2000) 401–405.
[204] O.M. Magnussen, B.M. Ocko, M.J. Regan, K. Penanen, P.S. Pershan, M. Deutsch, X-ray reflectivity measurements of surface layering in liquid mercury, Physical Review Letters 74 (1995) 4444–4447.
[205] H. You, U. Welp, G.W. Crabtree, Y. Fang, S.K. Sinha, J.D. Axe, X. Jiang, S.C. Moss, X-ray crystal-truncation-rod analysis of untwinned $YBa_2Cu_3O_7$-delta single-crystals—the growth-termination plane, Physical Review B 45 (1992) 5107–5110.
[206] I.K. Robinson, E. Vlieg, X-ray reflectivity study of the Si(1 1 1)7×7 surface, Surface Science 261 (1992) 123–128.
[207] I.K. Robinson, P. Eng, R. Schuster, Origin of the surface sensitivity in surface X-ray diffraction, Acta Physica Polonica A 86 (1994) 513–520.
[208] D. Gidalevitz, R. Feidenhansl, D.M. Smilgies, L. Leiserowitz, X-ray scattering from surfaces of organic crystals, Surface Review and Letters 4 (1997) 721–732.
[209] D. Gidalevitz, R. Feidenhansl, L. Leiserowitz, Surface X-ray scattering study of stereospecific adsorption of additives onto the surface of a molecular crystal grown from solution, Angewandte Chemie—International Edition in English 36 (1997) 959–962.
[210] S.A. de Vries, P. Goedtkindt, S.L. Bennett, W.J. Huisman, M.J. Zwanenburg, D.M. Smilgies, J.J. De Yoreo, W.J.P. van Enckevort, P. Bennema, E. Vlieg, Surface atomic structure of KDP crystals in aqueous solution: an explanation of the growth shape, Physical Review Letters 80 (1998) 2229–2232.
[211] R. Edgar, T.M. Schultz, F.B. Rasmussen, R. Feidenhans'l, L. Leiserowitz, Solvent binding to benzamide crystals: morphology, induced twinning and direct observation by surface X-ray diffraction, Journal of the American Chemical Society 121 (1999) 632–637.
[212] P. Fenter, L. Cheng, C. Park, Z. Zhang, N.C. Sturchio, Structure of the orthoclase (0 0 1)- and (0 1 0)–water interfaces by high-resolution X-ray reflectivity, Geochimica et Cosmochimica Acta 67 (2003) 4267–4275.
[213] P. Fenter, H. Teng, P. Geissbuhler, J.M. Hanchar, K.L. Nagy, N.C. Sturchio, Atomic-scale structure of the orthoclase (0 0 1)–water interface measured with high-resolution X-ray reflectivity, Geochimica et Cosmochimica Acta 64 (2000) 3663–3673.
[214] L. Cheng, P. Fenter, K.L. Nagy, M.L. Schlegel, N.C. Sturchio, Molecular-scale density oscillations in water adjacent to a mica surface, Physical Review Letters 87 (2001) 156103.
[215] M.F. Reedijk, J. Arsic, D. Kaminski, W.J.P. van Enckevort, E. Vlieg, Surface structure of potassium dichromate (KBC) crystals, Surface Science 526 (2003) 133–140.
[216] C. Park, P. Fenter, Z. Zhang, L. Cheng, N.C. Sturchio, Structure of naturally grown fluorapatite (1 0 0)–water interface by high-resolution X-ray reflectivity, American Mineralogist 89 (2004) 1647–1654.

[217] P. Fenter, C. Park, Termination interference along crystal truncation rods, Journal of Applied Crystallography 37 (6) (2004) 977–987.
[218] P. Fenter, M.T. McBride, G. Srajer, N.C. Sturchio, D. Bosbach, Structure of barite (001)- and (210)–water interfaces, Journal of Physical Chemistry B 105 (2001) 8112–8119.
[219] L. Cheng, P. Fenter, M.J. Bedzyk, N.C. Sturchio, Fourier-expansion solution of atom distributions in a crystal using X-ray standing waves, Physical Review Letters 90 (2003) 255503.
[220] R.P. Chiarello, N.C. Sturchio, The calcite (10−14) cleavage surface in water—early results of a crystal truncation rod study, Geochimica et Cosmochimica Acta 59 (1995) 4557–4561.
[221] M.L. Schlegel, K.L. Nagy, P. Fenter, N.C. Sturchio, Structures of quartz (10−10) and (10−11)–water interfaces determined by X-ray reflectivity and atomic force microscopy of natural growth surfaces, Geochimica et Cosmochimica Acta 66 (2002) 3037–3054.
[222] S.H. Park, G. Sposito, Structure of water adsorbed on a mica surface, Physical Review Letters 89 (2002) 085501.
[223] Z. Zhang, P. Fenter, L. Cheng, N.C. Sturchio, M.J. Bedzyk, M. Predota, A. Bandura, J.D. Kubicki, S.N. Lvov, P.T. Cummings, A.A. Chialvo, M.K. Ridley, P. Benezeth, L. Anovitz, D.A. Palmer, M.L. Machesky, D.J. Wesolowski, Ion adsorption at the rutile–water interface: linking molecular and macroscopic properties, Langmuir 20 (2004) 4954–4969.
[224] Z. Zhang, Ph.D. thesis, Northwestern University, 2004.
[225] J.W. Halley, Y. Lin, M. Zhuang, Self consistent direct dynamics studies of interfaces, Faraday Discussions 121 (2002) 85–95.
[226] M. Predota, A.V. Bandura, P.T. Cummings, J.D. Kubicki, D.J. Wesolowski, A.A. Chialvo, M. Machesky, Electric double layer at the rutile (110) surface. 1. Structure of surfaces and interfacial water from molecular dynamics by use of ab initio potentials, Journal of Physical Chemistry B 108 (2004) 12049–12060.
[227] M. Predota, Z. Zhang, P. Fenter, D.J. Wesolowski, P.T. Cummings, Electric double layer at the rutile (110) surface. 2. Adsorption of ions from molecular dynamics and X-ray experiments, Journal of Physical Chemistry B 108 (2004) 12061–12072.
[228] A.V. Bandura, D.G. Sykes, V. Shapovalov, T.N. Troung, J.D. Kubicki, R.A. Evarestov, Adsorption of water on the TiO_2 (rutile) (110) surface: a comparison of periodic and embedded cluster calculations, Journal of Physical Chemistry B 108 (2004) 7844–7853.
[229] R. Schaub, R. Thostrup, N. Lopez, E. Laegsgaard, I. Stensgaard, J.K. Norskov, F. Besenbacher, Oxygen vacancies as active sites for water dissociation on rutile TiO2(110), Physical Review Letters 87 (2001) 266104.
[230] A. Fahmi, C. Minot, A theoretical investigation of water-adsorption on titanium-dioxide surfaces, Surface Science 304 (1994) 343–359.
[231] A.V. Bandura, J.D. Kubicki, Derivation of force field parameters for TiO_2–H_2O systems from a initio calculations, Journal of Physical Chemistry B 107 (2003) 11072–11081.
[232] S.H. Lee, J.C. Rasaiah, Molecular dynamics simulation of ion mobility. 2. Alkali metal and halide ions using the SPC/E model for water at 25 degrees C, Journal of Physical Chemistry 100 (1996) 1420–1425.
[233] B.J. Palmer, D.M. Pfund, J.L. Fulton, Direct modeling of EXAFS spectra from molecular dynamics simulations, Journal of Physical Chemistry 100 (1996) 13393–13398.
[234] T.E. Lister, Y. Chu, W. Cullen, H. You, R.M. Yonco, J.F. Mitchell, Z. Nagy, Electrochemical and X-ray scattering study of well defined RuO_2 single crystal surfaces, Journal of Electroanalytical Chemistry 524 (2002) 201–218.
[235] T.E. Lister, Y.V. Tolmachev, Y. Chu, W.G. Cullen, H. You, R. Yonco, Z. Nagy, Cathodic activation of RuO_2 single crystal surfaces for hydrogen evolution reaction, Journal of Electroanalytical Chemistry 554 (2003) 71–76.
[236] J. Paquette, R.J. Reeder, Relationship between surface-structure, growth-mechanism, and trace-element incorporation in calcite, Geochimica et Cosmochimica Acta 59 (1995) 735–749.
[237] R.J. Reeder, M. Nugent, C.D. Tait, D.E. Morris, S.M. Heald, K.M. Beck, W.P. Hess, A. Lanzirotti, Coprecipitation of uranium(VI) with calcite: XAFS, micro-XAS, and luminescence characterization, Geochimica et Cosmochimica Acta 65 (2001) 3491–3503.

[238] N.C. Sturchio, R.P. Chiarello, L.W. Cheng, P.F. Lyman, M.J. Bedzyk, Y.L. Qian, H.D. You, D. Yee, P. Geissbuhler, L.B. Sorensen, Y. Liang, D.R. Baer, Lead adsorption at the calcite–water interface: synchrotron X-ray standing wave and X-ray reflectivity studies, Geochimica et Cosmochimica Acta 61 (1997) 251–263.
[239] L. Cheng, P.F. Lyman, N.C. Sturchio, M.J. Bedzyk, X-ray standing wave investigation of the surface structure of selenite anions adsorbed on calcite, Surface Science 382 (1997) L690–L695.
[240] L. Cheng, P. Fenter, N.C. Sturchio, Z. Zhong, M.J. Bedzyk, X-ray standing wave study of arsenite incorporation at the calcite surface, Geochimica et Cosmochimica Acta 63 (1999) 3153–3157.
[241] P. Van Cappellen, L. Charlet, W. Stumm, P. Wersin, A surface complexation model of the carbonate mineral–aqueous solution interface, Geochimica et Cosmochimica Acta 57 (1993) 3505–3518.
[242] O.S. Pokrovsky, J.A. Mielczarski, O. Barres, J. Schott, Surface speciation models of calcite and dolomite/aqueous solution interfaces and their spectroscopic evaluation, Langmuir 16 (2000) 2677–2688.
[243] N.H. deLeeuw, S.C. Parker, Atomistic simulation of the effect of molecular adsorption of water on the surface structure and energies of calcite surfaces, Journal of the Chemical Society—Faraday Transactions 93 (1997) 467–475.
[244] K. Wright, R.T. Cygan, B. Slater, Structure of the $(10-14)$ surfaces of calcite, dolomite and magnesite under wet and dry conditions, Physical Chemistry Chemical Physics 3 (2001) 839–844.
[245] A.L. Rohl, K. Wright, J.D. Gale, Evidence from surface phonons for the (2×1) reconstruction of the $(10-14)$ surface of calcite from computer simulation, American Mineralogist 88 (2003) 921–925.
[246] S. Kerisit, S.C. Parker, Free energy of adsorption of water and calcium on the $\{10-14\}$ calcite surface, Chemical Communications (2004) 52–53.
[247] S. Kerisit, S.C. Parker, J.H. Harding, Atomistic simulation of the dissociative adsorption of water on calcite surfaces, Journal of Physical Chemistry B 107 (2003) 7676–7682.
[248] S. Hwang, M. Blanco, W.A. Goddard, Atomistic simulations of corrosion inhibitors adsorbed on calcite surfaces I. Force field parameters for calcite, Journal of Physical Chemistry B 105 (2001) 10746–10752.
[249] P.E. Hillner, A.J. Gratz, S. Manne, P.K. Hansma, Atomic-scale imaging of calcite growth and dissolution in real-time, Geology 20 (1992) 359–362.
[250] A.L. Rachlin, G.S. Henderson, M.C. Goh, An atomic force microscope (AFM) study of the calcite cleavage plane—image averaging in Fourier space, American Mineralogist 77 (1992) 904–910.
[251] F. Ohnesorge, G. Binnig, True atomic-resolution by atomic force microscopy through repulsive and attractive forces, Science 260 (1993) 1451–1456.
[252] A.J. Gratz, P.E. Hillner, P.K. Hansma, Step dynamics and spiral growth on calcite, Geochimica et Cosmochimica Acta 57 (1993) 491–495.
[253] Y. Liang, D.R. Baer, Anisotropic dissolution at the $CaCO_3(10-14)$–water interface, Surface Science 373 (1997) 275–287.
[254] R.P. Chiarello, R.A. Wogelius, N.C. Sturchio, In-situ synchrotron X-ray reflectivity measurements at the calcite–water interface, Geochimica et Cosmochimica Acta 57 (1993) 4103–4110.
[255] P. Fenter, P. Geissbuhler, E. DiMasi, G. Srajer, L.B. Sorensen, N.C. Sturchio, Surface speciation of calcite observed in situ by high-resolution X-ray reflectivity, Geochimica et Cosmochimica Acta 64 (2000) 1221–1228.
[256] P. Geissbühler, P. Fenter, E. DiMasi, G. Srajer, L.B. Sorensen, N.C. Sturchio, Three-dimensional structure of the calcite–water interface, Surface Science 573 (2004) 191–203.
[257] S.L. Stipp, M.F. Hochella, Structure and bonding environments at the calcite surface as observed with X-ray photoelectron-spectroscopy (XPS) and low-energy electron-diffraction (LEED), Geochimica et Cosmochimica Acta 55 (1991) 1723–1736.
[258] S.I. Kuriyavar, R. Vetrivel, S.G. Hegde, A.V. Ramaswamy, D. Chakrabarty, S. Mahapatra, Insights into the formation of hydroxyl ions in calcium carbonate: temperature dependent FTIR and molecular modelling studies, Journal of Materials Chemistry 10 (2000) 1835–1840.
[259] W. Neagle, C.H. Rochester, Infrared study of the adsorption of water and ammonia on calcium-carbonate, Journal of the Chemical Society—Faraday Transactions 86 (1990) 181–183.

[260] A. Paytan, M. Kastner, D. Campbell, M.H. Thiemens, Seawater sulfur isotope fluctuations in the cretaceous, Science 304 (2004) 1663–1665.
[261] J.J. De Yoreo, T.A. Land, B. Dair, Growth-morphology of vicinal hillocks on the (101) face of KH_2PO_4—from step-flow to layer-by-layer growth, Physical Review Letters 73 (1994) 838–841.
[262] P. Hartman, W.G. Pardok, On the relations between structure and morphology of crystals, Acta Crystallographica 8 (1955) 49–52.
[263] K.J. Davis, P.M. Dove, J.J. De Yoreo, The role of Mg^{2+} as an impurity in calcite growth, Science 290 (2000) 1134–1137.
[264] S.A. de Vries, P. Goedtkindt, W.J. Huisman, M.J. Zwanenburg, R. Feidenhans'l, S.L. Bennett, D.M. Smilgies, A. Stierle, J.J. De Yoreo, W.J.P. van Enckevort, P. Bennema, E. Vlieg, X-ray diffraction studies of potassium dihydrogen phosphate (KDP) crystal surfaces, Journal of Crystal Growth 205 (1999) 202–214.
[265] J. Arsic, M.F. Reedijk, A.J.R. Sweegers, Y.S. Wang, E. Vlieg, Compression versus expansion on ionic crystal surfaces, Physical Review B 64 (2001) 233402.
[266] W.E. Brown, J.P. Smith, J.R. Lehr, A.W. Frazier, Octacalcium phosphate and hydroxyapatite, Nature 196 (1962) 1048–1055.
[267] W.E. Brown, M. Mathew, M.S. Tung, Crystal chemistry of octacalcium phosphate, Progress in Crystal Growth and Characterization of Materials 4 (1981) 59–87.
[268] D.N. Misra, Adsorption on and Surface Chemistry of Hydroxyapatite, Plenum Press, New York, 1984.
[269] Y. Liu, G.H. Nancollas, Crystallization and colloidal stability of calcium phosphate phases, Journal of Physical Chemistry B 101 (1997) 3464–3468.
[270] G.L. Gaines, The ion-exchange properties of muscovite mica, Journal of Physical Chemistry 61 (1957) 1408–1413.
[271] R.M. Pashley, DLVO and hydration forces between mica surfaces in Li^+, Na^+, K^+, and Cs^+ electrolyte solutions: a correlation of double-layer and hydration forces with surface cation exchange properties, Journal of Colloid and Interface Science 83 (1981) 531–546.
[272] P.B. Miranda, L. Xu, Y.R. Shen, M. Salmeron, Icelike water monolayer adsorbed on mica at room temperature, Physical Review Letters 81 (1998) 5876–5879.
[273] P. Guenard, G. Renaud, A. Barbieer, M. Gautier-Soyer, Determination of the α-Al_2O_3 (0001) surface relaxation and termination by measurements of crystal truncation rods, Surface Review and Letters 5 (1998) 321–324.
[274] J. Toofan, P.R. Watson, The termination of the α-Al_2O_3 (0001) surface: a LEED crystallographic determination, Surface Science 401 (1998) 162–172.
[275] J. Ahn, J.W. Rabalais, Composition and structure of the Al_2O_3 0001-(1×1) surface, Surface Science 388 (1997) 121–131.
[276] V.E. Puchin, J.D. Gale, A.L. Shluger, E.A. Kotomin, J. Gunster, M. Brause, V. Kempter, Atomic and electronic structure of the corundum (0001) surface: comparison with surface spectroscopies, Surface Science 370 (1997) 190–200.
[277] J. Guo, D.E. Ellis, D.J. Lam, Electronic structure and energetics of sapphire (0001) and (1−102) surfaces, Physical Review B 45 (1992) 13647–13656.
[278] T.J. Godin, J.P. LaFemina, Atomic and electronic structure of the corundum (α-alumina) (0001) surface, Physical Review B 49 (1994) 7691–7696.
[279] J.W. Elam, C.E. Nelson, M.A. Cameron, M.A. Tolbert, S.M. George, Adsorption of H_2O on a single crystal α-Al_2O_3 (0001) surface, J. Phys. Chem. B 102 (1998) 7008–7015.
[280] P. Liu, T. Kendelewicz, E.J. Nelson, G.E. Brown, Reaction of water with MgO(100) surfaces: Part III. X-ray standing wave studies, Surface Science 415 (1998) 156–169.
[281] K.C. Hass, W.F. Schneider, A. Curioni, W. Andreoni, First-principles molecular dynamics simulations of H_2O on α-Al_2O_3 (0001), Journal of Physical Chemistry B 104 (2000) 5527–5540.
[282] K.C. Hass, W.F. Schneider, A. Curioni, W. Andreoni, The chemistry of water on alumina surfaces reaction dynamics from first principles, Science 282 (1998) 265–268.
[283] N.H. de Leeuw, S.C. Parker, Effect of chemisorption and physisorption of water on the surface structure and stability of α-alumina, Journal of the American Ceramic Society 82 (1999) 3209–3216.

[284] V. Shapovalov, T.N. Truong, Ab Initio study of water adsorption on α-Al_2O_3 (0001) crystal surface, Journal of Physical Chemistry B 104 (2000) 9859–9863.
[285] R. Di Filice, J.E. Northrup, Theory of the clean and hydrogenated Al_2O_3 (0001)-(1×1) surfaces, Physical Review B 60 (1999) R16287–R16290.
[286] X.-G. Wang, A. Chaka, M. Scheffler, Effect of the environment on α-Al_2O_3 surface structures, Physical Review Letters 84 (2000) 3650–3653.
[287] T.P. Trainor, P.J. Eng, G.E. Brown, I.K. Robinson, M. De Santis, Crystal truncation rod diffraction study of the α-Al_2O_3 $(1\,-1\,0\,2)$ surface, Surface Science 496 (2002) 238–250.
[288] R.M. Cornell, U. Schwertmann, The Iron Oxides: Structure, Properties, Reactions, Occurrences and Uses, Wiley-VCH, Weinheim, 2003, p. 664.
[289] W. Weiss, W. Ranke, Surface chemistry and catalysis on well-defined epitaxial iron-oxide layers, Progress in Surface Science 70 (2002) 1–151.
[290] J.R. Bargar, T.P. Trainor, J.P. Fitts, S.A. Chambers, G.E. Brown, In situ grazing-incidence extended X-ray absorption fine structure study of Pb(II) chemisorption on hematite (0001) and $(1\,-1\,0\,2)$ surfaces, Langmuir 20 (2004) 1667–1673.
[291] J.R. Bargar, S.N. Towle, G.E. Brown, G.A. Parks, Outer-sphere Pb(II) adsorbed at specific surface sites on single crystal alpha-alumina, Geochimica et Cosmochimica Acta 60 (1996) 3541–3547.
[292] A.S. Templeton, T.P. Trainor, S.J. Traina, A.M. Spormann, G.E. Brown, Pb(II) distributions at biofilm–metal oxide interfaces, Proceedings of the National Academy of Sciences of the United States of America 98 (2001) 11897–11902.
[293] J.R. Bargar, S.N. Towle, G.E. Brown, G.A. Parks, XAFS and bond-valence determination of the structures and compositions of surface functional groups and Pb(II) and Co(II) sorption products on single-crystal α-Al_2O_3, Journal of Colloid and Interface Science 185 (1997) 473–492.
[294] S.A. Chambers, S.I. Yi, Fe termination for small alpha, α-Fe_2O_3 (0001) as grown by oxygen-plasma-assisted molecular beam epitaxy, Surface Science 439 (1999) L785–L791.
[295] S. Thevuthasan, Y.J. Kim, S.I. Yi, S.A. Chambers, J. Morais, R. Denecke, C.S. Fadley, P. Liu, T. Kendelewicz, G.E. Brown, Surface structure of MBE-grown α-Fe_2O_3 (0001) by intermediate-energy X-ray photoelectron diffraction, Surface Science 425 (1999) 276–286.
[296] E. Wasserman, J.R. Rustad, A.R. Felmy, B.P. Hay, J.W. Halley, Ewald methods for polarizable surfaces with application to hydroxylation and hydrogen bonding on the (012) and (001) surfaces of α-Fe_2O_3, Surface Science 385 (1997) 217–239.
[297] C.M. Eggleston, M.F. Hochella, The structure of hematite (001) surfaces by scanning tunneling microscopy—image interpretation, surface relaxation, and step structure, American Mineralogist 77 (1992) 911–922.
[298] N.G. Condon, P.W. Murray, F.M. Leibsle, G. Thornton, A.R. Lennie, D.J. Vaughan, Fe_3O_4(111) termination of α-Fe_2O_3 (0001), Surface Science 310 (1994) L609–L613.
[299] N.G. Condon, F.M. Leibsle, A.R. Lennie, P.W. Murray, T.M. Parker, D.J. Vaughan, G. Thornton, Scanning tunneling microscopy studies of alpha-Fe_2O_3 (0001), Surface Science 397 (1998) 278–287.
[300] X.G. Wang, W. Weiss, S.K. Shaikhutdinov, M. Ritter, M. Petersen, F. Wagner, R. Schlogl, M. Scheffler, The hematite (α-Fe_2O_3) (0001) surface: evidence for domains of distinct chemistry, Physical Review Letters 81 (1998) 1038–1041.
[301] S.K. Shaikhutdinov, W. Weiss, Oxygen pressure dependence of the α-Fe_2O_3(0001) surface structure, Surface Science 432 (1999) L627–L634.
[302] O. Warschkow, D.E. Ellis, J.H. Hwang, N. Mansourian-Hadavi, T.O. Mason, Defects and charge transport near the hematite (0001) surface: an atomistic study of oxygen vacancies, Journal of the American Ceramic Society 85 (2002) 213–220.
[303] X.-G. Wang, W. Weiss, S.K. Shaikhutdinov, M. Ritter, M. Petersen, F. Wagner, R. Schlogl, M. Scheffler, The hematite (α-Fe_2O_3) (0001) surface: evidence for domains of distinct chemistry, Physical Review Letters 81 (1998) 1038–1041.
[304] T.P. Trainor, A.M. Chaka, P.J. Eng, M. Newville, G.A. Waychunas, J.G. Catalano, G.E. Brown, Structure and reactivity of the hydrated hematite (0001) surface, Surface Science 573 (2004) 204–224.

[305] C.M. Eggleston, A.G. Stack, K.M. Rosso, S.R. Higgins, A.M. Bice, S.W. Boese, R.D. Pribyl, J.J. Nichols, The structure of hematite (α-Fe_2O_3) (0 0 1) surfaces in aqueous media: scanning tunneling microscopy and resonant tunneling calculations of coexisting O and Fe terminations, Geochimica et Cosmochimica Acta 67 (2003) 985–1000.
[306] K. Reuter, M. Scheffler, First-principles atomistic thermodynamics for oxidation catalysis: surface phase diagrams and catalytically interesting regions, Physical Review Letters 90 (2003) 046103.
[307] M.F. Reedijk, J. Arsic, F.F.A. Hollander, S.A. de Vries, E. Vlieg, Liquid order at the interface of KDP crystals with water: evidence for icelike layers, Physical Review Letters 90 (2003) 066103.
[308] M.F. Reedijk, Ph.D. thesis, Katholieke Universiteit Nijmegen, 2003.
[309] E. Vlieg, personal communication, 2004.
[310] M.D. Francis, N.C. Webb, Calcified Tissue Research 6 (1971) 335.
[311] M.J. Glimcher, L.C. Bonar, M.D. Grynpas, W.J. Landis, A.M. Roufosse, Recent studies of bone mineral: Is the amorphous calcium phosphate theory valid?, Journal of Crystal Growth 53 (1981) 100–119.
[312] J. Arsic, D. Kaminski, P. Poodt, E. Vlieg, Liquid ordering at the brushite-{0 1 0}–water interface, Physical Review B 69 (2004) 245406.
[313] D. Hanein, B. Geiger, L. Addadi, Fibronectin adsorption to surfaces of hydrated crystals—an analysis of the importance of bound water in protein substrate interactions, Langmuir 9 (1993) 1058–1065.
[314] J. Heidberg, W. Haser, Journal of Electron Spectroscopy and Related Phenomena 54/55 (1990) 971.
[315] S. Folsch, A. Stock, M. Henzer, Two-dimensional water condensation on the NaCl(1 0 0) surface, Surface Science 264 (1992) 65–72.
[316] K. Ichikawa, M. Yamada, Atomic resolution for non-equilibrium structures in the steady state and for structural transformations at the interface between NaCl and water, Journal of Physics: Condensed Matter 8 (1996) 4889–4901.
[317] Q. Dai, M. Salmeron, Adsorption of water on NaCl (1 0 0) surfaces: role of atomic steps, Journal of Physical Chemistry B 1997 (1997) 1994–1998.
[318] A. Allouche, Water adsorption on NaCl (1 0 0): a quantum ab-initio cluster calculation, Surface Science 406 (1998) 279–293.
[319] H. Meyer, P. Entel, J. Hanfner, Physisorption of water on salt surfaces, Surface Science 488 (2001) 177–192.
[320] D.P. Taylor, W.P. Hess, M.I. McCarthy, Structure and energetics of the water/NaCl (1 0 0) interface, Journal of Physical Chemistry B 101 (1997) 7455–7463.
[321] H. Uchida, H. Takiyama, M. Matsuoka, Molecular dynamics simulation of the solution structure near the solid–liquid interface between the NaCl (1 0 0) and NaCl–KCl–H_2O Solutions, Crystal Growth & Design 3 (2003) 209–213.
[322] J. Arsic, D.M. Kaminski, N. Radenovic, P. Poodt, W.S. Graswinckel, H.M. Cuppen, E. Vlieg, Thickness-dependent ordering of water layers at the NaCl(1 0 0) surface, Journal of Chemical Physics 120 (2004) 9720–9724.
[323] L.W. Bruch, A. Glebov, J.P. Toennies, H. Weiss, A helium atom scattering study of water adsorption on the NaCl(1 0 0) single crystal surface, Journal of Chemical Physics 103 (1995) 5109–5120.
[324] Y. Kashibara, S. Kimura, J. Harada, X-ray measurements of the crystal truncation rod scattering from cleavage surfaces of ionic crystals, Surface Science 214 (1989) 477–492.
[325] H.A. Miers, Note on the crystallization of potassium bichromate, Mineralogical Magazine 15 (1908) 39–41.
[326] K. Sangwal, M. Szurgot, Growth morphology of potassium crystals from aqueous solutions, Journal of Crystal Growth 80 (1987) 351–365.
[327] W.J.P. van Enckevort, Growth steps on crystal surfaces: their observation and their interpretation, Current Topics in Crystal Growth 2 (1995) 535–551.
[328] M. Plomp, W.J.P. van Enckevort, E. Vlieg, Controlling crystal surface termination by cleavage direction, Physical Review Letters 86 (2001) 5070–5072.

[329] J. Borc, K. Sangwal, A. Richter, R. Ries, E. Mielniczek-Broska, Surface morphology of the {0 0 1} cleavage faces of potassium bichromate single crystals, Surface Science 489 (2001) 174–184.
[330] M. Plomp, W.J.P. van Enckevort, E. Vlieg, Etching and surface termination of $K_2Cr_2O_7$ {0 0 1} faces observed using in situ atomic force microscopy, Journal of Crystal Growth 216 (2000) 413–427.
[331] M. Plomp, Ph.D. thesis, University of Nijmegen, 1999.
[332] P.B. Miranda, Y.R. Shen, Liquid interfaces: a study by sum-frequency vibrational spectroscopy, Journal of Physical Chemistry B 103 (1999) 3292–3307.
[333] E.A. Raymond, T.L. Tarbuck, G.L. Richmond, Isotopic dilution studies of the vapor/water interface as investigated by vibrational sum-frequency spectroscopy, Journal of Physical Chemistry B 106 (2002) 2817–2820.
[334] Z. Zhang, P. Fenter, L. Cheng, N.C. Sturchio, M.J. Bedzyk, M.L. Machesky, D.J. Wesolowski, Model-independent X-ray imaging of adsorbed cations at the crystal–water interface, Surface Science 554 (2004) L95–L100.
[335] K.L. Nagy, M.L. Schlegel, P. Fenter, L.W. Cheng, N.C. Sturchio, Cation sorption on the muscovite (0 0 1) surface using X-ray reflectivity, Abstracts of Papers of the American Chemical Society 223 (2002) U617.
[336] W.H. Casey, B.L. Phillips, M. Karlsson, S. Nordin, J.P. Nordin, D.J. Sullivan, S. Neugebauer-Crawford, Rates and mechanisms of oxygen exchanges between sites in the $AlO_4Al_{12}(OH)_{24}(H_2O)_{12}^{7+}$ (aq) complex and water: implications for mineral surface chemistry, Geochimica et Cosmochimica Acta 64 (2000) 2951–2964.
[337] B.L. Phillips, W.H. Casey, M. Karlsson, Bonding and reactivity at oxide mineral surfaces from model aqueous complexes, Nature 404 (2000) 379–382.
[338] X.Q. Hou, D.L. Bish, S.L. Wang, C.T. Johnston, R.J. Kirkpatrick, Hydration, expansion, structure, and dynamics of layered double hydroxides, American Mineralogist 88 (2003) 167–179.
[339] K.N. Tu, J.W. Mayer, L.C. Feldman, Electronic Thin Film Science: for Electrical Engineers and Materials Scientists, Macmillan, New York, 1992, p. xvii, 428 p.
[340] F.T. Gittes, M. Schick, Complete and incomplete wetting by adsorbed solids, Physical Review B 30 (1984) 209–214.
[341] P.G. de Gennes, Wetting: statics and dynamics, Reviews of Modern Physics 57 (1985) 827–863.
[342] B.M. Law, Wetting, adsorption and surface critical phenomena, Progress in Surface Science 66 (2001) 159–216.
[343] O. Shpyrko, M. Fukuto, P. Pershan, B. Ocko, I. Kuzmenko, T. Gog, M. Deutsch, Surface layering of liquids: the role of surface tension, Physical Review B 69 (2004) 245423.
[344] A. Braslau, P.S. Pershan, G. Swislow, B.M. Ocko, J. Als-Nielsen, Capillary waves on the surface of simple liquids measured by X-ray reflectivity, Physical Review A 38 (1988) 2457–2470.
[345] M.J. Regan, E.H. Kawamoto, S. Lee, P.S. Pershan, N. Maskil, M. Deutsch, O.M. Magnussen, B.M. Ocko, L.E. Berman, Surface layering in liquid Gallium—an X-ray reflectivity study, Physical Review Letters 75 (1995) 2498–2501.
[346] O.M. Magnussen, M.J. Regan, E.H. Kawamoto, B.M. Ocko, P.S. Pershan, N. Maskil, M. Deutsch, S. Lee, K. Penanen, L.E. Berman, X-ray reflectivity studies of the surface structure of liquid metals, Physica B 221 (1996) 257–260.
[347] H. Tostmann, E. DiMasi, O.G. Shpyrko, P.S. Pershan, B.M. Ocko, M. Deutsch, Surface phases in binary liquid metal alloys: an X-ray study, Berichte Der Bunsen-Gesellschaft—Physical Chemistry Chemical Physics 102 (1998) 1136–1141.
[348] O. Shpyrko, P. Huber, A. Grigoriev, P. Pershan, B. Ocko, H. Tostmann, M. Deutsch, X-ray study of the liquid potassium surface: structure and capillary wave excitations, Physical Review B 67 (2003) 115405.
[349] E. DiMasi, H. Tostmann, O.G. Shpyrko, M. Deutsch, P.S. Pershan, B.M. Ocko, Surface-induced order in liquid metals and binary alloys, Journal of Physics—Condensed Matter 12 (2000) A209–A214.